

This is a non peer-reviewed preprint uploaded to EarthArxiv. This manuscript has been submitted for publication in Earth and Space Science. Subsequent versions of this manuscript may have slightly different content.

Please feel free to contact Penny Wieser (penny.wieser (at) gmail.com) with any comments or suggestions to improve this paper.

## VESIcal Part II: A critical approach to volatile solubility modelling using an open-source Python3 engine

P. E. Wieser<sup>1,2\*</sup>, K. Iacovino<sup>3</sup>, S. Matthews<sup>4</sup>, G. Moore<sup>3</sup>, C. M. Allison<sup>5,6</sup>

<sup>1</sup>Department of Earth Sciences, University of Cambridge, UK.

<sup>2</sup>College of Earth, Ocean and Atmospheric sciences, Oregon State University

<sup>3</sup>Jacobs, NASA Johnson Space Center, Houston, TX 77058, USA.

<sup>4</sup>Johns Hopkins University, Department of Earth and Planetary Sciences, Baltimore, MD 21218, USA.

<sup>5</sup>Cornell University, Department of Earth and Atmospheric Sciences, Ithaca, NY 14853

<sup>6</sup>City College of New York, City University of New York, New York, NY 10031

# VESIcal Part II: A critical approach to volatile solubility modelling using an open-source Python3 engine

P. E. Wieser<sup>1,2\*</sup>, K. Iacovino<sup>3</sup>, S. Matthews<sup>4</sup>, G. Moore<sup>3</sup>, C. M. Allison<sup>5,6</sup>

<sup>1</sup>Department of Earth Sciences, University of Cambridge, UK.

<sup>2</sup>College of Earth, Ocean and Atmospheric sciences, Oregon State University

<sup>3</sup>Jacobs, NASA Johnson Space Center, Houston, TX 77058, USA.

<sup>4</sup>Johns Hopkins University, Department of Earth and Planetary Sciences, Baltimore, MD 21218, USA.

<sup>5</sup>Cornell University, Department of Earth and Atmospheric Sciences, Ithaca, NY 14853

<sup>6</sup>City College of New York, City University of New York, New York, NY 10031

## Key Points:

- The Python3 tool VESIcal allows extensive comparisons to be drawn between different H<sub>2</sub>O-CO<sub>2</sub> solubility models
- Solubility models are not interchangeable; for a single magma composition, different models can predict a wide range of solubility relationships
- The P-T-X calibration range of each solubility model must be critically evaluated before application to a specific volcanic system

---

Corresponding author: P. Wieser, [penny.wieser@gmail.com](mailto:penny.wieser@gmail.com)

17      **Abstract**

18      Accurate models of H<sub>2</sub>O and CO<sub>2</sub> solubility in silicate melts are vital for understanding volcanic  
19      plumbing systems. These models are used to estimate the depths of magma storage regions from melt  
20      inclusion volatile contents, investigate the role of volatile exsolution as a driver of volcanic eruptions,  
21      and track the degassing paths followed by magma ascending to the surface. However, despite the large  
22      increase in the number of experimental constraints over the last two decades, many recent studies still  
23      utilize the earlier generation of models, which were calibrated on experimental datasets with restricted  
24      compositional ranges. This may be because many of the available tools for more recent models re-  
25      quire large numbers of input parameters to be hand-typed (e.g., temperature, concentrations of H<sub>2</sub>O,  
26      CO<sub>2</sub>, and 8–14 oxides), making them difficult to implement on large datasets. Here, we use a new  
27      open-source Python3 tool, VESIcal, to critically evaluate the behaviours and sensitivities of different  
28      solubility models for a range of melt compositions. Using literature datasets of andesitic-dacitic ex-  
29      perimental products and melt inclusions as case studies, we illustrate the importance of evaluating the  
30      calibration dataset of each model. Finally, we highlight the limitations of particular data presentation  
31      methods such as isobar diagrams, and provide suggestions for alternatives, and best practices regard-  
32      ing the presentation and archiving of data. This review will aid the selection of the most applicable  
33      solubility model for different melt compositions, and identifies areas where additional experimental  
34      constraints are required. (242/250 words)

35      **Plain Language Summary**

36      Being able to accurately model the solubility of H<sub>2</sub>O and CO<sub>2</sub> in magmas is very important for  
37      understanding a wide variety of volcanic processes, such as the depths at which magma is stored in  
38      the crust, the driving force behind volcanic eruptions, and the release of volatile elements into the  
39      atmosphere. However, there has been no easy way for volcanologists to perform calculations on large  
40      datasets, or to compare different models. This review uses a new, open-source tool called VESIcal  
41      written in the popular programming language Python3. This allows us to compare different models for  
42      a wide variety of melt compositions, temperatures and pressures, helping researchers to identify the  
43      most suitable model for their study. We also suggest areas where further experimental constraints are  
44      required. Finally, we highlight the limitations of particular data presentation methods such as isobar  
45      diagrams, and provide suggestions for alternatives, and best practices regarding the presentation and  
46      archiving of data.

47      **1 Introduction**

48      The most abundant volatile components found in terrestrial magmatic systems are H<sub>2</sub>O and  
 49      CO<sub>2</sub>. It has been known for nearly a century (Bowen, 1928; Tuttle & Bowen, 1958) that these volatile  
 50      species have profound effects on the chemical and material properties of magmas (e.g., phase equilib-  
 51      ria, melting temperatures, magma viscosity and density; Burnham, 1979; Husen et al., 2016; Burnham  
 52      & Davis, 1974; Hess & Dingwell, 1996; Ochs & Lange, 1999), so significantly affect their geochemical  
 53      and dynamical behavior (e.g., eruption and degassing style, erupted volume; Papale et al., 1999; Hup-  
 54      pert & Woods, 2002). Thus, it is vital to be able to predict how H<sub>2</sub>O and CO<sub>2</sub> solubilities change as  
 55      a function of intensive variables such as pressure, temperature, melt and fluid composition in order to  
 56      understand plutonic and volcanic systems.

57      The solubility of a volatile species is defined at a given pressure and temperature as the maxi-  
 58      mum concentration that can be dissolved within a silicate melt of a specified composition. Ignoring  
 59      disequilibrium effects, if the volatile content of the system exceeds this solubility limit, a separate  
 60      fluid/vapour phase will exsolve from the magma. In this review, we favour the term fluid because of  
 61      the supercritical nature of exsolved volatile phases at magmatic temperatures. In general terms, a  
 62      magma is described as volatile undersaturated when there is no fluid phase, and volatile saturated  
 63      once a fluid phase is present (also referred to as vapour undersaturated/saturated, or fluid undersatu-  
 64      rated/saturated). In detail, different volatile species do not act as independent entities, but influence  
 65      one another. For this reason, a magma may exsolve a mixed CO<sub>2</sub>-H<sub>2</sub>O fluid even if the dissolved con-  
 66      centrations of H<sub>2</sub>O and CO<sub>2</sub> do not exceed the pure solubility limit of each species.

67      Despite the obvious importance of accurate volatile solubility modelling, very few studies of vol-  
 68      canic systems have evaluated results using several different solubility models to determine possible  
 69      sources of systematic and random error, and assess the suitability of each model for the conditions of  
 70      interest (e.g. temperature, pressure, and melt composition). This lack of intercomparison likely re-  
 71      sults from the fact that it is extremely time consuming to perform the large numbers of calculations  
 72      necessary for thorough comparisons using available tools. For example, many solubility models were  
 73      released as stand-alone Excel spreadsheets (e.g., G. Moore et al., 1998; Newman & Lowenstein, 2002;  
 74      Allison et al., 2019) or web apps (e.g., Iacono-Marziano et al., 2012; Ghiorso & Gualda, 2015), where  
 75      saturation pressures, dissolved volatile contents, degassing paths, and isobars can only be calculated  
 76      for one sample and set of conditions at a time. The more recent models which include several terms  
 77      accounting for the effect of melt composition on volatile solubility require users to hand-type a large  
 78      number of input parameters. For example, to calculate a saturation pressure in MagmaSat (Ghiorso  
 79      & Gualda, 2015), users must hand-type 9–14 oxide concentrations in addition to entering H<sub>2</sub>O and

80 CO<sub>2</sub> concentrations, and a melt temperature. Similarly, the web app of Iacono-Marziano et al. (2012)  
81 requires users to input 8 major element oxide concentrations. Calculating isobars using these web  
82 apps is a particularly daunting task, as users must evaluate dissolved volatile contents at multiple fluid  
83 compositions, and then use curve fitting to produce a smooth isobar to display on plots. Other mod-  
84 els were released with no calculator at all, requiring each user to correctly interpret and combine the  
85 relevant equations in the manuscript (Dixon, 1997; Shishkina et al., 2014).

86 Here, we take advantage of the recent release of VESIcal (Volatile Equilibria and Saturation  
87 Identification calculator; Iacovino et al., 2021), an open-source tool written in Python3. VESIcal con-  
88 tains functions to calculate saturation pressures, dissolved volatile contents, isobars, and degassing  
89 paths automatically for seven different models. Calculations can be performed based on melt com-  
90 positions provided in an Excel spreadsheet, and users can take full advantage of Python's extensive  
91 flexibility to perform large numbers of calculations automatically (e.g., creating for loops to perform  
92 calculations across a range of pressures, temperatures, and fluid compositions). To our knowledge,  
93 the only other model with similar functionality to VESIcal is the Linux program Solwcad supplied by  
94 Papale et al. (2006), which performs calculations automatically on a user-supplied .txt file containing  
95 melt compositions, pressures and temperatures (<http://www.pi.ingv.it/progetti/eurovolc/>). Sol-  
96 wcad was used alongside VESIcal in this review, through the Windows Subsystem for Linux (WSL2).

97 The overall aim of this review is to summarize the formulation, strengths and weaknesses of pop-  
98 ular solubility models to inform users who wish to model volatile solubility in silicate melts, whether  
99 that be the calculation of melt inclusion saturation pressures, degassing paths, incorporating volatile  
100 exsolution in physical model of magma chambers (e.g. Huber et al., 2019), or calculating the dissolved  
101 volatile contents of experimental products where the pressure, temperature and fluid composition are  
102 known (e.g. Waters & Lange, 2015). We start by briefly summarizing the major results from volatile  
103 solubility experiments over the last century (section 2), before describing nine of the most popular  
104 solubility models (section 3). We then compare the solubility of pure H<sub>2</sub>O, mixed H<sub>2</sub>O-CO<sub>2</sub>, and pure  
105 CO<sub>2</sub> predicted by different models for representative mafic and silicic compositions (section 4). We  
106 also explore the sensitivity of these models to parameters such as temperature and redox state, which  
107 are often poorly constrained in igneous systems (section 5). Finally, we evaluate the suitability of  
108 these models for intermediate melt compositions, where experimental constraints are sparse relative to  
109 basaltic and rhyolitic melts (section 6). We conclude by discussing best practices for presenting and  
110 archiving data related to volatile components in igneous systems (section 7). The aim of this review  
111 is to give readers an insight into the strengths and weaknesses of different models, as well as the large  
112 systematic errors associated with model choice. This will help users of VESIcal and other tools to

113 select an appropriate model for their specific application. All the Python code used to perform these  
114 comparisons is provided in the supporting material, which users can easily adapt to evaluate melt  
115 compositions for their specific application.

## 116 **2 Major findings from experimental studies investigating volatile solubility in 117 magmas**

118 One of the earliest volatile studies was that of Goranson (1931), who investigated the effect of  
119 pressure on the solubility of water in granitic melts. The classic treatise of Tuttle and Bowen (1958)  
120 investigated the impact of H<sub>2</sub>O on mineral phase equilibrium. This study led to a wider recognition  
121 of the importance of volatiles, and motivated the development of both the experimental and analytical  
122 approaches to determining volatile solubilities as a function of pressure, temperature, and melt  
123 composition. Hamilton et al. (1964) was one of the first to compare H<sub>2</sub>O solubilities for differing melt  
124 compositions (basalt and andesite), while also investigating the effect of dissolved H<sub>2</sub>O and oxidation  
125 state on the magmatic phase equilibria. These studies were followed by the fundamental experimental  
126 measurements of the Burnham group on the dissolution of H<sub>2</sub>O in albite melts (e.g., Burnham &  
127 Davis, 1971, 1974).

128 Further investigation of volatile solubility over the next four decades in natural samples and  
129 experimental products was aided significantly by analytical developments, allowing volatile contents  
130 in quenched glasses to be measured by techniques such as Fourier Transform infra-red spectroscopy  
131 (FTIR; e.g., Stolper, 1982; Fine & Stolper, 1986; Silver et al., 1990) and secondary ion mass spectrometry  
132 (SIMS; Hervig & Williams, 1988; Hauri, 2002). In particular, the high spatial resolution of FTIR  
133 and SIMS (a few tens of micrometers) meant that volatile concentrations could be measured within  
134 quenched pockets of melt trapped within crystals (termed melt inclusions). Unlike subaerially-erupted  
135 lavas which have degassed almost all their H<sub>2</sub>O and CO<sub>2</sub> following their ascent to shallow pressures,  
136 melt inclusions remain pressurized during ascent as they are trapped in relatively incompatible crys-  
137 tals, so retain high volatile contents.

138 Melt inclusion analyses have greatly advanced our understanding of the behavior of volatiles in  
139 volcanic systems (Lowenstern, 2003; Hauri et al., 2002; Roggensack, 2001; Wallace et al., 1995; Métrich  
140 & Wallace, 2008; Sides et al., 2014a). For example, melt inclusions provide insights into pre-eruptive  
141 volatile contents (e.g., Saal et al., 2002; Hervig et al., 1989), and links between melt volatile contents  
142 and eruption styles (Lucic et al., 2016). The strong pressure-dependence on volatile solubility means  
143 that H<sub>2</sub>O and CO<sub>2</sub> contents within melt inclusions trapped from a volatile-saturated magma can be  
144 used to determine the pressure at which the inclusion was trapped (termed the saturation pressure or  
145 entrapment pressure). In turn, the distribution of saturation pressures in a suite of melt inclusions can

146 reveal the locations of the main regions of magma storage in a volcanic system. This explosion of new  
147 information from melt inclusions greatly increased the demand for flexible and accurate solubilities  
148 models that could be applied to a broad range of pressures, temperatures, and melt/fluid compositions  
149 (G. Moore, 2008; Ghiorso & Gualda, 2015).

150 It has become increasingly apparent from solubility experiments that while the solubility of  
151  $\text{H}_2\text{O}$  is relatively insensitive to melt composition (e.g., G. Moore & Carmichael, 1998; Shishkina et  
152 al., 2010),  $\text{CO}_2$  solubility is highly sensitive to melt composition, particularly in mafic melts where  
153 the carbonate ion is the dominant species (Dixon, 1997; Brooker et al., 2001a; Shishkina et al., 2010;  
154 Iacono-Marziano et al., 2012; Shishkina et al., 2014; Allison et al., 2019). This has lead to a great di-  
155 versity in the way that various models treat the dependence of  $\text{CO}_2$  solubility on melt composition. In  
156 general, models have become more complex with time as the region of compositional space spanned  
157 by solubility experiments has increased to include more alkaline lavas. The individual role and rela-  
158 tive importance of each cation species in the melt is still associated with a large degree of uncertainty  
159 (Allison et al., 2019), accounting for the larger discrepancies between different model predictions for  
160  $\text{CO}_2$  vs.  $\text{H}_2\text{O}$ .

161 Experimental work has also highlighted the complexities of mixing between  $\text{H}_2\text{O}$  and  $\text{CO}_2$  in  
162 igneous systems. In the simplest case, the addition of one component in a melt-fluid system decreases  
163 the activity, and therefore the solubility of the other component in the melt (Lowenstern, 2001). This  
164 behavior is referred to as Henrian/ideal behavior. Henry's Law states that the amount of a volatile  
165 dissolved in a liquid is proportional to its partial pressure in the gas phase in equilibrium with that  
166 liquid. Neglecting the possible entropic effects of speciation, the addition of  $\text{H}_2\text{O}$  to the fluid/gas phase  
167 acts to lower the partial pressure of  $\text{CO}_2$ , and therefore lowers the solubility of  $\text{CO}_2$  in the liquid.  
168 Similarly, addition of  $\text{CO}_2$  to the fluid/gas phase causes the solubility of  $\text{H}_2\text{O}$  in the melt to decrease.

169 Experimental studies have shown that Henry's law is generally obeyed at low pressures (<1  
170 kbar) in basaltic (Dixon et al., 1995) and rhyolitic melts (Blank et al., 1993). However, at higher pres-  
171 sures, some experimental observations have shown that the mixing behavior of  $\text{CO}_2$  and  $\text{H}_2\text{O}$  becomes  
172 strongly non-Henrian (Papale, 1999). For example, Eggler (1973), Mysen et al. (1976) and Mysen  
173 (1976) show that the solubility of  $\text{CO}_2$  in albitic melts increases with the addition of  $\text{H}_2\text{O}$  at higher  
174 pressures. This has been attributed to the fact that the addition of small amounts of water as  $\text{OH}^-$   
175 species decreases melt polymerization, and therefore enhances the solubility of  $\text{CO}_2$  relative to an en-  
176 tirely anhydrous melt. After a certain amount of  $\text{H}_2\text{O}$  is added, solubility decreases once more because  
177 the addition of  $\text{H}_2\text{O}$  to the fluid phase causes the fugacity of  $\text{CO}_2$  to decrease (Mysen, 1976; Dingwell,

178 1986; King & Holloway, 2002). More recently, this behavior has been demonstrated for dacitic and  
 179 rhyolitic melts by Behrens et al. (2004) and Liu et al. (2005).

180 The non-ideal behavior of H<sub>2</sub>O and CO<sub>2</sub> in basaltic and andesitic melts at higher pressures is  
 181 less well constrained. King and Holloway (2002) show that at 1 kbar, andesitic melts (SiO<sub>2</sub>=58.4 wt%)  
 182 exhibit a sharp increase in the solubility of CO<sub>3</sub><sup>2-</sup> species with increasing melt H<sub>2</sub>O contents between  
 183 0–3.39 wt%. In contrast, Jakobsson (1997) show that the solubility of CO<sub>2</sub> in an icelanditic melt (54.6  
 184 wt% SiO<sub>2</sub>) at 10 kbar is essentially constant, despite variation in melt water contents between ~1–9  
 185 wt%. Similar behaviour to that observed by Jakobsson (1997) was noted for andesitic magmas (57.4  
 186 wt% SiO<sub>2</sub>) at 5 kbar by Botcharnikov et al. (2006), who suggest that differences between H<sub>2</sub>O-CO<sub>2</sub>  
 187 mixing in their experiments and those of King and Holloway (2002) may result from differences in  
 188 oxygen fugacity of these experiments (Fe<sup>3+</sup>/Fe<sub>T</sub>=0.2–0.6 vs. Fe<sup>3+</sup>/Fe<sub>T</sub>=0.09–0.2). However, as we  
 189 discuss in section 4.1, the influence of oxygen fugacity on volatile solubility is still poorly constrained.  
 190 Recent basaltic H<sub>2</sub>O-CO<sub>2</sub> experiments generally show a relatively flat plateau for CO<sub>2</sub> solubility with  
 191 increasing melt H<sub>2</sub>O contents between ~0–4 wt% (Iacono-Marziano et al., 2012; Shishkina et al., 2010,  
 192 2014), although relatively large error bars on analyses of CO<sub>2</sub> in experimental products make it diffi-  
 193 cult to determine whether this plateau is truly flat, or shows a slight positive or negative gradient at  
 194 low H<sub>2</sub>O contents (see Fig. 7a of Iacono-Marziano et al., 2012). The effect of H<sub>2</sub>O-CO<sub>2</sub> mixing in the  
 195 9 solubility models evaluated here is discussed further in sections 4.2.2 and 4.3.2.

### 196 3 Models discussed in this review

197 In this review, we focus on the seven models implemented in VESIcal (Iacovino et al., 2021):

- 198 1. The simplified parameterization of the Dixon (1997) model for H<sub>2</sub>O and CO<sub>2</sub>, which was im-  
 199 plemented in the popular Excel tool VolatileCalc (Newman & Lowenstern, 2002), hereafter  
 200 VolatileCalc-Basalt.
- 201 2. The H<sub>2</sub>O model of G. Moore et al. (1998), hereafter M–1998.
- 202 3. The H<sub>2</sub>O and CO<sub>2</sub> models of Liu et al. (2005), hereafter L–2005.
- 203 4. The H<sub>2</sub>O and CO<sub>2</sub> models of Iacono-Marziano et al. (2012), hereafter IM–2012.
- 204 5. The H<sub>2</sub>O and CO<sub>2</sub> models of Shishkina et al. (2014), hereafter S–2014.
- 205 6. The combined H<sub>2</sub>O and CO<sub>2</sub> model of Ghiorso and Gualda (2015), hereafter MagmaSat.
- 206 7. The CO<sub>2</sub> models of Allison et al. (2019), hereafter A–2019.

207 We also consider the two additional models, reflecting both their popularity and relative ease of calcu-  
 208 lation using previously published tools:

209        8. The combined H<sub>2</sub>O and CO<sub>2</sub> model of Papale et al. (2006), hereafter P–2006, accessed using the  
210        Linux program solwcad.

211        9. The Rhyolite functions in the VolatileCalc spreadsheet, hereafter VolatileCalc-Rhyolite

212        We do not consider the models of X. Duan (2014), Eguchi and Dasgupta (2018), or Burgisser et al.  
213        (2015) because no tool exists to automate the necessary calculations. We also do not discuss models  
214        with more limited pressure (P), temperature (T) or compositional (X) ranges.

215        A summary of the P, T and X range covered by the calibration dataset of each of the 9 models  
216        evaluated, as well as available tools to perform calculations, is provided in Figure 1. The calibration  
217        dataset of each model is shown on a total alkali-silica diagram in Figure 2. Detailed descriptions of  
218        each model are provided below.

Publication	Volatile	Speciation	P (bar)	T (°C)	Compositional range	Formulation	Redox sensitive?	Available Tools	Notes
Moore et al., 1998	H <sub>2</sub> O		0–3000 <sup>1</sup>	700–1200 <sup>1</sup>	Broad compositional range: subalkaline basalts to rhyolites; alkaline trachybasalts–andesites, foidites, phonolites	Thermodynamic basis, empirical effect of melt composition	No (input FeO <sub>T</sub> )	Macro-enabled Excel spreadsheet supplied by authors Python3 code <b>VEStCalc</b> ; Iacovino et al. 2021 <sup>1</sup>	'Author-suggested calibration range. The calibration dataset spans 190 to 6067 bar, and 800–1200 °C.
Newman and Lowenstein (2002), VolatileCalc–Basalt	H <sub>2</sub> O CO <sub>2</sub>	H <sub>2</sub> O as OH <sup>+</sup> and H <sub>2</sub> O <sub>tot</sub> , CO <sub>2</sub> as CO <sub>3</sub> <sup>2-</sup>	0–5000 <sup>1</sup> 0–2000 <sup>2</sup> 0–1000 <sup>3</sup>	600–1500 <sup>1</sup> 1200 <sup>4</sup>	Alkali basalts; 40–49 wt% SiO <sub>2</sub>	Thermodynamic basis, Empirical effect of melt composition	No (input SiO <sub>2</sub> only)*	Macro-enabled Excel spreadsheet ( <b>VolatileCalc</b> ; Newman and Lowenstein, 2002).	Warnings implemented in <b>VolatileCalc</b> (Newman and Lowenstein, 2002).
Newman and Lowenstein (2002), VolatileCalc–Rhyolite	H <sub>2</sub> O CO <sub>2</sub>	H <sub>2</sub> O as OH <sup>+</sup> and H <sub>2</sub> O <sub>tot</sub>	0–5000 <sup>1</sup>	600–1500 <sup>1</sup>	Rhyolites	Thermodynamic basis, no compositional term	No	Macro-enabled Excel spreadsheet ( <b>VolatileCalc</b> ; Newman and Lowenstein, 2002)	Calibration range suggested by Iacovino–Marziano et al. (2012).
Liu et al. 2005	H <sub>2</sub> O CO <sub>2</sub>		0–5000 <sup>1</sup>	700–1200 <sup>1</sup>	Haplogranites and rhyolites	Empirical basis, no compositional term	No	Macro-enabled Excel spreadsheet ( <b>VolatileCalc</b> ; Newman and Lowenstein, 2002)	*Calibration temperature of Dixon (1997).
Papale et al. (2006)	H <sub>2</sub> O CO <sub>2</sub>		0–10,000 <sup>1</sup>	~630–1630 <sup>1</sup>	Broad compositional range (SiO <sub>2</sub> =37–85 Na <sub>2</sub> O+K <sub>2</sub> O=0–20) for H <sub>2</sub> O, more limited for CO <sub>2</sub> and CO <sub>2</sub> –H <sub>2</sub> O liquids. Poor coverage of intermediate compositions (SiO <sub>2</sub> =55–75 wt%).	Fully thermodynamic (formulation + effect of melt composition)	Yes (input FeO and Fe <sub>x</sub> O <sub>3</sub> )	Python3 code ( <b>VEStCalc</b> ; Iacovino et al. 2021 <sup>1</sup> )	'Author-suggested calibration range for the mixed fluid model. The calibration dataset covers 70–550 bar and 800–1150 °C for the Carbon model, and 1–5000 bar and 700–1200 °C for the water model'
Iacono–Marziano et al., 2012	H <sub>2</sub> O CO <sub>2</sub>		100–10000 (mostly <5000) <sup>1</sup>	1100–1400 (preferably 1200–1300) <sup>2</sup>	Predominantly mafic compositions: subalkaline and alkaline basalts–andesites	Thermodynamic basis, Empirical effect of melt composition	No (input FeO <sub>T</sub> )	Web application ( <a href="http://calcul-iiso.cnrs-orleans.fr/appsh2o-co2/">http://calcul-iiso.cnrs-orleans.fr/appsh2o-co2/</a> – <b>VEStCalc</b> ; Iacovino et al. 2021 <sup>1</sup> )	'Inference' of H <sub>2</sub> O–CO <sub>2</sub> fields on Fig. 10 of Papale (1998)
Shishkina et al. 2014	H <sub>2</sub> O <sup>1</sup> CO <sub>2</sub> <sup>1</sup>		163–6067 <sup>1</sup>	1000–1250 <sup>1</sup>	Mafic and intermediate compositions: Subalkaline basalts–basic andesites, alkali basalts–phonolites; SiO <sub>2</sub> <65 wt%.	Fully empirical (formulation + effect of melt composition)	Only for CO <sub>2</sub> (as T <sup>*</sup> equation uses Fe <sup>2+</sup> ), Calibrated with Fe=Fe <sup>2+</sup>	Python3 code ( <b>VEStCalc</b> ; Iacovino et al. 2021 <sup>1</sup> )	'Range of calibration dataset, as authors do not state a range. We note that the vast majority of experiments were conducted at <5000 bar.'
Nagmasat (Ghiorsi and Gualda, 2015)	H <sub>2</sub> O <sup>1</sup> CO <sub>2</sub> <sup>1</sup>	H <sub>2</sub> O as OH <sup>+</sup> CO <sub>2</sub> as CaCO <sub>3</sub> and CO <sub>2</sub> <sub>2tot</sub>	0–5000 <sup>2</sup> 500–5000 <sup>2</sup>	1050–1400 (preferably 1150–1250) <sup>2</sup> 1200–1250 <sup>2</sup> <sup>3</sup>	Predominantly mafic compositions: subalkaline basalts, alkaline basalts, trachybasalts	Fully thermodynamic (formulation + effect of melt composition)	Yes (input FeO and Fe <sub>x</sub> O <sub>3</sub> )	Web application ( <a href="http://melts.mfe.iris.upmc.fr/corba/CGS-H2O-CO2.html">http://melts.mfe.iris.upmc.fr/corba/CGS-H2O-CO2.html</a> – <b>VEStCalc</b> ; Iacovino et al. 2021 <sup>1</sup> )	'Authors state that most experiments were conducted between 1200–1300 °C (whole range 1100–1400 °C). Note, this model contains no temperature term.'
Allison et al., 2019	CO <sub>2</sub> <sup>1</sup>		0–7000 <sup>2</sup>	1200 <sup>3</sup> (~1000–1400)	Alkali-rich mafic magmas from 6 volcanic fields (San Francisco Volcanic Field, Sunset Crater, Erebus, Vesuvius, Etna, Stromboli). Separate model coefficients for each composition.	Thermodynamic basis, separate parameters for each of 6 melt compositions.	No	Excel spreadsheet supplied by authors Python3 code ( <b>VEStCalc</b> ; Iacovino et al. 2021 <sup>1</sup> )	'Although this model is for pure CO <sub>2</sub> , it was calibrated on mixed CO <sub>2</sub> –H <sub>2</sub> O experiments.'

Figure 1. Summary of the calibration range of each model, as well as available tools to perform calculations.

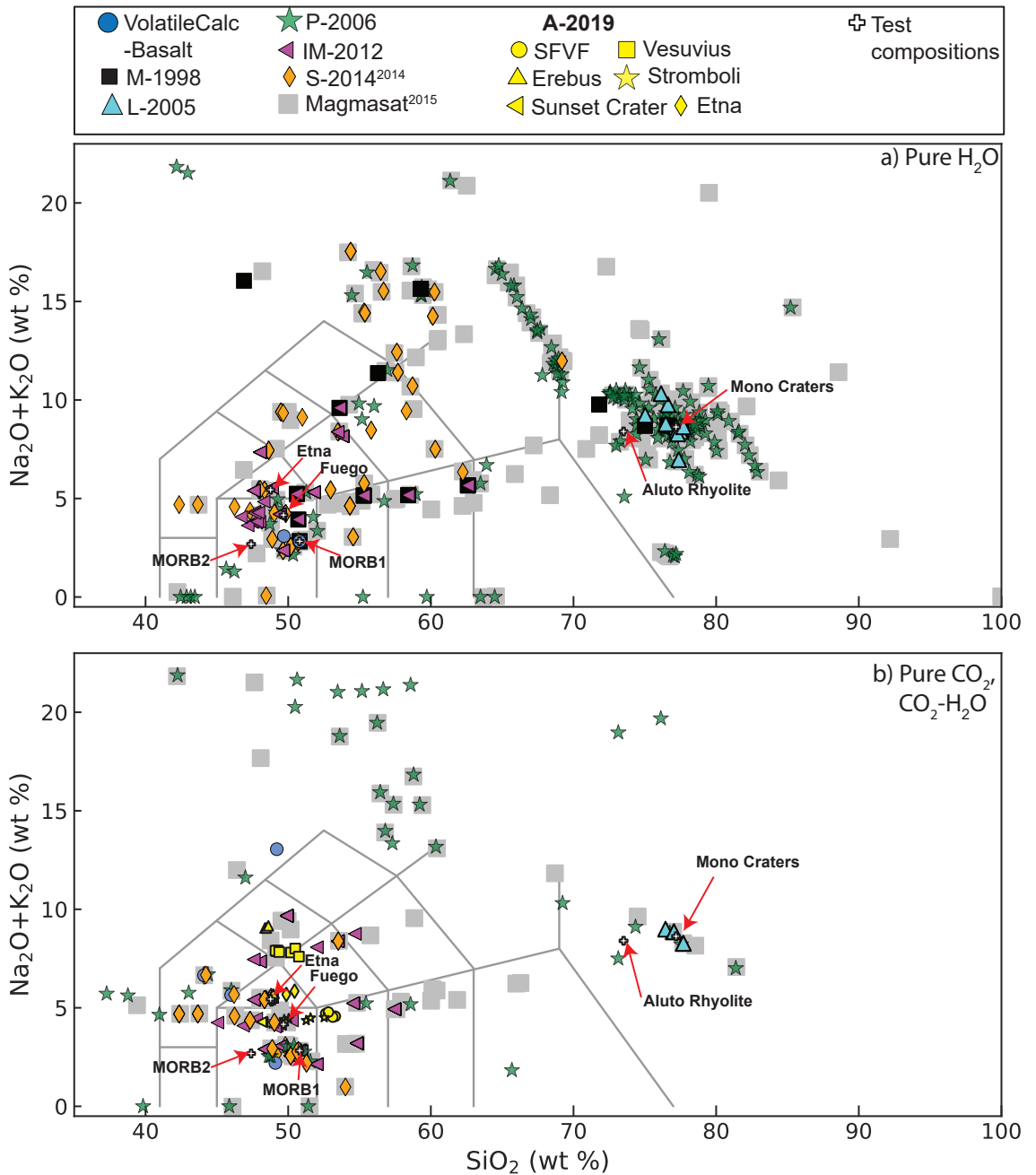


**Figure 2.** Total alkalis ( $\text{Na}_2\text{O} + \text{K}_2\text{O}$ ) vs.  $\text{SiO}_2$  (TAS) diagram showing the composition of melts in the calibration dataset of each model for a) pure  $\text{H}_2\text{O}$  and b) pure  $\text{CO}_2$  and mixed  $\text{CO}_2\text{-H}_2\text{O}$ . Pure  $\text{CO}_2$  and  $\text{CO}_2\text{-H}_2\text{O}$  experiments are combined because pure  $\text{CO}_2$  experiments are often contaminated by variable amounts of  $\text{H}_2\text{O}$  due to exposure with the earth's atmosphere, and the high mobility of  $\text{H}^+$  through experimental apparatus (Mangan et al., 2021). As dissolved  $\text{H}_2\text{O}$  contents in glasses from pure  $\text{CO}_2$  experiments are rarely reported, it is nontrivial to distinguish these from a mixed  $\text{H}_2\text{O-CO}_2$  experiment. For P-2006 and MagmaSat, points were extracted from the TAS diagrams shown in these papers using Web Plot Digitizer (Rohatgi, 2017). For the other models, the calibration dataset is provided in the supplementary information of Iacovino et al. (2021). TAS plot drawn using Python code from Stevenson (2015).

219        **3.1 VolatileCalc-Basalt: a simplification of Dixon (1997)**

220        The Dixon (1997) model calculates the solubility of H<sub>2</sub>O and CO<sub>2</sub> in basaltic silicate melts, com-  
 221        bining thermodynamic expressions as a function of pressure and temperature described in Dixon et  
 222        al. (1995) with empirical parameters from Dixon (1997) accounting for the effect of melt composition  
 223        in terms of melt SiO<sub>2</sub> content. The thermodynamic expressions are originally from Fine and Stolper  
 224        (1986) for carbon, and Silver and Stolper (1989) for water. The Dixon (1997) model considers the sol-  
 225        ubility of the carbonate ion (CO<sub>3</sub><sup>2-</sup>) for CO<sub>2</sub>, and both molecular water (H<sub>2</sub>O<sub>mol</sub>) and hydroxyl groups  
 226        (OH<sup>-</sup>) for H<sub>2</sub>O.

The solubility of molecular H<sub>2</sub>O is calculated using an adapted version of equation 3 of Dixon et al. (1995). In the original equation the X<sub>H<sub>2</sub>O<sub>mol</sub></sub><sup>m</sup>(P<sub>0</sub>, T<sub>0</sub>) term, representing the mole fraction of molecular H<sub>2</sub>O in equilibrium with fluid with a fugacity of water specified by f<sub>H<sub>2</sub>O</sub>(P<sub>0</sub>, T<sub>0</sub>) at 1473.15 K and 1 bar, was fixed at 3.28 × 10<sup>-5</sup>. To account for the effect of melt composition on H<sub>2</sub>O solubility, Dixon (1997) parametrize this term as a function of melt SiO<sub>2</sub> content:

$$X_{H_2O_{mol}}^m(P_0, T_0) = 3.04 \times 10^{-5} + 1.29 \times 10^{-6}[\text{SiO}_2]^{\text{wt}\%} \quad (1)$$

227        This relationship was derived from experimental observations of Cocheo and Holloway (1993),  
 228        and predicts that there is a ~30% increase in the solubility of H<sub>2</sub>O with increasing SiO<sub>2</sub> between  
 229        nephelinite (~40 wt% SiO<sub>2</sub>) and tholeiite (~49 wt% SiO<sub>2</sub>) melt compositions. The concentration of  
 230        OH<sup>-</sup> is then calculated as a function of the mole fraction of molecular H<sub>2</sub>O in the melt using the solu-  
 231        tion model of Silver and Stolper (1989) (see equation 4 of Dixon, 1997). Interestingly, this is the only  
 232        model discussed here which considers more than one species for dissolved H<sub>2</sub>O in the melt.

For CO<sub>2</sub> solubility, Dixon (1997) adapted the model of Dixon et al. (1995) to account for the effect of melt composition, based on observations from experiments that CO<sub>2</sub> solubility increases from tholeiitic (49 wt% SiO<sub>2</sub>) to basanitic (46 wt% SiO<sub>2</sub>) to leucitic (44.1 wt% SiO<sub>2</sub>) melts at 1200°C, 1 kbar. A linear regression with CO<sub>2</sub> solubility was achieved using a composition parameter (II) expressed in terms of the cation fractions, X<sub>i</sub> (Dixon, 1997):

$$\Pi = -6.50(X_{\text{Si}^{4+}} + X_{\text{Al}^{3+}}) + 20.17(X_{\text{Ca}^{2+}} + 0.8X_{\text{K}^+} + 0.7X_{\text{Na}^+} + 0.4X_{\text{Mg}^{2+}} + 0.4X_{\text{Fe}^{2+}}) \quad (2)$$

However, based on the strong correlation between II and SiO<sub>2</sub> in a suite of lavas from the North Arch Volcanic Field, Dixon (1997) simplify the X<sub>CO<sub>3</sub><sup>2-</sup></sub><sup>m</sup>(P<sub>0</sub>, T<sub>0</sub>) term from equation 6 of Dixon et al. (1995) solely as a function of melt SiO<sub>2</sub> content:

$$X_{\text{CO}_3^{2-}}^m(P_0, T_0) = 8.70 \times 10^{-6} - 1.70 \times 10^{-7}[\text{SiO}_2]^{\text{wt}\%} \quad (3)$$

233 Where  $X_{CO_3^{2-}}^m (P_0, T_0)$  is the mole fraction of carbonate in equilibrium with fluid with a fugacity of  
 234 carbon dioxide specified by  $f_{CO_2}(P_0, T_0)$  at 1473.15 K and 1 bar. Fugacities are calculated using the  
 235 Redlich-Kwong equation of state (Holloway, 1977), with the correction of Flowers (1979).

236 This simplified expression was designed to aid the investigations of volatile solubility in the suite  
 237 of lavas from the North Arch, where it effectively captures the observed 5× decrease in CO<sub>2</sub> solubility  
 238 from 40 to 49 wt% SiO<sub>2</sub>. However, this simplified parameterization became very widely used in a wide  
 239 variety of tectonic settings following its implementation in the Excel-based tool VolatileCalc (Newman  
 240 and Lowenstern, 2002). Here, we refer to this model as VolatileCalc-Basalt, to differentiate it from the  
 241 full II parameterization of Dixon (1997).

242 The advantage of the II-SiO<sub>2</sub> simplification is that users only have to input the concentration of  
 243 one oxide component (melt SiO<sub>2</sub>) in addition to melt temperature and melt volatile contents to cal-  
 244 culate saturation pressures or degassing paths. The limited number of inputs required by this model  
 245 meant that users can calculate saturation pressures for large numbers of melt inclusions relatively  
 246 quickly compared to more recent models such as Iacono-Marziano et al. (2012) and MagmaSat (which  
 247 require users to input 8–14 oxide concentrations).

248 However, extreme care must be taken when using this simplified model to calculate CO<sub>2</sub> solubil-  
 249 ity. Firstly, the North Arch lavas span SiO<sub>2</sub> contents of only 40–49 wt%. Because of the rapid drop in  
 250 II with increasing SiO<sub>2</sub>, extrapolation beyond 51.2 wt% SiO<sub>2</sub> yields a negative value for  $X_{CO_3^{2-}}^m (P_0,$   
 251  $T_0)$ , corresponding to a negative amount of dissolved CO<sub>2</sub>. To avoid this issue, VolatileCalc-Basalt  
 252 returns an error, and will not perform the calculation if users enter a SiO<sub>2</sub> content >49 wt%. Most  
 253 studies extrapolate beyond this by simply entering SiO<sub>2</sub>=49 wt% into VolatileCalc-Basalt if their  
 254 melts have higher silica contents (e.g. Sides et al., 2014a, 2014b; Tucker et al., 2019), and this ap-  
 255 proach is implemented in VESIcal for consistency. Newman and Lowenstern (2002) suggest that this  
 256 extrapolation will be “generally applicable for other basaltic rocks with <52 wt% SiO<sub>2</sub>”. However,  
 257 if a large proportion of a sample suite has SiO<sub>2</sub> contents with >49 wt% SiO<sub>2</sub>, the simplified II-SiO<sub>2</sub>  
 258 parameterization treats all melts as if they have the same composition, neglecting variations in sol-  
 259 ubility that may exist within that suite (see Wieser et al., 2021). Additionally, even if samples have  
 260 SiO<sub>2</sub> contents between 40–49 wt%, this simplification can yield spurious results for melts which do not  
 261 follow the same trend in II-SiO<sub>2</sub> space to the North Arch lavas (see section 4.2.3). Thus, we suggest  
 262 that any users wishing to apply VolatileCalc-Basalt to their system first check whether their melt com-  
 263 positions lie close to the trend defined by the North Arch lavas using the Jupyter notebook provided in  
 264 the supplementary information of Iacovino et al. (2021).

It is also worth noting that, because VolatileCalc-Basalt parameterizes the effect of melt composition in terms of the absolute concentration of SiO<sub>2</sub> (rather than other empirical models which use cation fractions), it is extremely sensitive to normalization. For example, consider the MORB2 composition in Table 1 which has a measured SiO<sub>2</sub> content of 47.4 wt%, and an anhydrous total of 97.375 wt%. For 1000 ppm CO<sub>2</sub> and T=1200°C, using raw data (SiO<sub>2</sub>=47.4 wt%) the calculated saturation pressure is 1206 bars. However, it is relatively common in the literature that major elements (excluding volatiles) are scaled to sum to 100%, while volatile concentrations are left unchanged. This would cause the melt SiO<sub>2</sub> content to increase to 48.68 wt% SiO<sub>2</sub>, corresponding to a saturation pressure of 1765 bar respectively (1.7× higher!). We encourage users not to normalize their data, as we note that the II-SiO<sub>2</sub> plot of North Arch Glasses in Dixon (1997) is best recreated using unnormalized data (see Supporting Fig. S1). Unnormalized data is used throughout this review for all VolatileCalc-Basalt outputs, which gives results comparable to those produced in the VolatileCalc-Basalt spreadsheet when users enter the SiO<sub>2</sub> contents given in Table 1.

### 3.2 VolatileCalc-Rhyolite: Newman and Lowenstern, 2002

In addition to the functionality for basalts described above, the VolatileCalc spreadsheet also allows users to calculate saturation pressures, degassing paths, isobars and isopleths for rhyolitic magmas (hereafter, VolatileCalc-Rhyolite). For CO<sub>2</sub>, VolatileCalc-Rhyolite uses the simple thermodynamic model from Stolper et al. (1987) that was later applied to rhyolitic melts by Fogel and Rutherford (1990). The molar enthalpy change for CO<sub>2</sub> dissolution in the melt is from Fogel and Rutherford (1990), the single-O melt mass from Silver et al. (1990), and the CO<sub>2</sub> molar volume and solubility at standard state from Blank et al. (1993). The thermodynamic basis for the H<sub>2</sub>O model is the same as that used in VolatileCalc-Basalt. The fitted parameters for H<sub>2</sub>O solubility in the standard state is from Silver (1988), and the single-O melt mass and molar enthalpy change for H<sub>2</sub>O dissolution in the melt from Silver et al. (1990). The partial molar volume of H<sub>2</sub>O was adjusted to 5 cm<sup>3</sup>/mol to provide a better fit to experimental data. There are two main differences of the rhyolite model relative to the basaltic model. First, while both the models use a temperature-dependent equation of state, VolatileCalc-Rhyolite model also contains a term for the heat of solution of volatile solubility, so is far more sensitive to temperature (see section 5). Second, unlike VolatileCalc-Basalt which require users to enter melt SiO<sub>2</sub> contents, VolatileCalc-Rhyolite is independent of melt composition. Thus, Newman and Lowenstern (2002) caution that this model may not be applicable for strongly peralkaline or peraluminous rhyolites.

296      **3.3 M–1998 (Moore et al., 1998)**

The Moore et al. (1998) model calculates the solubility of H<sub>2</sub>O for a wide range of silicate melt compositions using an empirical expression valid between 700–1200°C and 0–3000 bars:

$$2 \ln(X_{\text{H}_2\text{O}}^{\text{melt}}) = \frac{a}{T} + \sum_i b_i X_i \frac{P}{T} + c \ln(f_{\text{H}_2\text{O}}^{\text{fluid}}) + d \quad (4)$$

297      Where X<sub>H<sub>2</sub>O</sub><sup>melt</sup> is the mole fraction of H<sub>2</sub>O dissolved in the melt, T is the temperature in Kelvin, P is  
298      the pressure in bars, and X<sub>i</sub> is the anhydrous molar fraction of each oxide component. f<sub>H<sub>2</sub>O</sub><sup>fluid</sup> is the  
299      fugacity of H<sub>2</sub>O in the fluid, calculated using the modified version of the Redlich-Kwong equation  
300      of state provided in the appendix of Holloway and Blank (1994). Equation 4 is associated with the  
301      following fit parameters ( $\pm$  standard error):

Coefficient	a	b <sub>Al<sub>2</sub>O<sub>3</sub></sub>	b <sub>FeO<sub>T</sub></sub>	b <sub>Na<sub>2</sub>O</sub>	c	d
Value ( $\pm 1\sigma$ )	2565 ( $\pm 362$ )	-1.997 ( $\pm 0.706$ )	-0.9275 ( $\pm 0.394$ )	2.736 ( $\pm 0.871$ )	1.171 ( $\pm 0.069$ )	-14.21 ( $\pm 0.54$ )

302      As equation 4 includes a term for the fugacity of H<sub>2</sub>O in the fluid, this model can be integrated  
303      with CO<sub>2</sub> models implemented in VESIcal (e.g., the II-SiO<sub>2</sub> simplification of Dixon, 1997, Liu et al.,  
304      2005, Iacono-Marziano et al., 2012, Shishkina et al., 2014, Allison et al., 2019) to investigate mixed  
305      H<sub>2</sub>O-CO<sub>2</sub> fluids.

307      The model calibration dataset combines the authors' pure H<sub>2</sub>O experiments with literature data,  
308      spanning sub-alkaline basaltic to rhyolitic compositions, as well as some alkaline compositions (Fig. 2).  
309      As with other fully-empirical models implemented in VESIcal, or those including empirical expressions,  
310      extreme care must be taken when extrapolating this model outside of the calibration range. In partic-  
311      ular, the authors warn against extrapolating this model to pressures exceeding 3 kbar, in part due to  
312      the complexities of the critical behavior of fluids at higher pressures.

313      **3.4 L–2005 (Liu et al., 2005)**

The Liu et al. (2005) model calculates the solubility of H<sub>2</sub>O and CO<sub>2</sub> in metaluminous, high-silica rhyolitic melts using empirical expressions, valid between 700–1200°C, and 0–5000 bars. The following expression is used to calculate CO<sub>2</sub> solubility:

$$[CO_2]^{\text{ppm}} = \frac{P_{CO_2}(b_1 + b_4 P_W)}{T} + P_{CO_2}(b_2 P_W^{0.5} + b_3 P_W^{1.5}) \quad (5)$$

T is temperature in Kelvin, b<sub>1</sub>–b<sub>4</sub> are fit parameters, and the P<sub>W</sub> and P<sub>CO<sub>2</sub></sub> terms account for the partial pressures of each volatile species in the co-existing fluid, with:

$$P_{CO_2} = X_{CO_2}^f P \quad (6)$$

$$P_W = X_W^f P \quad (7)$$

314 Where P is pressure in MPa,  $X_{\text{CO}_2}^f$  is the mole fraction of CO<sub>2</sub> in the fluid, and  $X_{\text{H}_2\text{O}}^f$  is the mole fraction of H<sub>2</sub>O in the fluid. These empirical terms mean that no equation of state is used (unlike M-1998 and VolatileCalc-Basalt). The fit parameters associated with equation 5 are shown below ( $\pm$  error):

Coefficient	$b_1$	$b_2$	$b_3$	$b_4$
Value (Error)	5668 ( $\pm$ 127)	0.4133 ( $\pm$ 0.0491)	$2.041 \times 10^{-3}$ ( $\pm$ 0.285 $\times 10^{-3}$ )	-55.99 ( $\pm$ 8.36)

317

Similarly, they provide the following expression for H<sub>2</sub>O:

$$[\text{H}_2\text{O}_t]^{\text{wt}\%} = \frac{a_1 P_w^{0.5} + a_2 P_w + a_3 P_w^{1.5}}{T} + a_4 P_w^{1.5} + P_{\text{CO}_2} (a_5 P_w^{0.5} + a_6 P_w) \quad (8)$$

318 Using the following fit parameters:

Coefficient	$a_1$	$a_2$	$a_3$	$a_4$
Value (Error)	354.94 ( $\pm$ 4.55)	9.623 ( $\pm$ 0.923)	-1.5223 ( $\pm$ 0.0722)	0.0012439 ( $\pm$ 0.0000499)
				$a_5$
				$a_6$
				$-1.084 \times 10^{-4}$ ( $\pm$ 0.406 $\times 10^{-4}$ ) $-1.362 \times 10^{-5}$ ( $\pm$ 0.352 $\times 10^{-5}$ )

319

320 The model calibration dataset combines pure H<sub>2</sub>O solubility experiments by the authors be-  
 321 tween  $\sim$ 1 and 250 bars with literature experiments investigating the solubility of pure H<sub>2</sub>O, H<sub>2</sub>O-H<sub>2</sub>,  
 322 CO<sub>2</sub> and CO<sub>2</sub>-H<sub>2</sub>O fluids, spanning significantly higher pressures (up to 5000 bars). Unlike the M-  
 323 1998 model, their empirical expressions do not incorporate a term for melt composition, so care is  
 324 needed when applying this model to melts with different major element compositions to the calibration  
 325 dataset (Fig. 2).

### 326 3.5 P-2006 (Papale et al., 2006)

327 Papale et al. (2006) present a fully non-ideal thermodynamic model for H<sub>2</sub>O and CO<sub>2</sub> solubil-  
 328 ity, which is a recalibration of the earlier models of Papale (1999) and Papale (1997). This updated  
 329 model capitalizes on the large amount of volatile solubility experiments performed between 1997 and  
 330 2005, which nearly doubled the size of the calibration dataset, and allowed experimental data on CO<sub>2</sub>  
 331 solubility collected prior to 1980 to be discarded (removing systematic errors associated with different  
 332 analytical techniques, see Papale, 1999). Unlike the models discussed above which are calibrated on  
 333 a specific subregion of compositional space and use empirical parametrizations to account for the ef-  
 334 fect of melt composition, the models of Papale et al. (2006) and Papale (1999) treat the composition  
 335 of the silicate liquid using a thermodynamic approach based on Ghiorso et al. (1983). Papale et al.  
 336 (2006) note that this thermodynamic approach means that for any specific region of composition space  
 337 (e.g., comparing model results to a specific experiment), the fit may not be as good as an empirical  
 338 model tuned to that composition. However, carefully calibrated thermodynamic models will be signif-  
 339 icantly more successful than empirical models when applied to melts which are not represented in the  
 340 calibration dataset.

P–2006 considers a silicate liquid in mechanical, thermal and chemical equilibrium with a fluid phase containing H<sub>2</sub>O and CO<sub>2</sub>. The model uses the modified Redlich-Kwong equation of state of Kerrick and Jacobs (1981) to describe the fluid phase, and considers only the dissolution of CO<sub>2</sub> and H<sub>2</sub>O in the melt (while natural silicate melts contain molecular CO<sub>2</sub> and CO<sub>3</sub><sup>2-</sup> species, and molecular H<sub>2</sub>O and OH<sup>-</sup> species). The model calculates the Gibbs free energy of mixing, considering 10 major oxide components in addition to CO<sub>2</sub> and H<sub>2</sub>O. Binary interaction coefficients, denoted by  $w_{ij}$ , account for the attractive-repulsive behaviour between an oxide and volatile component. For example,  $w_{CO_2,MgO}$  describes the interaction of MgO with CO<sub>2</sub>. Interaction coefficients for CO<sub>2</sub> are expressed as a function of pressure (relative to a reference pressure of 0.1 MPa) requiring two coefficients, while those for H<sub>2</sub>O are invariant of pressure (requiring 1 coefficient):

$$w_{CO_2,i} = w_{CO_2,i}^0 + w_{CO_2,i}^1 \ln \frac{P}{P_0} \quad (9)$$

$$w_{H_2O,i} = w_{H_2O,i}^0 \quad (10)$$

P–2006 uses interaction terms for SiO<sub>2</sub>, Al<sub>2</sub>O<sub>3</sub>, MgO, CaO, Na<sub>2</sub>O, K<sub>2</sub>O, FeO and Fe<sub>2</sub>O<sub>3</sub>. The presence of two Fe terms means that the model is sensitive to melt redox. Papale et al. (2006) show that the inclusion of  $w$  terms for MnO and TiO<sub>2</sub> lead to overfitting, so the effect of these oxides on model outputs is only through the dilution of the concentration of components allocated  $w$  terms. The values of the 24  $w$  terms, as well as 5 terms accounting for molar volumes and fugacities, are calculated from a calibration dataset comprising  $\sim 1100$  solubility experiments with pure CO<sub>2</sub>, pure H<sub>2</sub>O and mixed CO<sub>2</sub>-H<sub>2</sub>O fluids. While the calibration dataset contains well populated clusters for basaltic and rhyolitic compositions, intermediate compositions and basaltic melts with high alkali contents are poorly represented, particularly for CO<sub>2</sub> (Fig. 2).

Papale et al. (2006) demonstrate that despite the addition of hundreds of new experimental datapoints for H<sub>2</sub>O, there are no significant changes in coefficients compared to those which were published with their 1999 model. The percent errors on the H<sub>2</sub>O coefficients in the 2006 model are < 10% for all species (defined as 100\*  $\sigma$ /coefficient). In contrast, the addition of new CO<sub>2</sub> data to the calibration dataset resulted in significant changes in coefficients, and the percentage errors on these coefficients in the 2006 model remained large ( $\sim 800\%$  for FeO,  $\sim 150\%$  for Na<sub>2</sub>O,  $\sim 190\%$  for MgO, Fig. 3). Based on these large error values, these coefficients would likely change again if this model was recalibrated to include all new CO<sub>2</sub> experiments published since 2006.

Finally, the pressure-dependence of the CO<sub>2</sub> melt interaction terms, combined with the fact that the  $w_0$  and  $w_1$  terms have different signs for all oxides except FeO, means that a given change in melt chemistry may cause an increase in CO<sub>2</sub> solubility at one pressure, but a decrease at another pressure (see Section 4.1). Ghiorso and Gualda (2015) note that the coefficient for the compressibility

of CO<sub>2</sub> in the P-2006 model is negative, which is physically impossible (implying the volume of the CO<sub>2</sub> fluid increases when pressure is increased), which they suggest may arise from the inclusion of pressure-dependent *w*-terms.

## P-2006

Element	CO <sub>2</sub>				H <sub>2</sub> O	
	w <sub>o</sub>	% error (1σ)	w <sub>1</sub>	% error	w <sub>o</sub>	% error
SiO <sub>2</sub>	-59,962	18	6049	19	-34,093	1.85
Al <sub>2</sub> O <sub>3</sub>	-590,957	32	41,395	47	-189,117	2.54
Fe <sub>2</sub> O <sub>3</sub>	4,469,623	9	-529,301	9	135,935	9.32
FeO	21,666	806	1214	1500	-195,751	3.13
MgO	52,866	189	-13,446	78	-86,418	7.06
CaO	-328,792	23	12,789	63	-209,997	1.67
Na <sub>2</sub> O	140,034	146	-35,213	60	-322,253	1.42
K <sub>2</sub> O	309,070	48	-58,010	27	-349,798	1.79

## MagmaSat

Element	CO <sub>2</sub> -CO <sub>3</sub> <sup>2-</sup>				H <sub>2</sub> O	
	W (CO <sub>2</sub> )	% error (1σ)	W (CaCO <sub>3</sub> )	% error	W	% error
SiO <sub>2</sub>			63.281	2.52	27.557	0.065
TiO <sub>2</sub>	-19.266	24.3	-79.203	0.46	88.199	2.87
Al <sub>2</sub> O <sub>3</sub>			46.716	2.52	11.768	21.8
Fe <sub>2</sub> O <sub>3</sub>	-3.187	4.9	65.509	0.26	50.105	17.0
Fe <sub>2</sub> SiO <sub>4</sub>	-32.465	44.5	-72.997	0.40	30.936	18.8
Mg <sub>2</sub> SiO <sub>4</sub>	-40.854	164.3	-24.873	4.17	20.910	21.5
CaSiO <sub>3</sub>	30.012	80.0	37.534	2.70	9.715	27.5
Na <sub>2</sub> SiO <sub>3</sub>			-311.011	0.24	-82.460	2.9
KAlSiO <sub>4</sub>			-27.865	8.21	1.057	112
Ca <sub>3</sub> (PO <sub>4</sub> ) <sub>2</sub>	-3.473	172.6	37.534	0.13	44.133	0.76

**Figure 3.** Interaction coefficients for P-2006 and MagmaSat. Percentage errors calculated as 100\*1σ/coefficient. Error are colored green if they are <10%, light pink if 10–25%, and red if >25%.

### 3.6 IM-2012 (Iacono-Marziano et al. 2012)

The Iacono-Marziano et al. (2012) model expresses the solubility of H<sub>2</sub>O and CO<sub>2</sub> in mafic melts by combining simplified thermodynamic expressions for melt-fluid thermodynamics with empirical formulations accounting for melt composition. For CO<sub>2</sub>, they present the following expression:

$$\ln[\text{CO}_2]^{\text{ppm}} = X_{\text{H}_2\text{O}} d_{\text{H}_2\text{O}} + X_{\text{AI}} d_{\text{AI}} + X_{\text{FeO}+\text{MgO}} d_{\text{FeO}+\text{MgO}} + X_{\text{Na}_2\text{O}+\text{K}_2\text{O}} d_{\text{Na}_2\text{O}+\text{K}_2\text{O}}$$

$$+ a_{\text{CO}_2} \ln[\text{PCO}_2] + b_{\text{CO}_2} \left[ \frac{\text{NBO}}{\text{O}} \right] + B_{\text{CO}_2} + C_{\text{CO}_2} \frac{\text{P}}{\text{T}} \quad (11)$$

Where P is the pressure in bars, T is the temperature in Kelvin,  $X_{\text{H}_2\text{O}}$  is the molar fraction of  $\text{H}_2\text{O}$  in the melt and  $P_{\text{CO}_2}$  is the partial pressure of  $\text{CO}_2$  in bars. The partial pressure of  $\text{CO}_2$  is calculated from the pressure multiplied by the mole fraction of  $\text{CO}_2$  in the fluid. This means that this model does not rely on an equation of state (as with the L–2005 model). The other terms account for the effect of melt composition using molar fractions calculated on a hydrous basis;  $X_{\text{FeO}+\text{MgO}}$  is the sum of molar fractions of  $\text{FeO}_t$  and  $\text{MgO}$ ,  $X_{\text{Na}_2\text{O}+\text{K}_2\text{O}}$  is the sum of the molar fractions of  $\text{Na}_2\text{O}$  and  $\text{K}_2\text{O}$ , and  $X_{\text{AI}}$  is the agpaitic index (AI):

$$X_{\text{AI}} = \frac{X_{\text{Al}_2\text{O}_3}}{X_{\text{CaO}} + X_{\text{K}_2\text{O}} + X_{\text{Na}_2\text{O}}} \quad (12)$$

The NBO/O term represents the number of non-bridging oxygens divided by oxygen, expressing the availability of oxygen to form carbonate groups within the melt. NBO/O can be calculated from mol fraction of different oxides,  $X_i$ , on an anhydrous or hydrous basis:

$$\frac{\text{NBO}}{\text{O}}^{\text{Anhyd}} = \frac{2(X_{\text{K}_2\text{O}} + X_{\text{Na}_2\text{O}} + X_{\text{CaO}} + X_{\text{MgO}} + X_{\text{FeO}} - X_{\text{Al}_2\text{O}_3})}{2X_{\text{SiO}_2} + 2X_{\text{TiO}_2} + 3X_{\text{Al}_2\text{O}_3} + X_{\text{MgO}} + X_{\text{FeO}} + X_{\text{CaO}} + X_{\text{Na}_2\text{O}} + X_{\text{K}_2\text{O}}} \quad (13)$$

$$\frac{\text{NBO}}{\text{O}}^{\text{Hyd}} = \frac{2(X_{\text{H}_2\text{O}} + X_{\text{K}_2\text{O}} + X_{\text{Na}_2\text{O}} + X_{\text{CaO}} + X_{\text{MgO}} + X_{\text{FeO}} - X_{\text{Al}_2\text{O}_3})}{2X_{\text{SiO}_2} + 2X_{\text{TiO}_2} + 3X_{\text{Al}_2\text{O}_3} + X_{\text{MgO}} + X_{\text{FeO}} + X_{\text{CaO}} + X_{\text{Na}_2\text{O}} + X_{\text{K}_2\text{O}} + X_{\text{H}_2\text{O}}} \quad (14)$$

In both cases, mole fractions are calculated on a hydrous basis (Iacono-Marziano, written comms).

Iacono-Marziano give coefficients for equation 11 for both cases ( $\pm 2\sigma$ ), leading to two forms of this model: IM–2012–A (anhydrous) and IM–2012–H (hydrous):

Coefficient	$d_{\text{H}_2\text{O}}$	$d_{\text{AI}}$	$d_{\text{FeO}+\text{MgO}}$	$d_{\text{Na}_2\text{O}+\text{K}_2\text{O}}$	$a_{\text{CO}_2}$	$b_{\text{CO}_2}$	$c_{\text{CO}_2}$	$e_{\text{CO}_2}$
Hydrous ( $\pm$ error)	-16.4 ( $\pm$ 1.2)	4.4 ( $\pm$ 0.4)	-17.1 ( $\pm$ 0.9)	22.8 ( $\pm$ 1.1)	1 ( $\pm$ 0.03)	17.3 ( $\pm$ 0.9)	0.12 ( $\pm$ 0.02)	-6 ( $\pm$ 0.4)
Anhydrous ( $\pm$ error)	2.3 ( $\pm$ 0.5)	3.8 ( $\pm$ 0.4)	-16.3 ( $\pm$ 0.9)	20.1 ( $\pm$ 1.1)	1 ( $\pm$ 0.03)	15.8 ( $\pm$ 0.9)	0.14 ( $\pm$ 0.02)	-5.3 ( $\pm$ 0.4)

371

We note for completeness that in the original publication, equation 11 was incorrectly expressed in terms of  $\ln[\text{CO}_3^{2-}]$  (Iacono-Marziano, written. comms).

For  $\text{H}_2\text{O}$ , the authors state that it is statistically unjustified to include  $d_i$  terms similar to those in the  $\text{CO}_2$  expression, due to the relatively small effect of melt composition on  $\text{H}_2\text{O}$  solubility. The effect of melt composition is incorporated only through the NBO/O term:

$$\ln [\text{H}_2\text{O}]^{\text{wt}\%} = a_{\text{H}_2\text{O}} \ln[P_{\text{H}_2\text{O}}] + b_{\text{H}_2\text{O}} \left[ \frac{\text{NBO}}{\text{O}} \right] + B_{\text{H}_2\text{O}} + C_{\text{H}_2\text{O}} \frac{P}{T} \quad (15)$$

377

Where  $P_{\text{H}_2\text{O}}$  is the partial pressure of  $\text{H}_2\text{O}$  in bars. As for  $\text{CO}_2$ , coefficients are provided for NBO/O calculated on a hydrous and anhydrous basis. The hydrous coefficients in the published paper differ from those used in the web app over the last decade (although a new web app using the published coefficients appeared briefly in 2021). VESIcal uses the web app hydrous coefficients by default, as recommended by Iacono-Marziano (written. comms). The coefficients in the published paper were from an older version of the model, and predict extremely high  $\text{H}_2\text{O}$  solubility at  $\sim 10$  kbar ( $> 100\text{wt}\%$ ).

Coefficient	$a_{H_2O}$	$b_{H_2O}$	$B_{H_2O}$	$C_{H_2O}$
Hydrous ( $\pm$ error)	0.53 ( $\pm$ 0.02)	2.35 ( $\pm$ 0.28)	-3.37 ( $\pm$ 0.13)	-0.02 ( $\pm$ 0.02)
Anhydrous ( $\pm$ error)	0.54 ( $\pm$ 0.02)	1.24 ( $\pm$ 0.28)	-2.95 ( $\pm$ 0.17)	0.02 ( $\pm$ 0.02)
Web App	0.52096846	2.11575907	-3.24443335	0.02238884

383

The authors state that the differences between calculations performed with NBO/O calculated on a hydrous and anhydrous basis are relatively small, but that a slightly better fit to experimental data is obtained using the hydrous model (particularly for H<sub>2</sub>O-rich, and CO<sub>2</sub>-poor melts). For completeness, we perform calculations using both versions (referred to as IM-20120-H and IM-2012-A). Interestingly, we show that the anhydrous version is most similar to other models for MORB-like compositions.

The calibration dataset for CO<sub>2</sub> combines the authors experiments with those from a variety of literature studies for mixed H<sub>2</sub>O-CO<sub>2</sub> fluids, spanning temperatures between 1100 and 1400°C, and pressures between 100 and 10,000 bars (but mostly <5000 bars). The calibration dataset for H<sub>2</sub>O incorporates pure H<sub>2</sub>O experiments from the literature (spanning 163–6067 bars, and 1000–1250°C), as well as the experiments on H<sub>2</sub>O-CO<sub>2</sub> fluids used to calibrate the CO<sub>2</sub> expression. Melt compositions are predominantly mafic, spanning subalkaline-alkaline basalts to basaltic andesites (45–57 wt% SiO<sub>2</sub> for mixed H<sub>2</sub>O-CO<sub>2</sub> experiments, and 46–63 wt% SiO<sub>2</sub> for pure H<sub>2</sub>O; Fig. 2).

The empirical nature of the fitting terms incorporating melt composition, pressure and temperature means that users should be cautious when extrapolating this model to conditions lying outside the P-T-X range of the calibration dataset. In particular, Iacono-Marziano et al. (2012) highlight five weaknesses of their model:

1. The effect of melt MgO and FeO contents on CO<sub>2</sub> solubility is poorly constrained, because of the small variation in the concentrations of these oxides in the calibration database.
2. While their compositional terms for the effect of melt composition on CO<sub>2</sub> solubility gives equal weight to Na<sub>2</sub>O and K<sub>2</sub>O, the calibration dataset only includes K<sub>2</sub>O-rich melts with a range of pressures, so the effect of substituting Na and K is poorly constrained.
3. The effect of temperature on the solubility of mixed H<sub>2</sub>O-CO<sub>2</sub> is poorly constrained because the majority of experiments in the calibration dataset were performed at 1200–1300°C.
4. The relative role of molecular H<sub>2</sub>O vs. OH<sup>−</sup> on melt structure, which in turn influences CO<sub>2</sub> solubility, needs to be evaluated further.
5. The model was calibrated assuming that all Fe was Fe<sup>2+</sup>, so calculated solubilities are not sensitive to melt redox (unlike the model of P-2006).

These weaknesses are explored in more detail in sections 5 and 6.

413      **3.7 S–2014 (Shishkina et al., 2014)**

The Shishkina et al. (2014) model calculates the solubility of H<sub>2</sub>O and CO<sub>2</sub> using fully-empirical expressions. Their expression for CO<sub>2</sub> solubility was calibrated on a dataset of mixed H<sub>2</sub>O-CO<sub>2</sub> experiments on predominantly mafic compositions between 1200–1300°C, and 500–5000 bars:

$$\ln[\text{CO}_2]^{\text{ppm}} = 1.150 \ln(P) + 6.71 \Pi^* - 1.345 \quad (16)$$

Where P is the pressure in MPa, and  $\Pi^*$  is a compositional parameter expressed in terms of the cation fractions of 7 species:

$$\Pi^* = \frac{X_{\text{Ca}^{2+}} + 0.8 X_{\text{K}^+} + 0.7 X_{\text{Na}^+} + 0.4 X_{\text{Mg}^{2+}} + 0.4 X_{\text{Fe}^{2+}}}{X_{\text{Si}^{4+}} + X_{\text{Al}^{3+}}} \quad (17)$$

We note for completeness that the expression provided in Shishkina et al. (2014) incorrectly states that CO<sub>2</sub> in equation 16 was in wt%, rather than ppm.

Their expression for H<sub>2</sub>O solubility was calibrated on a dataset of pure H<sub>2</sub>O experiments with mafic to intermediate compositions between 1200–1250°C, and 485–5009 bars. It incorporates a composition parameter expressed in terms of the anhydrous cation fractions of Na and K:

$$\begin{aligned} [\text{H}_2\text{O}]^{\text{wt}\%} = & (3.36 \times 10^{-7} P^3 - 2.33 \times 10^{-4} P^2 - 0.0711 P - 1.1309)(X_{\text{Na}} + X_K) \\ & - 1.2 \times 10^{-5} P^2 + 0.0196 P + 1.1297 \end{aligned} \quad (18)$$

In general, the compositional range of the Shishkina et al. (2014) dataset includes a larger variety of mafic compositions than that of Iacono-Marziano et al. (2012), particularly with respect to alkali-rich, or highly depolymerized melts (Fig. 2). However, as was true for IM–2012, the empirical nature of the compositional term means that extreme care is needed when extrapolating this model beyond the compositional range of the calibration dataset (see section 6).

One caveat of the implementation of this model in VESIcal is the treatment of mixing between CO<sub>2</sub> and H<sub>2</sub>O. Shishkina et al. (2014) note that their experimental data shows evidence for significant non-ideality, with isobars remaining almost horizontal between 0–4 wt% H<sub>2</sub>O (see their Fig. 6). However, the isobars shown on their plots are fitted to experimental data, rather than derived from their equations for CO<sub>2</sub> and H<sub>2</sub>O solubility. These fits cannot be applied to melts with different compositions, and the authors give no guidance as to how to combine their equations for pure CO<sub>2</sub> and pure H<sub>2</sub>O to reproduce this non-ideal behaviour for any given melt composition. Thus, due to an absence of other information, VESIcal treats mixing between H<sub>2</sub>O and CO<sub>2</sub> as ideal in this model. To emphasize this assumption, the H<sub>2</sub>O-CO<sub>2</sub> model called ShishkinaIdealMixing in VESIcal.

430      **3.8 MagmaSat: Ghiorso and Gualda (2015)**

Ghiorso and Gualda (2015) present a comprehensive thermodynamic model (MagmaSat) for mixed H<sub>2</sub>O-CO<sub>2</sub> solubility, calibrated on the most chemically-diverse set of natural silicate melt com-

positions of all the models discussed thus far (Fig. 2). For this reason, it is the default model in VESIcal. MagmaSat uses the equation of state of Z. Duan and Zhang (2006) for the CO<sub>2</sub>-H<sub>2</sub>O fluid, and is the volatile solubility model implemented in rhyolite-MELTS v.1.2 (Gualda et al., 2012). Thus, it is currently the only model which can be directly integrated with phase equilibrium calculations (e.g., to track microlite growth during degassing upon ascent, or post-entrapment modification to melt inclusions). Like P-2006, the model considers the Gibbs free energy of solution using interaction parameters (denoted with a capital  $W$  in this model), although, unlike in P-2006, these terms are independent of pressure (as well as temperature). The exact choice of components differs from that of P-2006, as MagmaSat adapts the formulation from Rhyolite-MELTS (e.g., Mg is considered as Mg<sub>2</sub>SiO<sub>4</sub>, Ghiorso & Sack, 1995). Unlike P-2006, MagmaSat considers the dissolution of CO<sub>2</sub> as both molecular CO<sub>2</sub> and carbonate species (as CaCO<sub>3</sub>), with a set of  $W$  coefficients for each. It is apparent from the percentage errors on these coefficients that the effect of melt composition on carbonate solubility is much better constrained than the effect of melt composition on molecular CO<sub>2</sub> solubility (percentage errors < 10% vs. errors up to 170%, Table 3). MagmaSat assumes that water dissolves entirely as a hydroxyl species, rather than considering both hydroxyl and molecular species. This helps to reduce the number of interaction parameters for volatile-melt species, and seems to be a justified simplification based on available experimental data (see Ghiorso and Gualda, 2015 for a more detailed discussion).

The calibration dataset for H<sub>2</sub>O spans 550–1420°C, and pressures of 0–20,000 bars, and for CO<sub>2</sub> spans 1140–1400 °C and 0–30,000 bars. Importantly, unlike P-2006, MagmaSat is not calibrated for synthetic liquids (e.g., compositions only containing a small number of oxide species like albite), so should only be applied to natural silicate liquid compositions.

### 3.9 A-2019: Allison et al. (2019)

Allison et al. (2019) present thermodynamic models to calculate CO<sub>2</sub> solubility for six different basaltic compositions from Stromboli (alkali basalt), Etna (trachybasalt), Vesuvius (phonotephrite), Erebus (phonotephrite), Sunset Crater (alkali basalt), and the San Francisco Volcanic Field (basaltic andesite, Fig. 2). Specifically, they performed experiments at 1200°C, and ~4000–6000 bars to address the paucity of experiments examining CO<sub>2</sub> solubility in alkali systems at mid crustal pressures. In addition to these experiments, their models for Vesuvius, Etna and Stromboli incorporate experiments from the literature, extending the calibration range of these three models to upper crustal pressures (see Fig. 1). Unlike models which incorporate the effect of changing melt composition empirically (e.g., Newman & Lowenstern, 2002; Iacono-Marziano et al., 2012; Shishkina et al., 2014), Allison et al. (2019) determine the parameters  $\Delta V_r^{0,m}$  (the molar volume change of the condensed components

of the reaction) and  $K_0(P_0, T_0)$  (the equilibrium constant at the reference pressure and temperature) within their thermodynamic equation empirically for each of the six compositions they examine, and create 6 separate models (each of which contains no compositional dependence). The A–2019 models incorporate the modified Redlich-Kwong equation of state provided in the appendix of Holloway and Blank (1994).

Interestingly, Allison et al. (2019) show that CO<sub>2</sub> solubility does not simply scale with total alkali contents. Erebus melts have Na<sub>2</sub>O+K<sub>2</sub>O=8.8 wt%, but dissolve less CO<sub>2</sub> than Etna and Vesuvius melts (Na<sub>2</sub>O+K<sub>2</sub>O=5.2 and 7.8 wt% respectively). They suggest that CaO, MgO and Al<sub>2</sub>O<sub>3</sub> may play a role in the lower solubility of Erebus compared to Etna, but the fact that 5 of the 7 major elements they examine show notable differences between these melt compositions make it difficult to conclusively determine the origin of solubility variations. Ideally, users would apply the A–2019 Etna model to lavas erupted at Etna, the Stromboli model to lavas erupted at Stromboli and so on. The absence of an empirical term for melt composition means that extreme care should be taken when applying these equations to alkaline lavas with different major element contents to those used in the experiments of Allison et al. (2019), even if the lavas originated from one of the 6 volcanoes they examine.

Allison et al. (2019) only present equations for CO<sub>2</sub> solubility, as their experiments weren't designed to have a wide range of H<sub>2</sub>O contents at different pressures, and their high X<sub>CO<sub>2</sub></sub><sup>f</sup> values mean that errors in their fluid fraction measurements propagate into large errors for H<sub>2</sub>O fugacity (relative to the insignificant errors for CO<sub>2</sub> fugacity). In their supplementary spreadsheet, they integrate their CO<sub>2</sub> solubility models with an power law fit for water solubility developed specifically for Etna (Equation 2 of Lesne, Scaillet, Pichavant, Iacono-Marziano, & Beny, 2011). In VESIcal, users can combine any of the A–2019 carbon models with H<sub>2</sub>O models from M–1998, IM–2012 and S–2014, or write their own.

## 4 Model Comparisons

To aid comparisons between models, a number of silicate melt compositions (Table 1) are used to examine the relationship between volatile solubility and pressure, the treatment of mixing between H<sub>2</sub>O and CO<sub>2</sub> (manifested in the shapes of isobars), as well as sensitivity to parameters such as temperature and oxygen fugacity. For basalts, we compare four compositions; two mid-ocean ridge basalts (termed MORB1 and MORB2), one alkali basalt and one arc basalt (grey crosses on Fig. 2). MORB1 from Dixon et al. (1995) has 50.8 wt% SiO<sub>2</sub>, MORB2 from table 3 of Ghiorso and Gualda (2015) has 47.4 wt% SiO<sub>2</sub> (originally from Allan et al., 1989), and the Etna alkali basalt from Allison et al. (2019) has 48.8 wt% SiO<sub>2</sub>. Comparisons between these three compositions were performed at 1200°C.

498 To investigate model sensitivities with relevance to mafic melt inclusion studies in volcanic arcs, we use  
 499 the composition of a Fuego melt inclusion from Lloyd et al. (2013) with 49.7 wt% SiO<sub>2</sub> at 1000°C.

500 For rhyolitic magmas, we perform calculations at 800°C for a rhyolite from Mono Craters (East-  
 501 ern California) and Aluto (African Rift). The Mono Craters composition is a high-Si, metaluminous  
 502 rhyolite with 77.19 wt% SiO<sub>2</sub> from Liu et al. (2005). The Aluto composition is a peralkaline rhyolitic  
 503 melt inclusion with 73.5 wt% SiO<sub>2</sub> from Iddon and Edmonds (2020). The Aluto rhyolite has much  
 504 lower Al<sub>2</sub>O<sub>3</sub> and higher FeO contents than the Mono Craters Rhyolite (Table 1).

**Table 1.** Representative compositions used for comparisons. MORB1 is a Mid-Oceanic Ridge Basalt tholeiite from Dixon et al. (1995). MORB2 is the MORB composition given in Table 3 of Ghiorso and Gualda (2015), originally from Allan et al. (1989). Etna is sample ET-8 from the supplementary information of Allison et al. (2019). Fuego is the composition of a melt inclusion from Lloyd et al. (2013). Mono Craters is from Table 1 of Liu et al. (2005). Aluto rhyolite is the composition of a quartz-hosted melt inclusion from the East African Rift (MI70 from sample MER055A; Iddon & Edmonds, 2020).

Name	MORB1	MORB2	Etna	Fuego	Mono Craters	Aluto Pumice
SiO <sub>2</sub>	50.8	47.4	48.77	49.67	77.19	73.51
TiO <sub>2</sub>	1.84	1.01	1.79	1.17	0.06	0.23
Al <sub>2</sub> O <sub>3</sub>	13.7	17.64	16.98	16.50	12.8	9.18
Fe <sub>2</sub> O <sub>3</sub>	2.1	0.89	2.51	1.65	0.26	1.41
FeO	10.5	7.18	6.44	8.43	0.71	3.81
MnO	0	0	0.18	0.19	0	0.25
MgO	6.67	7.63	6.33	4.38	0.03	0
CaO	11.5	12.44	11.26	7.90	0.53	0.2
Na <sub>2</sub> O	2.68	2.65	3.65	3.37	3.98	4.18
K <sub>2</sub> O	0.15	0.03	1.79	0.79	4.65	4.22
P <sub>2</sub> O <sub>5</sub>	0.19	0.08	0.53	0.22	0	0

#### 505 4.1 Redox sensitivity

506 Before proceeding with these comparisons, it is worth noting that the vast majority of studies  
 507 report whole-rock, melt inclusion and matrix glass compositions in terms of FeO<sub>t</sub>, because the propor-  
 508 tions of FeO vs. Fe<sub>2</sub>O<sub>3</sub> are difficult to determine precisely using common analytical techniques such as  
 509 electron probe microanalysis (EPMA) and x-ray fluorescence (XRF). VolatileCalc-Rhyolite and L-2005  
 510 have no compositional terms, and VolatileCalc-Basalt is only parameterized in terms of the melt SiO<sub>2</sub>  
 511 content, so these 3 models are not sensitive to the choice of FeO vs. Fe<sub>2</sub>O<sub>3</sub> for the representative com-  
 512 positions in Table 1. Similarly, IM-2012 and M-1998 are parameterized using an FeO<sub>t</sub> term, so also  
 513 show no sensitivity to melt redox. S-2014 is technically slightly redox-sensitive for CO<sub>2</sub>, because the  
 514 II\* term is expressed in terms of Fe<sup>2+</sup> species (equation 17). However, given that the model was cal-  
 515 brated assuming Fe<sup>2+</sup>=Fe<sub>T</sub>, any sensitivity to redox is likely spurious, so VESIcal calculates II with

516 Fe<sub>T</sub> by default for consistency with their calibration. In Figure 4, we perform calculations for different  
 517 Fe<sup>3+</sup> ratios for completeness, but the rest of the figures in the manuscript for S–2014 are calculated us-  
 518 ing Fe<sub>T</sub>. H<sub>2</sub>O solubility in S–2014 is not redox sensitive, because the effect of melt composition is only  
 519 parametrized in terms of cation fractions of Na and K (equation 18). Both P–2006 and MagmaSat  
 520 have interaction parameters for Fe<sup>2+</sup> and Fe<sup>3+</sup>-bearing species, so are redox sensitive for both CO<sub>2</sub>  
 521 and H<sub>2</sub>O solubility.

522 We examine the sensitivity of our calculations of volatile solubility to melt redox by performing  
 523 calculations for 0, 10 and 20% Fe<sup>3+</sup> for MORB2, and 0, 30 and 60% Fe<sup>3+</sup> for Etna (the higher re-  
 524 dox accounting for the highly oxidising conditions of experiments on Etna melts, e.g., Lesne, Scaillet,  
 525 Pichavant, & Beny, 2011).

526 Briefly for Etna, pure H<sub>2</sub>O solubility in MagmaSat is relatively insensitive to redox, predicting  
 527 variations in dissolved H<sub>2</sub>O which are well within model error (Fig. 4a). Pure CO<sub>2</sub> solubility in Mag-  
 528 maSat is more redox sensitive than H<sub>2</sub>O, predicting ~1.2–1.3× more CO<sub>2</sub> for 0% Fe<sup>3+</sup> vs. 60% Fe<sup>3+</sup>  
 529 (Fig. 4b). Pure H<sub>2</sub>O solubility in P–2006 shows the same directionality as MagmaSat, but is more  
 530 sensitive to redox (1.8× more H<sub>2</sub>O dissolves at 0.1 kbar for 0% Fe<sup>3+</sup> vs. 60% Fe<sup>3+</sup>, dropping to 1.2×  
 531 at > 2 kbar). Pure CO<sub>2</sub> solubility in P–2006 is extremely redox-sensitive, with melts with 0% Fe<sup>3+</sup> vs.  
 532 60% Fe<sup>3+</sup> dissolving 25× more CO<sub>2</sub> at 0.5 kbar, but 0.5× less at 5 kbar. S–2014 is slightly less redox  
 533 sensitive than MagmaSat for CO<sub>2</sub>.

534 Varying Fe<sup>3+</sup> proportions between 0–20% for MORB2 produces similar patterns as Etna, with  
 535 changes lying within model error for MagmaSat and S–2014, but showing significant differences for  
 536 P–2006 (Fig. 4c-d). Isobars for different redox states for this composition can be found in Supporting  
 537 Figure S2. For the smaller changes in Fe<sup>3+</sup> proportions considered for MORB2, changes in dissolved  
 538 H<sub>2</sub>O and CO<sub>2</sub> contents for MagmaSat and S–2014 are well within model uncertainty (generally stated  
 539 as 10–20%). In contrast, P–2006 shows changes in dissolved CO<sub>2</sub> which are significantly larger than  
 540 quoted errors on solubility models.

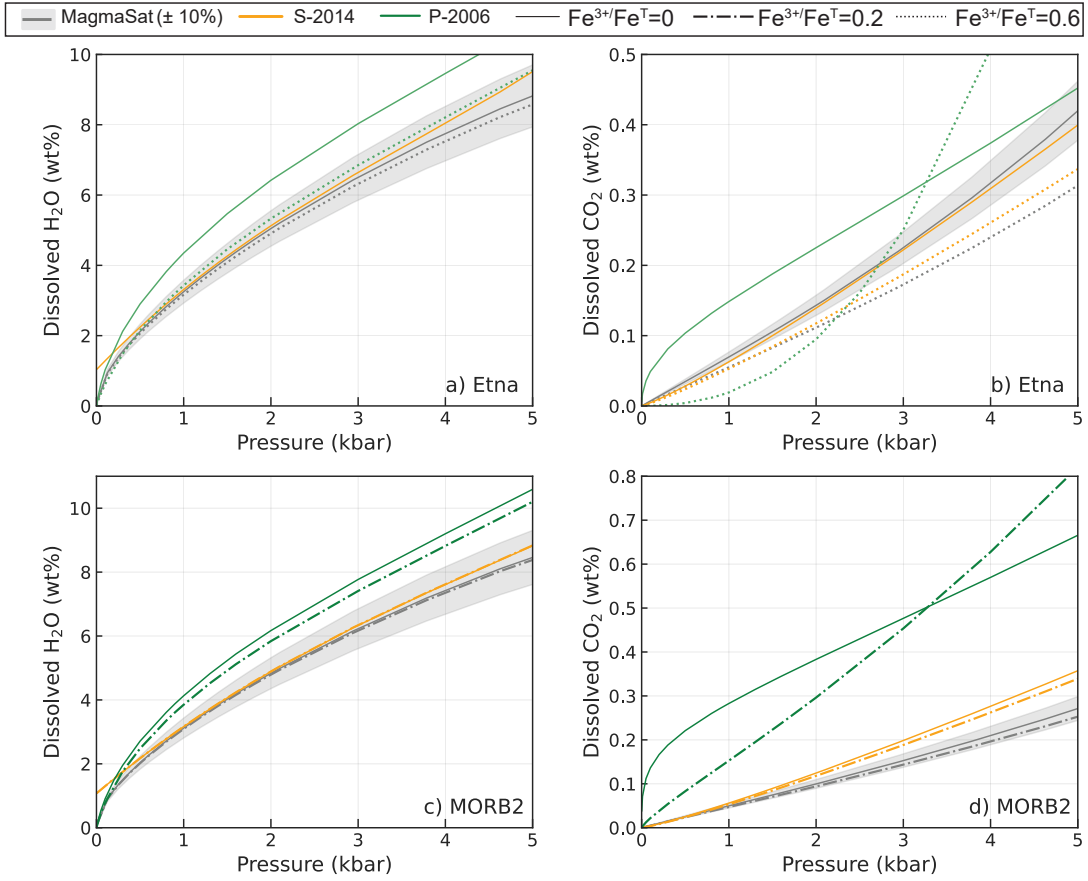


**Figure 4.** Relationship between volatile solubility and the proportion of  $\text{Fe}^{3+}$  for: a-b) the Etna composition at  $1200^{\circ}\text{C}$ ; c-d) the MORB2 composition at  $1200^{\circ}\text{C}$ . VESIcal uses  $\text{FeO}_t$  in S-2014 to calculate  $\Pi^*$  for consistency with the calibration of this model. Here, dashed and dotted lines show the results from calculations where  $\text{FeO}_t$  is multiplied by  $\text{Fe}^{2+}/\text{Fe}_T$ , to show the results that would be obtained if VESIcal calculated  $\Pi^*$  using only  $\text{Fe}^{2+}$ . Isobars for MORB2 and lines for intermediate  $\text{Fe}^{3+}$  ratios for each composition are shown in Supporting Fig. S2.

The different sensitivities of MagmaSat and P-2006 are apparent from examining the interaction coefficients in Table 3. In MagmaSat, the  $W_{\text{Fe}_2\text{O}_3, \text{H}_2\text{O}}$  coefficient is only  $1.6\times$  bigger than  $W_{\text{Fe}_2\text{SiO}_4, \text{H}_2\text{O}}$  ( $\sim 50$  vs.  $31$ ), and these two coefficients overlap within  $\pm 1.5\sigma$  of the uncertainty of these coefficients. This accounts for the relatively weak effect of redox on calculated  $\text{H}_2\text{O}$  solubility. For the  $\text{CaCaO}_3$  component representing the carbonate ion, the coefficients have similar magnitudes, but opposite signs ( $W_{\text{Fe}_2\text{O}_3, \text{CaCO}_3} \sim 66$ ,  $W_{\text{Fe}_2\text{SiO}_4, \text{CaCO}_3} \sim -73$ ), and this difference is much larger than the error on the coefficients (accounting for the stronger effect of melt redox on  $\text{CO}_2$  solubility compared with  $\text{H}_2\text{O}$ ). The  $\text{Fe}_2\text{O}_3$  and  $\text{Fe}_2\text{SiO}_4$  coefficients for the  $\text{CO}_2$  component (which becomes

more dominant in more evolved compositions) are also significantly different outside the quoted error but have the same sign ( $W_{Fe_2O_3, CO_2} \sim -32$ ,  $W_{Fe_2SiO_2, CO_2} \sim -3$ ).

In P–2006, the  $w_{H_2O-FeO}^0$  coefficient is of similar magnitude, but opposite sign to  $w_{H_2O-Fe_2O_3}^0$  ( $1.4 \times 10^5$  vs.  $-2 \times 10^5$ ), and clearly distinct outside the error on each coefficient. This accounts for the slightly stronger sensitivity of H<sub>2</sub>O in P–2006 to redox compared with MagmaSat. In stark contrast to all the comparisons thus far, the  $w_{CO_2-Fe_2O_3}^0$  coefficient is  $>200\times$  larger than  $w_{CO_2-FeO}^0$ . In fact,  $w_{CO_2-Fe_2O_3}^0$  is  $\sim 8\times$  higher than the next largest coefficient, suggesting that for a given mole fraction in the melt, it has the largest effect on carbonate ion solubility. The  $w_{CO_2-Fe_2O_3}^1$  coefficient in P–2006 model, which becomes more dominant at higher pressures, has the opposite sign to that for  $w_0$ . This accounts for the fact that at low pressures (<3 kbar), increasing proportions of Fe<sup>3+</sup> cause a decrease in CO<sub>2</sub> solubility, while at higher pressures, increasing proportions of Fe<sup>3+</sup> cause CO<sub>2</sub> solubility to increase.

It is difficult to trust the extreme sensitivity of CO<sub>2</sub> in P–2006 to redox given the large uncertainty associated with the proportions of Fe<sup>3+</sup> in volatile solubility experiments. For example, S–2014 note that only 7 of the 48 experiments in their calibration dataset contain non-zero values of Fe<sub>2</sub>O<sub>3</sub>, which is why they choose to calibrate the model using FeO<sub>T</sub>. In the P–2006 dataset, only 6 studies used in the calibration directly determined the proportion of Fe<sup>3+</sup>, and a further 9 reported the experimental oxygen fugacity. Thus, for the vast majority of their experimental calibration dataset, Papale et al. (2006) calculate the proportion of Fe<sup>3+</sup> assuming the oxygen fugacity is controlled by the H<sub>2</sub>O-H<sub>2</sub> equilibrium at the stated experimental conditions. However, this method requires accurate measurements of fluid composition, is affected by Fe and H<sup>+</sup>-loss during experiments, and it is unclear how applicable this method is for mixed H<sub>2</sub>O-CO<sub>2</sub> experiments (Botcharnikov et al., 2006). The P–2006 calibration dataset contains some very surprising values: in the calibration dataset for pure CO<sub>2</sub> experiments, the experiments of Fogel and Rutherford (1990) have been allocated Fe<sup>3+</sup>/Fe<sub>T</sub> ratios of  $\sim 0.9\text{--}1$ , despite the authors debating whether their experiments were actually reducing enough to stabilize a CO species. Similarly, the mixed CO<sub>2</sub>-H<sub>2</sub>O experiments of Paonita et al. (2000) have been allocated Fe<sup>3+</sup>/Fe<sub>T</sub> ratios of  $\sim 0.9$ , despite the starting materials having Fe<sup>3+</sup>/Fe<sub>T</sub> ratios of 0.01 for rhyolites and 0.45 for basalts. Although it might seem that a few such studies will not influence the overall result, it is worth noting that the coefficients for CO<sub>2</sub> are relatively underconstrained. While there are 10 coefficients for H<sub>2</sub>O calibrated using 865 datapoints of pure-H<sub>2</sub>O solubility, there are 20 coefficients for CO<sub>2</sub>, and only 173 datapoints for pure-CO<sub>2</sub> solubility and 84 for mixed fluids. In particular, the highly oxidising Fe<sup>3+</sup>/Fe<sub>T</sub> ratios calculated assuming H<sub>2</sub>O-H<sub>2</sub> equilibrium are more concentrated in experiments with low CO<sub>2</sub> contents and pressures, making it difficult to deconvolve

582 the differential effects of these parameters in a model with a large number of coefficients being cali-  
 583 brated on a relatively small calibration dataset.

584 Finally, we wish to draw attention to the very large error on the CO<sub>2</sub>-FeO coefficients ( $w_0 \sim$   
 585 800% and  $w_1 \sim 1500\%$ ), but the relatively small error on the CO<sub>2</sub>-Fe<sub>2</sub>O<sub>3</sub> coefficients in the P-2006  
 586 model ( $w_0 \sim 9\%$  and  $w_1 \sim 9\%$ ; Fig. 3). It is likely that the error on the FeO coefficient accurately  
 587 represents the large uncertainty on the effect of melt redox on CO<sub>2</sub> solubility, while the 9% error on  
 588 the CO<sub>2</sub>-Fe<sub>2</sub>O<sub>3</sub> coefficients is unrealistic, given the very large uncertainties associated with estimating  
 589 Fe<sup>3+</sup>/Fe<sub>T</sub> proportions from experiments which did not report any information on redox conditions.

590 In sections 4.2 to 5, we show calculations using the Fe<sup>3+</sup>/Fe<sub>T</sub> proportions in Table 1, as these  
 591 best-estimates for each center are representative of what a user would select when calculating melt  
 592 inclusion saturation pressures, dissolved volatile contents etc. For MORB1, MORB2, and Fuego, these  
 593 proportions are from the original publications. For Etna, Fe<sub>2</sub>O<sub>3</sub> was calculated from FeO<sub>t</sub> assuming  
 594 Fe<sup>3+</sup>/Fe<sub>T</sub>=0.26 after Gaborieau et al. (2020). For Mono Craters and the Aluto pumice, Fe<sup>3+</sup>/Fe<sub>T</sub> was  
 595 set at 0.25 based on available data on other rhyolites (e.g., Ghiorso and Gualda, 2015), and modelling  
 596 studies of the fractional crystallization path at Aluto (Gleeson et al., 2017).

## 597 4.2 Mafic Compositions

### 598 4.2.1 Pure H<sub>2</sub>O

599 The 7 models applicable to H<sub>2</sub>O in basaltic systems predict a sharp rise in pure H<sub>2</sub>O solubility with  
 600 increasing pressure (Fig. 5). For all three melt compositions, S-2014, IM-2012-A, VolatileCalc-Basalt,  
 601 and M-1998 predict H<sub>2</sub>O concentrations within  $\pm 10\%$  of MagmaSat (grey envelope) between  $\sim 1$ – $5$   
 602 kbar. For MORB1 and MORB2, IM-2012-H begins to deviate to higher H<sub>2</sub>O contents than Mag-  
 603 maSat at  $> 1$  kbar. For Etna, IM-2012-H follows a similar trajectory between 0–3 kbar to the solu-  
 604 bility model of Lesne, Scaillet, Pichavant, Iacono-Marziano, and Beny (2011) developed specifically  
 605 for Etna melts (yellow line, Fig. 5d). In contrast, P-2006 plots to substantially higher H<sub>2</sub>O solubili-  
 606 ties compared to all other models at  $> 0.5$  kbar (although P-2006 and IM-2012-H intercept at higher  
 607 pressures).

608 The fact that IM-2012-H predicts higher H<sub>2</sub>O solubility relative to the cluster of other mod-  
 609 els lying within the error window of MagmaSat is an interesting observation. Iacono-Marziano et al.  
 610 (2012) favour their hydrous model, particularly for CO<sub>2</sub>-poor, H<sub>2</sub>O-rich melts, based on regressions  
 611 between predicted and measured H<sub>2</sub>O contents, and by comparing the two models to experiments  
 612 conducted between 1 and 4 kbar on Etna melts (their Figure 7a). However, their Figure 8c, which  
 613 compares dissolved volatile contents calculated by the model for the entire calibration dataset, shows  
 614 that predicted H<sub>2</sub>O contents using the hydrous version are overestimates for experimental products

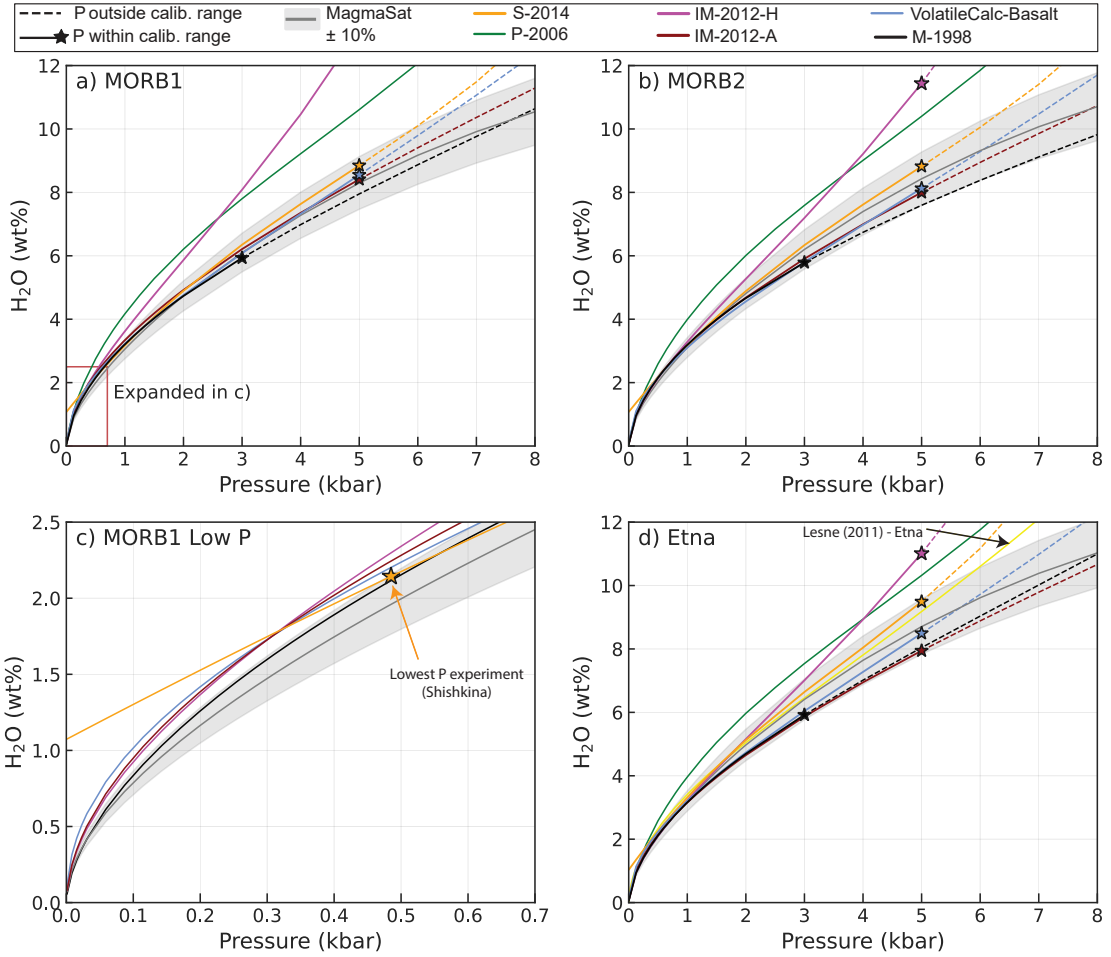


**Figure 5.** Relationship between pure  $\text{H}_2\text{O}$  solubility and pressure for MORB1, MORB2 and Etna melts at  $1200^\circ\text{C}$ . The grey field shows a  $\pm 10\%$  error window around MagmaSat. Model lines are dashed when extrapolated above the recommended pressure range. The low pressure region of a) is expanded in c), emphasizing the non-zero solubility of  $\text{H}_2\text{O}$  at  $P=0$  bar in the S-2014 model.

with  $>6\text{--}7$  wt%  $\text{H}_2\text{O}$  (although these predictions still lie within the  $\sim 17\%$  error associated with their  $\text{H}_2\text{O}$  model). Our comparisons suggest that the anhydrous model is most similar to other models, so should not automatically be discounted in favour of the hydrous model.

Another notable oddity is the nearly linear trajectory of  $\text{H}_2\text{O}$  vs.  $P$  in S-2014 at  $<0.5$  kbar, causing this model to predict a non-zero solubility of  $\text{H}_2\text{O}$  at 0 bar (Fig. 5c). This contrasts with the power-law shapes followed by the other models which intercept very close to the origin. This anomalous behaviour is because the S-2014 equation for  $\text{H}_2\text{O}$  solubility (equation 18) simplifies at  $P=0$  to:

$$[\text{H}_2\text{O}]^{\text{wt}\%} = -1.1309(\text{X}_{\text{Na}} + \text{X}_{\text{K}}) + 1.1297 \quad (19)$$

618 In the S–2014 calibration dataset,  $X_{Na} + X_K$  varies from 0.05 to 0.25, which corresponds to solubilities  
 619 of 0.85–1.07 wt%  $H_2O$  at 0 bar. This demonstrates the issue with extrapolating empirical expressions  
 620 beyond the calibration range (the lowest pressure experiment in the calibration dataset of S–2014 was  
 621 conducted at 485 bar). When combined with the assumption of ideal mixing used in VESIcal, this  
 622 non-zero solubility of  $H_2O$  at 0 bar results in S–2014 predicting unusual degassing paths and isobar  
 623 shapes relative to other models. For example, if a melt has <1 wt%  $H_2O$ , S–2014 predicts that the  
 624 co-existing fluid contains no  $H_2O$ , despite abundant evidence that volcanic plumes in low  $H_2O$  systems  
 625 such as Hawai'i are dominated by  $H_2O$  at low pressures (Gerlach, 1986). It also causes isobars to be  
 626 entirely flat at low  $H_2O$  contents (see section 4.2.2, Fig. 6).

627 Overall, excluding P–2006 and IM–2012–H based on their higher predictions of  $H_2O$  solubility,  
 628 and S–2014 based on anomalous behavior at low  $H_2O$  contents, the remaining four solubility models  
 629 predict dissolved  $H_2O$  concentrations within error of one another at pressures lower than the upper  
 630 calibration limit. This likely reflects the relatively small effect of melt composition of  $H_2O$  solubility,  
 631 meaning that more recent models calibrated on a wider compositional range display similar behavior  
 632 to older models (G. Moore & Carmichael, 1998; Papale et al., 2006). The larger deviation between  
 633 models at higher pressures reflect the fact that very few pure- $H_2O$  solubility experiments have been  
 634 performed at > 5 kbar (Table 1). One reason for this shortage of higher pressure experimental data  
 635 results from the fact that it is very difficult to quench silicate melts with >9 wt%  $H_2O$  to a glass phase  
 636 which can be analysed by FTIR or SIMS (Gavrilenko et al., 2019; Mitchell et al., 2017).

#### 637 4.2.2 Mixed $H_2O$ - $CO_2$

638 The majority of experiments used to calibrate expressions for pure- $CO_2$  solubility contained dis-  
 639 solved  $H_2O$  and  $CO_2$  (e.g., Iacono-Marziano et al., 2012; Shishkina et al., 2014; Allison et al., 2019),  
 640 requiring authors to assess  $H_2O$ - $CO_2$  mixing behaviour to determine the solubility of pure- $CO_2$  fluids.  
 641 Thus, it makes sense to consider the treatment of mixing between  $CO_2$  and  $H_2O$  species in each model  
 642 before considering predictions of pure  $CO_2$  solubility which are affected by these assumptions. The  
 643 treatment of  $H_2O$ - $CO_2$  mixing is best demonstrated using isobar diagrams, which show the solubility  
 644 of  $H_2O$  and  $CO_2$  in a given silicate melt composition at a given pressure for proportions of  $X_{H_2O}^f$  in  
 645 the co-existing fluid ranging from 0 (interception with the y axis) to 1 (interception with the x axis).  
 646 The treatment of mixed fluids differs quite considerably in each model.

647 VolatileCalc-Basalt models mixed fluids under the assumption of Henrian (ideal) mixing in the  
 648 fluid and melt phase. Thus, the addition of  $H_2O$  always causes the solubility of  $CO_2$  to decrease (and  
 649 vice versa), and isobars possess a negative gradient, with a slightly sloping plateau at low  $H_2O$  con-  
 650 tents merging into a concave-down shape (Fig. 6).

S–2014 does not provide an equation for the treatment of non-ideal mixing, despite their experiments showing that increasing H<sub>2</sub>O contents at high pressure cause almost no change in CO<sub>2</sub> solubility. Using the assumption of ideal mixing in VESIcal, S–2014 isobars exhibit a flat plateau at low H<sub>2</sub>O contents, merging into a negative slope at higher H<sub>2</sub>O contents. This flat plateau results from the fact that there are no partial pressures at which S–2014 yields H<sub>2</sub>O < 1 wt%, so the y co-ordinate for lower H<sub>2</sub>O contents is equal to the solubility of pure CO<sub>2</sub>.

P–2006 is fully non-ideal, which causes isobars to have complex shapes, exhibiting both positive and negative gradients. In detail, the shape of isobars calculated using P–2006 differ as a function of both melt composition and temperature (see Fig. 12 of Papale, 1999). For the basaltic compositions considered here, isobars show a sharp increase to higher CO<sub>2</sub> contents at very low H<sub>2</sub>O contents (Fig. 6a, c), because the model predicts a decrease in CO<sub>2</sub> solubility following the addition of small quantities of H<sub>2</sub>O.

IM–2012–A and IM–2012–H incorporate empirical representations of non-ideality through the inclusion of a term for the molar fraction of H<sub>2</sub>O in the melt in their expression for CO<sub>2</sub> solubility (equation 11). This means that these models predict that maximum CO<sub>2</sub> solubility occurs at non-zero H<sub>2</sub>O concentrations, causing isobars to display prominent domed shapes (Fig. 6). Isobars calculated using IM–2012–A show a more extreme peak than IM–2012–H, because of the difference in the sign and magnitude of the d<sub>H<sub>2</sub>O</sub> coefficient combined with the differences between NBO/O calculated on a hydrous and anhydrous basis (see Supporting Information for further detail).

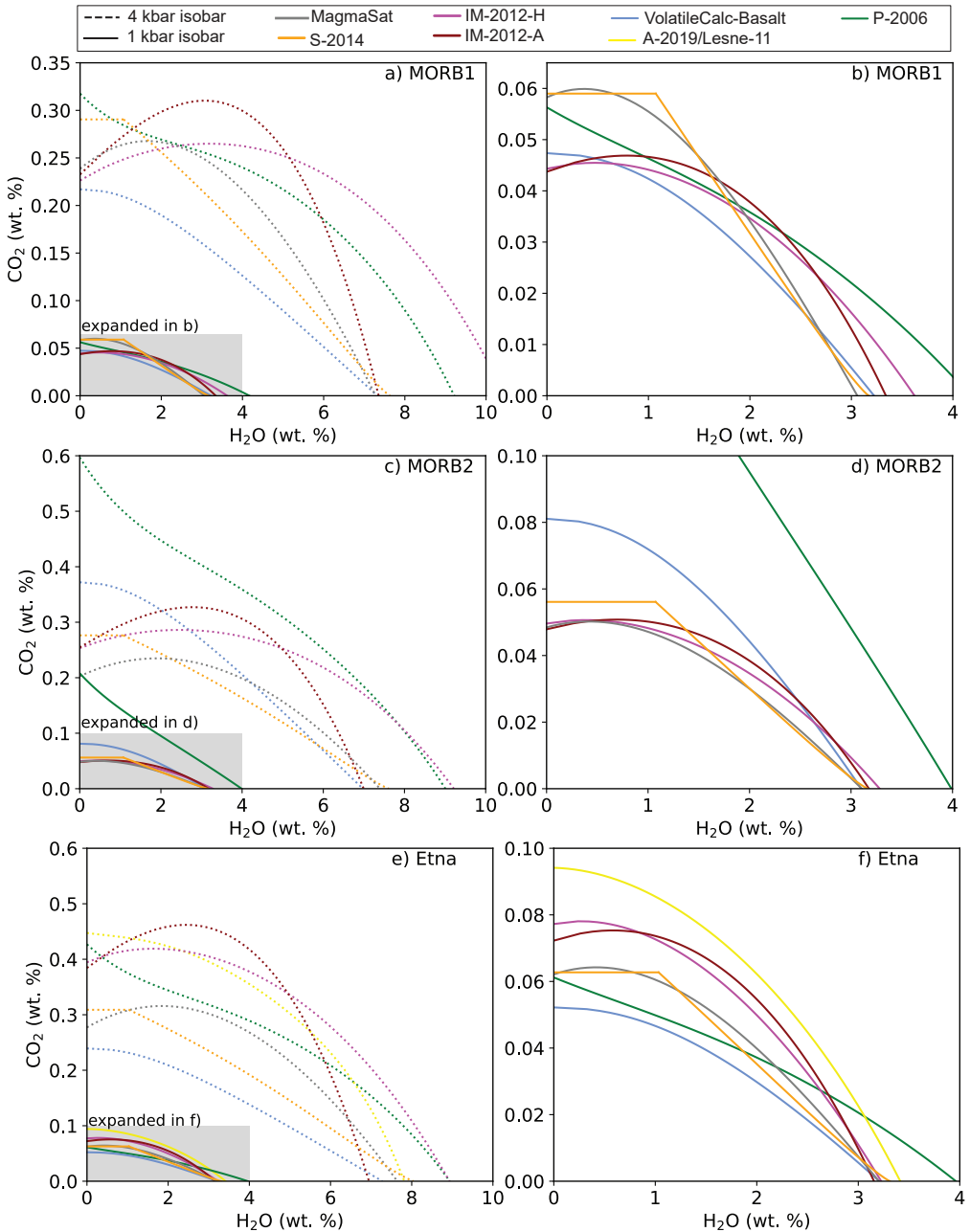


**Figure 6.** 1 and 4 kbar isobars for MORB1 (a-b) and MORB2 (c-d) and Etna (e-f) at 1200°C. The 1 kbar isobar is expanded in b), d) and e). The distinctive shapes of isobars from different models reflects different treatment of H<sub>2</sub>O-CO<sub>2</sub> mixing. This is most apparent at higher pressures. The prominent plateau at <1 wt% H<sub>2</sub>O for S-2014 at all pressures results from the non-zero solubility of H<sub>2</sub>O at low pressures.

Like P-2006, MagmaSat is fully non-ideal. However, unlike P-2006, the treatment of non-ideality in MagmaSat predicts that the addition of small amounts of H<sub>2</sub>O always causes the solubility of CO<sub>2</sub>

672 to increase (so isobars peak at non-zero H<sub>2</sub>O concentrations; Fig. 6, c). This peak becomes more pro-  
 673 nounced at higher pressures, but is generally smaller than that predicted by IM–2012.

674 These different mixing assumptions result in large discrepancies between the predicted volatile  
 675 solubilities for melts in equilibrium with H<sub>2</sub>O-CO<sub>2</sub> fluids, particularly at higher pressures where non-  
 676 ideal behaviour is more pronounced. For example, while IM–2012–A predicts similar pure CO<sub>2</sub> and  
 677 pure H<sub>2</sub>O solubilities to VolatileCalc-Basalt and MagmaSat for MORB1 at 4 kbar (interception with  
 678 x and y axis on Fig. 6a), IM–2012–A predicts that melts with ~ 4 wt% H<sub>2</sub>O can dissolve more than  
 679 twice as much CO<sub>2</sub> as that predicted by VolatileCalc-Basalt.

#### 680       4.2.3 Pure CO<sub>2</sub>

681 All basaltic compositions and models show a large increase in the solubility of pure CO<sub>2</sub> with  
 682 increasing pressure (Fig. 7). The solubility of pure CO<sub>2</sub> is approximately an order of magnitude lower  
 683 than for H<sub>2</sub>O (compare Fig. 7 with Fig. 5). This solubility difference accounts for the fact that Mid  
 684 Oceanic Ridge (MOR) magmas, which have similar concentrations of H<sub>2</sub>O and CO<sub>2</sub> (~ 0.07 wt%  
 685 H<sub>2</sub>O, 0.1–0.2 wt% CO<sub>2</sub>; Le Voyer et al., 2019), are almost always CO<sub>2</sub> saturated during crustal stor-  
 686 age (Saal et al., 2002) but only exsolve measurable quantities of H<sub>2</sub>O if erupted at very low pressures  
 687 (Le Voyer et al., 2019).

688 For MORB1, IM–2012–A and H, and VolatileCalc-Basalt lie within, or close to the ± 10% error  
 689 window on MagmaSat at <5 kbar, and S–2014 lie within ± 20%. The deviation at higher pressures  
 690 is expected, because only P–2006 and MagmaSat are calibrated on large numbers of experiments per-  
 691 formed at > 5 kbar (Fig. 1). For example, the relationship between II and CO<sub>2</sub> solubility of Dixon  
 692 (1997) used in VolatileCalc-Basalt was based on experiments at 1 kbar, and Newman and Lowenstern  
 693 (2002) suggest that it should not be extrapolated above 5 kbar. Similarly, only the experiments of  
 694 Jakobsson (1997) in the IM–2012 database were conducted at >5 kbar, and there are no experiments  
 695 in the calibration dataset of S–2014 performed at >5 kbar. Unlike for pure H<sub>2</sub>O, IM–2012–A and H  
 696 predict very similar pure CO<sub>2</sub> solubilities to one another. This reflects the fact the coefficients for CO<sub>2</sub>  
 697 between these 2 model versions are very similar (apart from the d<sub>H<sub>2</sub>O</sub> term, which is multiplied by a  
 698 zero when calculating pure CO<sub>2</sub> solubility). In contrast, P–2006 plots to significantly higher pressures  
 699 than the other models (~ 2× higher at ~8 kbar).

700 MORB2 shows a significantly larger discrepancy between different models at all pressures (Fig.  
 701 7b), although S–2014, IM–2012–H and –A follow very similar trajectories at <5 kbar. Most notably,  
 702 P–2006 predicts that MORB2 dissolves ~3370 ppm CO<sub>2</sub> at 2 kbar while MagmaSat predicts only  
 703 ~950 ppm (factor of 3.5×). VolatileCalc-Basalt also predicts higher CO<sub>2</sub> solubility relative to Mag-  
 704 maSat by a factor of 1.8× at 2 kbar.

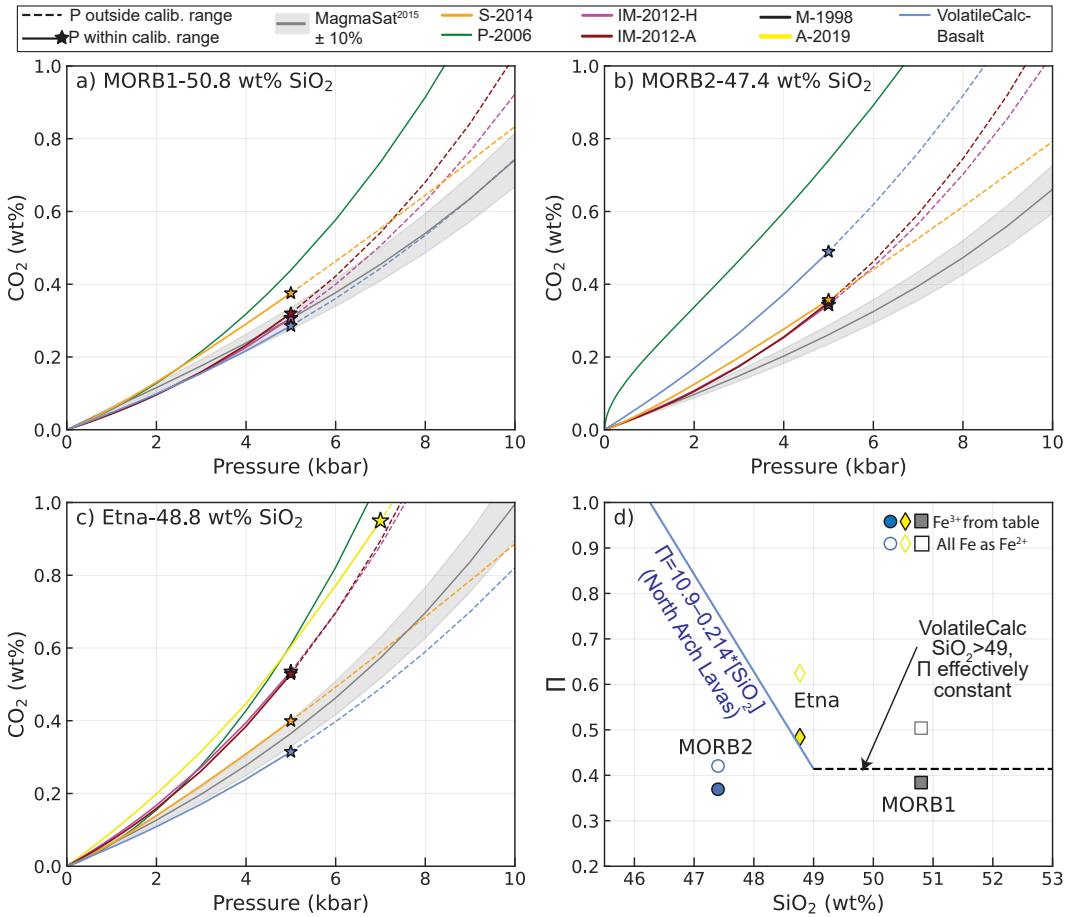


**Figure 7.** Relationship between pure CO<sub>2</sub> solubility and pressure for three mafic melts at 1200°C: a) MORB1 from Dixon et al. (1995), b) MORB2 from Ghiorso and Gualda (2015), and c) Etna from Allison et al. (2019). Models extrapolated beyond their calibrated pressure range are shown as dashed lines, with the colored star marking the recommended upper calibration limit. d) The relationship between  $\Pi$  and SiO<sub>2</sub> defined by the North Arch lavas is shown in blue (Dixon, 1997). Generally, VolatileCalc-Basalt is applied to melts with >49 wt% SiO<sub>2</sub> by setting SiO<sub>2</sub>=49 wt%; the black dashed line represents this extrapolation. These simplified relationships incorporated into VolatileCalc-Basalt (blue and black lines) underestimate the true  $\Pi$  value for Etna, and overestimate it for MORB2.

The high CO<sub>2</sub> solubility predictions by P-2006 relative to other models and experimental measurements has also been noted by Shishkina et al. (2010), Shishkina et al. (2014) and Mangan et al. (2021). This may result from the fact that the P-2006 has a negative compressibility for the CO<sub>2</sub> fluid (Ghiorso & Gualda, 2015). Alternatively, it may reflect the large errors on the CO<sub>2</sub> *w* coefficients, meaning that the effect of melt composition is uncertain, accounting for the larger discrepancy for MORB1 vs. MORB2 compared to other models. Finally, Shishkina et al. (2010) suggest that the

711 overprediction of CO<sub>2</sub> solubility by P-2006 may result from the inclusion of anomalously high CO<sub>2</sub>  
712 contents from the experiments of Freise (2004) in the calibration dataset of P-2006 (these values have  
713 now been revised to lower numbers, as the original FTIR thickness correction factor is thought to have  
714 been incorrect).

715 The fact that VolatileCalc-Basalt plots close to other models for MORB1 but not MORB2 is  
716 a good example of the main caveat of the  $\Pi$ -SiO<sub>2</sub> simplification used to account for the effect of  
717 melt composition on CO<sub>2</sub> solubility. For melts with 40–49 wt% SiO<sub>2</sub>, VolatileCalc-Basalt assumes  
718 that the relationship between CO<sub>2</sub> solubility and SiO<sub>2</sub> is identical to that defined by the North Arch  
719 lavas, shown in  $\Pi$  vs. SiO<sub>2</sub> space as a blue line in Fig. 7d. This is a reasonable approximation for the  
720 MORB1 composition, which has a  $\Pi$  value similar to North Arch Lavas with 49 wt% SiO<sub>2</sub>. However,  
721 the MORB2 composition lies significantly below the line defined by North Arch lavas, so has a lower  
722  $\Pi$  value, and therefore a lower CO<sub>2</sub> solubility at a given SiO<sub>2</sub> content compared to the North Arch  
723 Lavas. Thus, VolatileCalc-Basalt likely overpredicts the solubility of CO<sub>2</sub> in this melt composition.

724 Furthermore, VolatileCalc-Basalt predicts that MORB2 dissolves  $\sim$ 1.7 times more CO<sub>2</sub> at a  
725 given pressure than MORB1. This is because MORB2 has 3.4 wt% less SiO<sub>2</sub> than MORB1, and  
726 VolatileCalc-Basalt predicts that CO<sub>2</sub> solubility increases drastically with decreasing SiO<sub>2</sub>. How-  
727 ever, if the full  $\Pi$  expression of Dixon (1997) were used, MORB1 and MORB2 would have very similar  
728 CO<sub>2</sub> solubility, as they have similar  $\Pi$  values despite different SiO<sub>2</sub> contents. P-2006 also predicts that  
729 MORB2 dissolves 5–6× more CO<sub>2</sub> at 0.4 kbar, and 1.9× more at 4 kbar than MORB1. In contrast,  
730 the models of S-2014, IM-2012, and MagmaSat predict that MORB1 and MORB2 dissolve similar  
731 amounts of CO<sub>2</sub> (MORB2/MORB1= $\sim$ 0.99×,  $\sim$ 1.125× and  $\sim$ 0.81–0.89× respectively). These three  
732 more recent models utilize significantly larger basaltic calibration datasets to parametrize the effect of  
733 multiple oxide species melt on CO<sub>2</sub> solubility (Fig. 2), so likely predict more realistic solubility rela-  
734 tionships than VolatileCalc-Basalt and P-2006. CO<sub>2</sub> solubility in melt compositions that do not follow  
735 a similar trajectory in  $\Pi$ -SiO<sub>2</sub> space as the North Arch Lavas (Fig. 7d) is unlikely to be accurately  
736 predicted by VolatileCalc-Basalt.

737 There is also significant deviation between different models for Etna melts (Fig. 7c), which is far  
738 greater than that observed for H<sub>2</sub>O (Fig. 5). The A-2019 model, developed specifically for the com-  
739 position of Etna magmas, predicts much higher CO<sub>2</sub> solubility at a given pressure than VolatileCalc-  
740 Basalt, S-2014, and MagmaSat, while P-2006 and IM-2012-H and -A follow similar trajectories to  
741 A-2019. The success of both IM-2012 models likely reflects the large number of alkaline composi-  
742 tions in their calibration dataset, including some from Etna. VolatileCalc-Basalt predicts the lowest  
743 CO<sub>2</sub> solubility (factor of 0.5–0.6× that of A-2019). The calculated  $\Pi$  value for Etna lies significantly

above the line defined by North Arch lavas (so VolatileCalc-Basalt predicts lower CO<sub>2</sub> solubility; Fig. 7d). However, even the full Π expression of Dixon (1997) is unlikely to be successful, because alkaline magmas show considerable variation in CO<sub>2</sub> solubility at a given Π value (Allison et al., 2019). As S–2014’s expression for CO<sub>2</sub> solubility incorporates a Π\* term very similar to the Π term of Dixon (1997), the deviation of this model from that of A–2019 (0.6–0.7×) may also result from variations in CO<sub>2</sub> solubility that are not incorporated by this simplified melt composition parameter (Allison et al., 2019).

Interestingly, MagmaSat also underpredicts CO<sub>2</sub> concentrations at a given pressure relative to A–2019 by a factor of 0.6–0.7×, despite incorporating CO<sub>2</sub> experiments on Etna basalts from Lesne, Scaillet, Pichavant, and Beny (2011) and Iacono-Marziano et al. (2012) in its calibration dataset. This is a good example of the main pitfall of comprehensive models such as MagmaSat and P–2006 which can predict volatile solubility across the entire range of natural silicate melt compositions (Papale et al., 2006). For any specific melt composition, the model is highly unlikely to be as well tuned as models calibrated on melts from a specific volcanic center (e.g., Allison et al., 2019) or heavily weighted towards a specific region of compositional space (e.g., Iacono-Marziano et al., 2012, for alkali basalts). Tuning MagmaSat to provide a better fit to Etna would almost certainly cause this model to show larger discrepancies for experiments conducted on different melt compositions.

### 4.3 Silicic Compositions

#### 4.3.1 Pure H<sub>2</sub>O

All five H<sub>2</sub>O models calibrated for silicic magmas (MagmaSat, P–2006, L–2005, VolatileCalc-Rhyolite and M–1998) predict very similar H<sub>2</sub>O concentrations at <1–1.5 kbar for the Mono Craters rhyolite composition (Fig. 8a, Table 1). At higher pressures, P–2006, and to a much lesser extent L–2015, show a smaller increase in H<sub>2</sub>O solubility with pressure compared to MagmaSat, M–1998 and VolatileCalc-Rhyolite (the difference in H<sub>2</sub>O solubility between models reaches ~4 wt% at 5 kbar). As discussed for basalt, the large discrepancies at higher pressures and H<sub>2</sub>O contents likely results from an absence of experimental constraints because of challenges related to quenching melts with >6–9 wt% H<sub>2</sub>O (Gavrilenko et al., 2019).

L–2005 and VolatileCalc-Rhyolite have no compositional dependence, so follow identical trajectories for the Mono Craters rhyolite and the peralkaline Aluto rhyolite (Fig. 8b). MagmaSat and M–1998 also show very similar trends for these two compositions. In contrast, the P–2006 model predicts higher H<sub>2</sub>O concentrations at <2 kbar than the other models for Aluto (and higher H<sub>2</sub>O concentrations than predicted for Mono Craters). At >3 kbar, the P–2006 Aluto model shows a rapid reduction

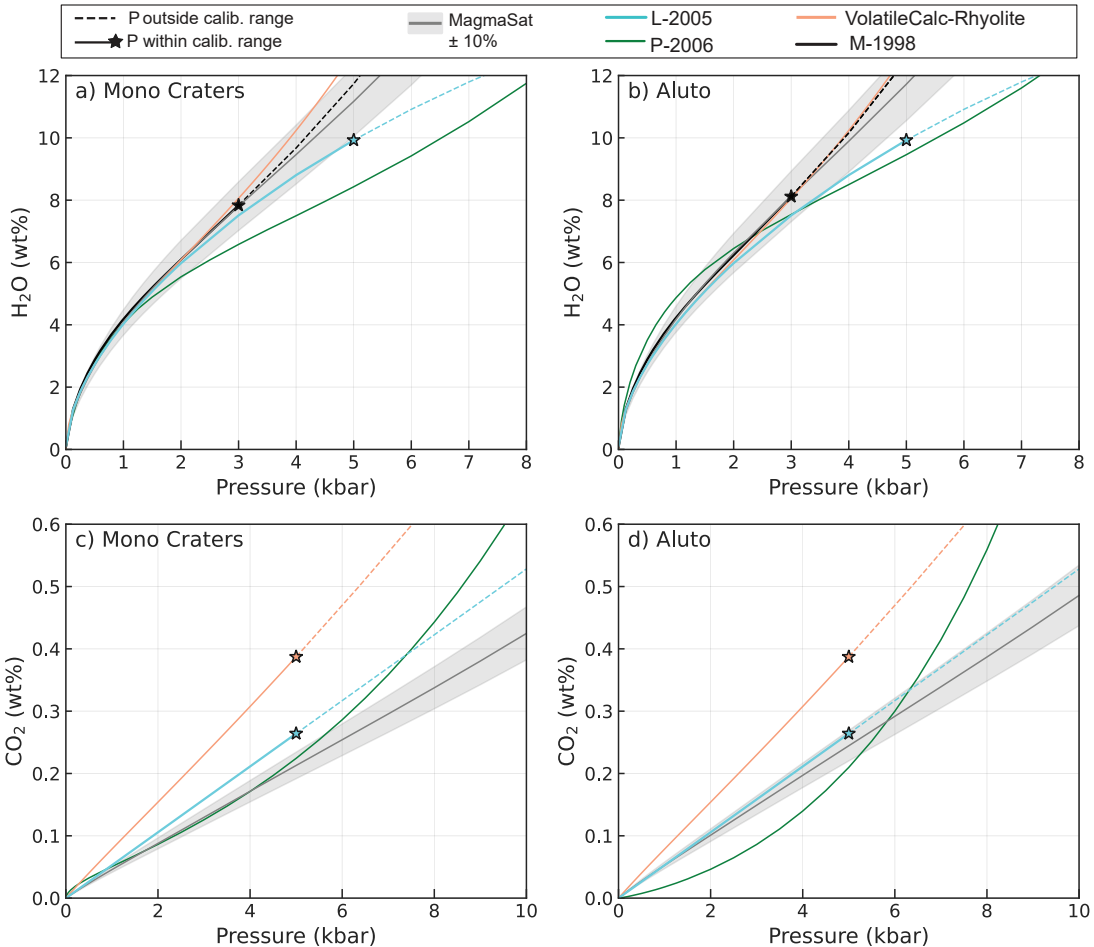


**Figure 8.** Relationship between pure H<sub>2</sub>O (a-b) and pure CO<sub>2</sub> (c-d) solubility and pressure at 800°C for the Mono Lake rhyolite from Liu et al. (2005), and a peralkaline Rhyolite from Aluto in the East African Rift (Iddon and Edmonds, 2020). Models extrapolated beyond their calibrated pressure range are shown as dashed lines, with the colored star marking the recommended upper calibration limit.

in gradient, and predicts lower H<sub>2</sub>O concentrations than L-2005 (although the discrepancy between these models at > 2 kbar is much smaller than for Mono Craters).

#### 4.3.2 Mixed H<sub>2</sub>O-CO<sub>2</sub>

Differences in the treatment of H<sub>2</sub>O-CO<sub>2</sub> mixing for rhyolitic melts are more subtle than for basaltic compositions (Fig. 9). Unlike for basalts, the differences in isobar positions mostly result from large differences between the pure CO<sub>2</sub> solubility predicted by different models rather than treatment of mixing. Only VolatileCalc-Rhyolite assumes ideal mixing of H<sub>2</sub>O-CO<sub>2</sub>, causing isobars to have a negative gradient at all pressures. L-2005 accounts for non-ideal mixing through the inclusion of a

term for the mole fraction of  $\text{H}_2\text{O}$  in the fluid in their expression for  $\text{CO}_2$  solubility (equation 5). This empirical representation of non-ideality causes isobars to exhibit a prominent peak at low  $\text{H}_2\text{O}$  contents (Fig. 9). MagmaSat and P–2006, which include a fully non-ideal treatment of mixing, show a far less prominent peak than L–2005. The slight up-tick in the P–2006 isobars at very low  $\text{H}_2\text{O}$  contents is much smaller than for basaltic compositions (e.g., Fig. 6).

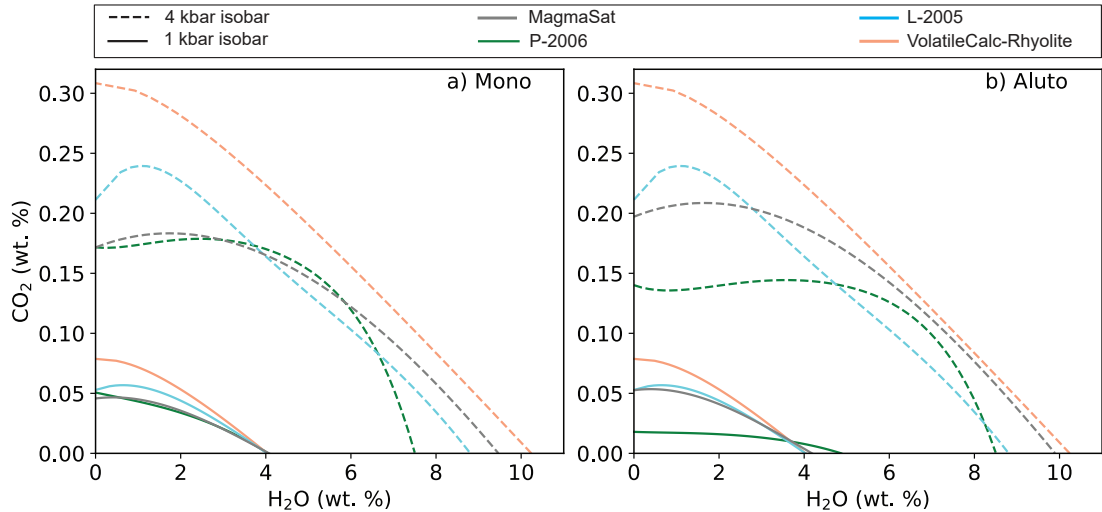


**Figure 9.** 1 and 4 kbar isobars for Mono Craters (a) and the Aluto rhyolite (b) at 800°C.

#### 4.3.3 Pure $\text{CO}_2$

Unlike the relatively good correspondence between rhyolite  $\text{H}_2\text{O}$  models (particularly at low pressures), there is substantial divergence between  $\text{CO}_2$  models at all pressures (Fig. 8c, d). For the Mono Craters rhyolite, VolatileCalc-Rhyolite predicts  $\sim 1.8 \times$  more dissolved  $\text{CO}_2$  than MagmaSat at 2 kbar, while Liu, P–2006 and MagmaSat plot relatively close to each other at  $< 5$  kbar. As VolatileCalc-Rhyolite and L–2005 have no compositional dependence, the model lines are identical for Mono Craters and Aluto. MagmaSat predicts that the Aluto composition has slightly higher  $\text{CO}_2$  solubility at a given pressure compared to the Mono Lake composition (factor of  $\sim 1.2 \times$ ), so the discrepancy between MagmaSat, VolatileCalc-Rhyolite and L–2005 is smaller for Aluto than Mono Craters.

The P–2006 model shows a substantially different trajectory for  $\text{CO}_2$  vs. pressure compared to the other three solubility models for both rhyolite compositions, showing a strongly concave-up shape compared to the near linear trajectory of L–2005 and VolatileCalc-Rhyolite, and the slightly concave-up shape of MagmaSat (Fig. 8c-d). For Mono Craters, P–2006 predicts similar  $\text{CO}_2$  solubility to MagmaSat at  $< 4$  kbar, but rapidly rises to higher  $\text{CO}_2$  contents at higher pressures, predicting al-

most as much dissolved CO<sub>2</sub> as VolatileCalc-Rhyolite at  $\sim$ 12 kbar (Fig. 8c). For Aluto, the curvature of the P–2006 model is even more prominent, predicting drastically lower CO<sub>2</sub> contents than all other models at <6 kbar, and then rapidly rising, predicting higher CO<sub>2</sub> solubility than even VolatileCalc-Rhyolite at >9 kbar (Fig. 8d). These large deviations between models, as well as the large errors on the interaction terms for CO<sub>2</sub> solubility in MagmaSat (Table 3) demonstrate that while H<sub>2</sub>O solubility in rhyolites is well constrained, more work is required to determine the effect of melt composition on CO<sub>2</sub> solubility at a range of pressures and temperatures.

#### 4.4 Comparisons between Basalts and Rhyolites

In this section, we briefly discuss the differences in solubility between basalts (using the MORB1 composition) and rhyolites (using the Mono Craters composition). To differentiate the effect of melt composition from temperature (because basaltic melts tend to be hotter), we perform calculations at 800 and 1000°C for Mono Craters, and 1000°C and 1200°C for MORB1.

When all solubility models are compared (4 applicable to rhyolites, 6 to basalts), there is substantial overlap between curves calculated for MORB1 at 1200°C and Mono Craters at 800°C (compare Fig. 11a vs. Fig. 8a). To get around this problem of large differences between models, we compare the predictions from the three models which can be applied to both Rhyolites and Basalts: MagmaSat (Fig. 10a-b), P–2006 (Fig. 10c-d) and VolatileCalc-Basalt and -Rhyolite (Fig. 10e-f).

MagmaSat and VolatileCalc (Rhyolite vs. Basalt) predict that Mono Craters dissolves more H<sub>2</sub>O than MORB1, even if these melts are at the same temperature (1000°C). In MagmaSat, the difference in solubility between Basalt and Rhyolite is enhanced by the fact that basalts tend to be hotter (the curves get closer when compositions are compared at 1000°C). In contrast, P–2006 predicts that Mono craters at 800°C dissolves less H<sub>2</sub>O than MORB1 at 1200°C, although their solubilities are nearly identical when compared at 1000°C.

MagmaSat and P–2006 predict that MORB1 dissolves more CO<sub>2</sub> than Mono Craters, with the difference increasing rapidly as a function of pressure. In contrast, VolatileCalc predicts that, at 800°C, Mono Craters dissolves more CO<sub>2</sub> than MORB1 at 1000°C or 1200°C, while the model predicts very similar CO<sub>2</sub> solubility when Mono Craters and MORB1 are both at 1000°C.

Overall, these comparisons demonstrate that at <5 kbar, the difference in solubility between basalts and rhyolites is relatively subtle and easily overwhelmed by differences in predictions from different solubility models, particularly given some models predict that solubility increases with temperature, and others predict the opposite (see section 5.3).

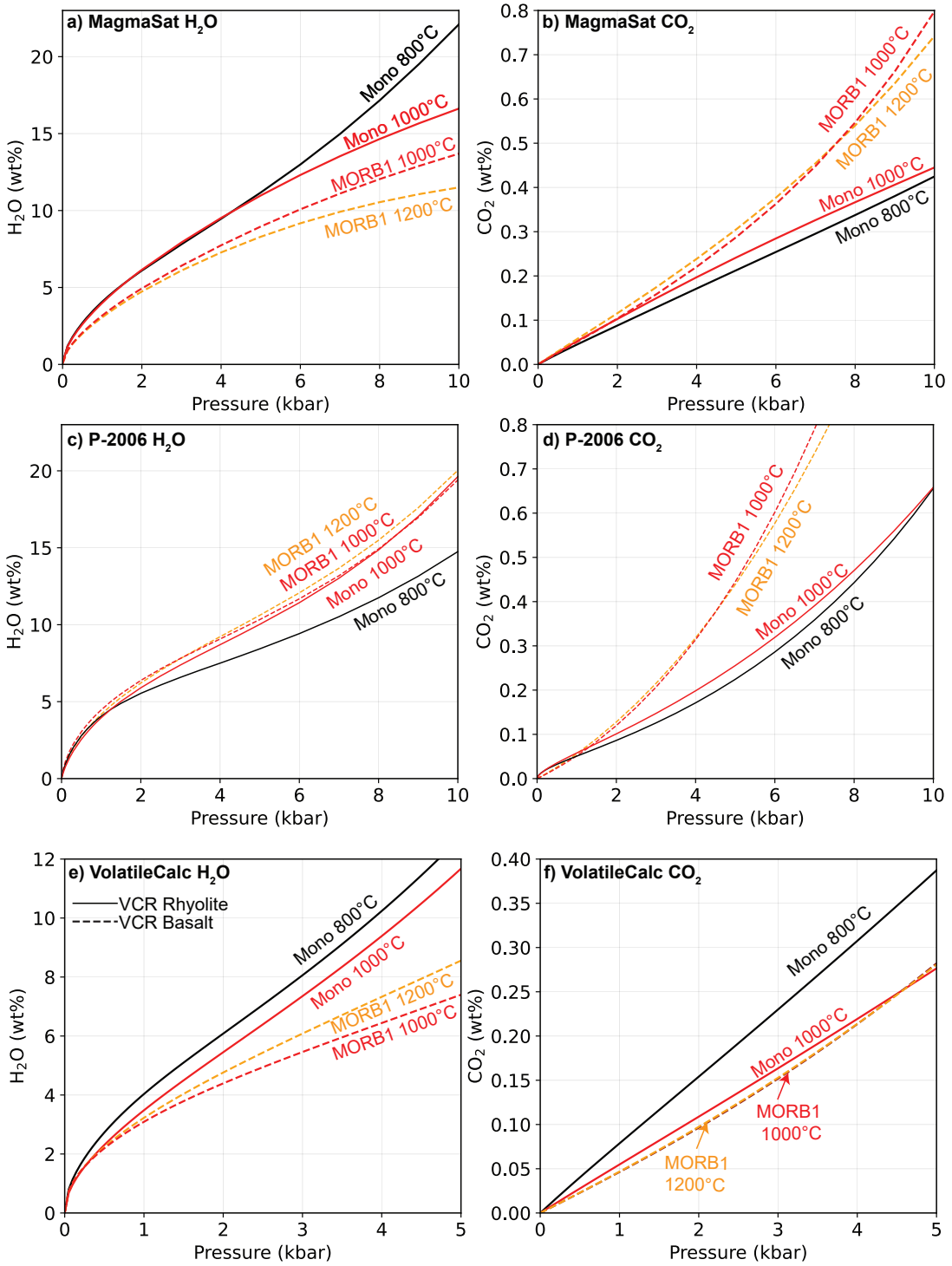


**Figure 10.** Comparison of solubility of basalt (represented by MORB1) to rhyolite (represented by Mono Craters) using MagmaSat (a-b), P-2006 (c-d) and VolatileCalc-Basalt and Rhyolite (d-e). Solubility curves are calculated for 1200°C and 1000°C for basalt, and 1000°C and 800°C for rhyolite.

834     **5 Model Sensitivities**

835     In this section, we explore the sensitivity of the different models to parameters such as temper-  
 836     ature and variable proportions of H<sub>2</sub>O and CO<sub>2</sub>. Specifically, we consider how these inputs affect cal-  
 837     culations of the pressure at which a melt inclusion was trapped (termed the saturation pressure). To  
 838     calculate saturation pressures, the initial concentration of major and volatile elements as well as the  
 839     temperature must be estimated at the time of melt inclusion entrapment. However, a number of pro-  
 840     cesses, such as crystallization of the host mineral on the wall of the inclusion (termed post-entrapment  
 841     crystallization, or PEC), growth of a vapour bubble or daughter phases within the inclusion, and dif-  
 842     fusive re-equilibration with a changing carrier liquid composition can make it difficult to reconstruct  
 843     initial major element and volatile contents (Lowenstern, 1995). Similarly, diffusive re-equilibration  
 844     of the major elements in the melt inclusion and host mineral, as well as the errors associated with  
 845     mineral-melt and melt-only thermometers, can lead to uncertainties in the entrapment temperature,  
 846     which propagates into the saturation pressure. By investigating the effect of varying these parameters  
 847     within realistic limits, insight can be gained into the uncertainties associated with estimating magma  
 848     storage depths using melt inclusions.

849     **5.1 Relationship between saturation pressure and dissolved H<sub>2</sub>O content**

850     Melt inclusion H<sub>2</sub>O contents are vulnerable to diffusional re-equilibration with the melt sur-  
 851     rounding the crystal (here termed the carrier melt), because of the fast diffusion rate of H<sup>+</sup> through  
 852     silicate minerals (Portnyagin et al., 2008). H<sup>+</sup> diffusion is particularly fast in olivine (Gaetani et  
 853     al., 2012), with melt inclusions losing significant amounts of water in hours to days (Bucholz et al.,  
 854     2013). Thus, this discussion focuses on mafic compositions, where olivine-hosted melt inclusions are  
 855     frequently analysed.

856     In relatively H<sub>2</sub>O-poor mafic systems such as MORs and ocean islands (e.g., Hawai'i), diffusive  
 857     re-equilibration can increase melt inclusion H<sub>2</sub>O contents if crystals are mixed into more H<sub>2</sub>O-rich  
 858     carrier melts (Hartley et al., 2015), or, more commonly, cause melt inclusion H<sub>2</sub>O contents to drop if  
 859     the crystal is in contact with a carrier melt that has degassed its H<sub>2</sub>O upon eruption (Gaetani et al.,  
 860     2012; Bucholz et al., 2013). To assess how uncertainty in initial H<sub>2</sub>O contents translates into errors  
 861     on saturation pressures, we calculate saturation pressures for the MORB1 melt composition with 200,  
 862     1000, and 3000 ppm CO<sub>2</sub> (representing melt inclusions trapped at low, medium and high pressures)  
 863     for H<sub>2</sub>O contents between 0–1.5 wt% (Fig. 11a-c). CO<sub>2</sub> contents are held constant while H<sub>2</sub>O con-  
 864     tents are varied, simulating the changes undergone by melt inclusions during diffusive re-equilibration  
 865     (which strongly affects H<sub>2</sub>O contents in the inclusion, but does not change the total CO<sub>2</sub> budget of the  
 866     inclusion).

The relationship between saturation pressure and dissolved H<sub>2</sub>O predicted by each solubility model is strongly dependent on the amount of CO<sub>2</sub> in the melt, and therefore the pressure. To quantify model sensitivity to H<sub>2</sub>O, saturation pressures calculated at H<sub>2</sub>O=1.5 wt% are divided by the saturation pressure calculated at H<sub>2</sub>O=0 wt%, representing the possible discrepancy between the calculated saturation pressure and the real saturation pressure for melt inclusions which have undergone complete H<sup>+</sup> re-equilibration with a fully degassed erupted melt at 0 bar. At low pressures (200 ppm CO<sub>2</sub>), all models show a decrease in calculated saturation pressure with decreasing H<sub>2</sub>O contents, with entrapment pressures being 1.2–1.8× higher before complete H<sub>2</sub>O-loss (Fig. 11a). MagmaSat shows the strongest sensitivity to H<sub>2</sub>O content, and both IM–2012 models the weakest.

At moderate pressures (1000 ppm CO<sub>2</sub>), loss of H<sub>2</sub>O causes a significantly smaller decrease in saturation pressure for VolatileCalc-Basalt, P–2006 and S–2014 compared to the 200 ppm CO<sub>2</sub> scenario (Fig. 11b, 1.1–1.2×). Saturation pressures for 1000 ppm CO<sub>2</sub> calculated using MagmaSat and IM–2012–H first decrease, then increase with H<sub>2</sub>O loss. This is because these models predict that the maximum CO<sub>2</sub> solubility occurs at H<sub>2</sub>O contents at ~0.5–1.25 wt% (see Fig. 6).

At higher pressures (3000 ppm CO<sub>2</sub>), saturation pressures from VolatileCalc-Basalt, P–2006 and S–2014 only drop by ~5–10% with progressive H<sub>2</sub>O-loss, while saturation pressures continually increase with progressive H<sub>2</sub>O-loss for IM–2012–H and -A and MagmaSat (because these models predict that maximum CO<sub>2</sub> solubility is found at H<sub>2</sub>O contents >1.5 wt% at these pressures; Fig. 6).

Within a given suite of MORB or OIB melt inclusions, the range of measured H<sub>2</sub>O contents, and the uncertainty involved in reconstructing initial H<sub>2</sub>O contents following diffusional re-equilibration, is likely significantly smaller than the 1.5 wt% H<sub>2</sub>O considered here (Koleszar et al., 2009; Sides et al., 2014a; Wieser et al., 2021). Thus, except at low pressures (<1 kbar), uncertainties in saturation pressures due to diffusive re-equilibration of H<sub>2</sub>O in relatively anhydrous systems are likely comparable to the analytical errors associated with the measurements of volatile species by FTIR or SIMS ( $\pm 5\text{--}10\%$ ), errors on each solubility model (~10–20%), and significantly smaller than the differences between solubility models.

The higher H<sub>2</sub>O contents of melt inclusions from subduction zones (~2–6 wt%; Plank et al., 2013) mean that substantially more H<sub>2</sub>O can be lost following diffusive re-equilibration with a degassed carrier melt upon eruption. Additionally, arc melt inclusions are vulnerable to diffusive re-equilibration during crustal storage. This is because these relatively hydrous magmas saturate in a H<sub>2</sub>O-rich fluid at high pressures in the crust. Thus, as a melt and its crystal cargo ascends from a deeper storage reservoir to a shallower storage reservoir, significant quantities of H<sub>2</sub>O will be degassed and the H<sub>2</sub>O contents of melt inclusions will rapidly diffusively re-equilibrate with the new carrier melt

composition (Gaetani et al., 2012). Even if samples are rapidly quenched upon eruption (preventing syn-eruptive H<sub>2</sub>O diffusion), only the volatile contents of melt inclusions trapped in the shallowest storage reservoir can be reliably converted into saturation pressures (Gaetani et al., 2012). This contrasts with more H<sub>2</sub>O-poor systems such as mid-oceanic ridges and oceanic islands, where H<sub>2</sub>O only degasses in the upper few hundred metres of the crust, so ascent to a shallower reservoir is not accompanied by a drop in melt H<sub>2</sub>O contents (although diffusive re-equilibration could occur if the resident melts in the shallower reservoir have different H<sub>2</sub>O contents; Hartley et al., 2015).

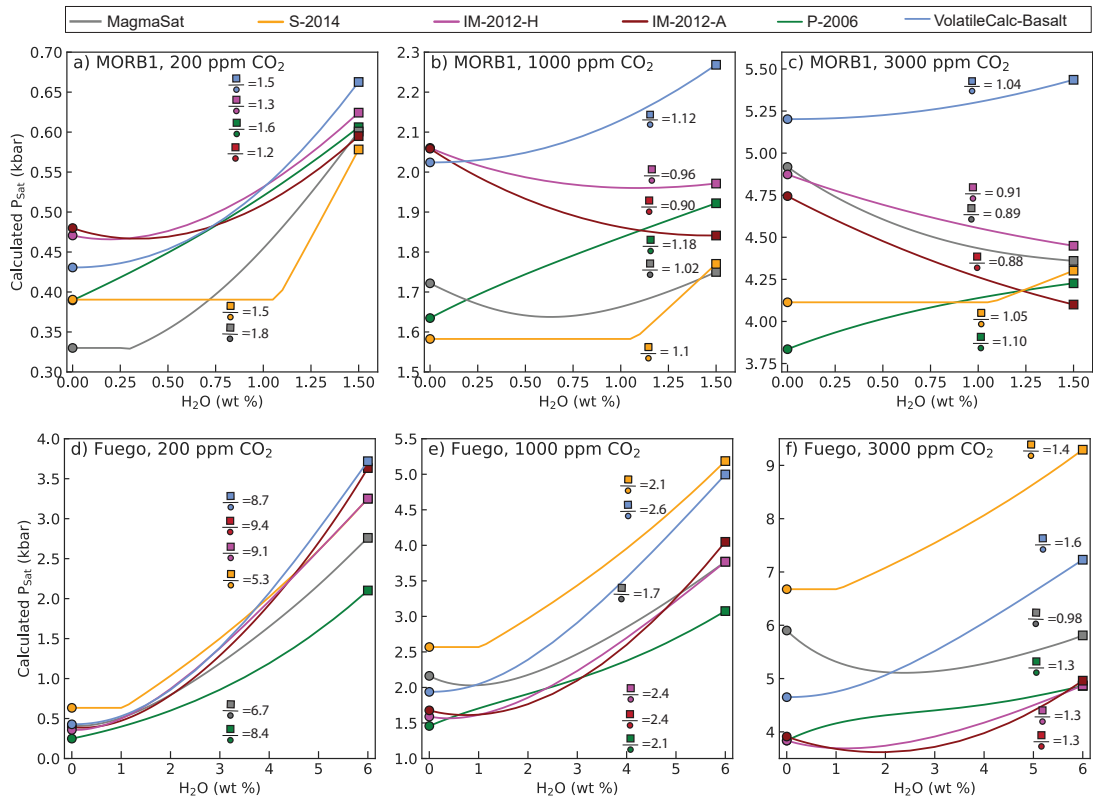


**Figure 11.** a-c) Relationship between saturation pressure and melt H<sub>2</sub>O content for H<sub>2</sub>O-poor melts (using the MORB1 composition at 1200°C). Three different melt CO<sub>2</sub> contents (200, 1000, 3000 ppm) are shown in part a, b and c respectively. The numbers on the graphs show the saturation pressure at 1.5 wt% H<sub>2</sub>O (square symbol) divided by the saturation pressure at 0 wt% H<sub>2</sub>O for each model. d-f) Sensitivity tests using the composition of a Fuego melt inclusion (Table 1) at 1000°C, and H<sub>2</sub>O contents between 0–6 wt%. Note that the y scale for parts a-c is significantly smaller than parts d-f.

To investigate the effect of H<sub>2</sub>O re-equilibration on melt inclusion saturation pressures in arcs, we repeat the sensitivity test described above, using the major element composition of a Fuego melt

inclusion with 49.7 wt% SiO<sub>2</sub> from Lloyd et al. (2013, Table 1) and H<sub>2</sub>O contents between 0–6 wt% (Fig. 11d-f). For melt inclusions with 200 ppm CO<sub>2</sub>, complete diffusive loss of H<sub>2</sub>O may result in saturation pressures being underestimated by a factor of  $\sim 5\text{--}10\times$ . Even for melts with 3000 ppm CO<sub>2</sub> (the highest pressure regime examined, and thus the best case scenario), diffusive loss can affect saturation pressures by factors of 0.98–1.6 $\times$  (similar in magnitude to the sensitivity displayed by H<sub>2</sub>O-poor melts at the lowest pressures; Fig. 11a vs. f). Only saturation pressures calculated in MagmaSat for the most CO<sub>2</sub>-rich melts display variations with variable H<sub>2</sub>O-loss similar in magnitude to analytical errors. Thus, it is extremely important to determine whether melt inclusions have undergone H<sub>2</sub>O-loss during ascent to a shallower reservoir or syn-eruptive degassing before using saturation pressures to deduce magma storage depths in H<sub>2</sub>O-rich volcanic systems.

## 5.2 Relationship between saturation pressure and dissolved CO<sub>2</sub> content

Estimating the initial CO<sub>2</sub> contents of melt inclusions is also challenging. While the total CO<sub>2</sub> content of the inclusion is not affected by diffusive re-equilibration, CO<sub>2</sub> may be partitioned from the melt phase into a vapour bubble. Cooling following melt inclusion entrapment is accompanied by the formation of a denser mineral phase from a less dense silicate melt, and differential thermal contraction of the melt and crystal. These processes cause the internal pressure of the inclusion to drop (Steele-Macinnis et al., 2011; Maclennan, 2017), driving the nucleation and growth of a vapour bubble. This may be enhanced by the diffusive loss of H<sub>2</sub>O, which also causes a pressure drop in the melt inclusion because of the high molar volume but low molecular weight of H<sub>2</sub>O (Gaetani et al., 2012; Aster et al., 2016). A drop in pressure, combined with a decrease in the solubility of CO<sub>2</sub> in the melt phase because of changes to the major element composition accompanying post-entrapment crystallization, causes CO<sub>2</sub> to partition strongly into the vapour bubble (L. R. Moore et al., 2015; Steele-Macinnis et al., 2011; Maclennan, 2017; Wieser et al., 2021). A number of recent studies have quantified the amount of CO<sub>2</sub> in vapour bubbles using Raman Spectroscopy, and demonstrated that between 15–99% of the total CO<sub>2</sub> budget of the inclusion may be held within the vapour bubble (Hartley et al., 2014; L. R. Moore et al., 2015; Wieser et al., 2021; Allison et al., 2021). This means that a large proportion of literature melt inclusion data, which only measured the CO<sub>2</sub> content of the glass phase, may have significantly underestimated initial CO<sub>2</sub> contents (and therefore saturation pressures).

In relatively H<sub>2</sub>O-poor systems such as Hawai'i and Iceland, where melt inclusion CO<sub>2</sub> contents have the dominant control on saturation pressures (shown by the near horizontal slopes of most model isobars at low H<sub>2</sub>O contents; Fig. 6), it is readily apparent that saturation pressures will be significantly underestimated if a CO<sub>2</sub>-rich vapour bubble is not measured. In arcs, H<sub>2</sub>O contents inferred from melt inclusions or mineral hygrometers are sometimes used to place first order constraints on

saturation pressures (e.g. Plank et al., 2013; Blundy & Cashman, 2005; Goltz et al., 2020). However, even in very H<sub>2</sub>O-rich melts, the non-vertical orientation of isobars at high H<sub>2</sub>O contents indicates that CO<sub>2</sub> contents still have an important role in determining the saturation pressure (Fig. 6). Additionally, only a very small number of studies have measured CO<sub>2</sub> in melt inclusion vapour bubbles from arc systems (L. R. Moore et al., 2015; Aster et al., 2016; Venugopal et al., 2020; Mironov et al., 2020). Thus, it is vital to determine the effect of CO<sub>2</sub> on saturation pressures in H<sub>2</sub>O-rich systems.

Using a similar method to that for H<sub>2</sub>O discussed above, we calculate saturation pressures for the composition of a Fuego melt inclusion from Lloyd et al. (2013) with varying CO<sub>2</sub> and H<sub>2</sub>O contents. The mean melt inclusion glass CO<sub>2</sub> content from this melt inclusion suite was 340 ppm (range of 59–786 ppm). However, Raman analyses of vapour bubbles in the same sample set by L. R. Moore et al. (2015) reveals that 993–4776 ppm of CO<sub>2</sub> has migrated from the glass phase into the vapour bubble following melt inclusion entrapment. Thus, we calculate saturation pressures for CO<sub>2</sub> contents between 0–5000 ppm at 1000°C for 2, 4 and 6 wt% H<sub>2</sub>O respectively (after Plank et al., 2013).

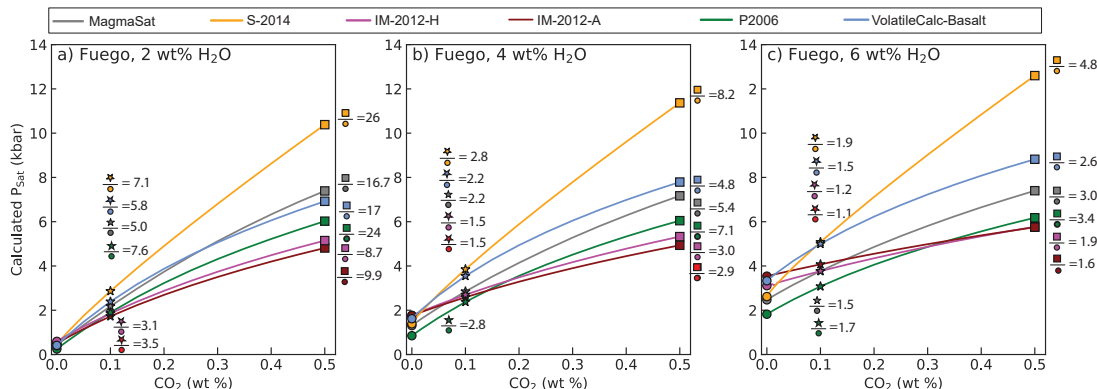


**Figure 12.** Relationship between saturation pressures and melt CO<sub>2</sub> contents for H<sub>2</sub>O-rich melts (using the composition of a Fuego melt inclusion at 1000°C; Table 1). Three different melt H<sub>2</sub>O contents (2, 4 and 6 wt%) are shown in part a, b and c) respectively. The numbers on the graphs show the saturation pressure at 5000 ppm CO<sub>2</sub> (square symbol) divided by the saturation pressure at 0 ppm CO<sub>2</sub> (circle), and the saturation pressure at 1000 ppm (star symbol) divided by the saturation pressure at 0 ppm CO<sub>2</sub> (square) for each model.

S-2014 is most sensitive to CO<sub>2</sub> content, and IM-2012-H and -A the least sensitive. With increasing H<sub>2</sub>O, the change in saturation pressure with increasing CO<sub>2</sub> becomes smaller, but is still significant (Fig. 12). For example, calculating a H<sub>2</sub>O-only saturation pressure for a melt inclusion with H<sub>2</sub>O=6 wt% in MagmaSat would underestimate magma storage depths by a factor of 1.5 if the melt inclusion had 1000 ppm CO<sub>2</sub>, and a factor of 3 if the inclusion had 5000 ppm CO<sub>2</sub>. For a melt inclu-

960 sion with 4 wt% H<sub>2</sub>O, H<sub>2</sub>O-only saturation pressures underestimate by a factor of  $\sim$ 2.2 for 1000 ppm  
961 CO<sub>2</sub>, and 5.4 for 5000 pm CO<sub>2</sub>. These variations in saturation pressure overwhelm the other errors  
962 associated with melt inclusion barometry (e.g., uncertainty in crustal density profiles, analytical errors  
963 associated with volatile measurements by FTIR or SIMS, differences between solubility models). Fur-  
964 ther investigation of the prevalence of CO<sub>2</sub>-rich vapour bubbles in arc lavas is clearly required to have  
965 confidence in published barometric estimates in studies which did not measure the vapour bubbles, or  
966 used mineral hygrometers.

967 Saturation pressures in rhyolitic magmas are also very sensitive to melt CO<sub>2</sub> contents (Fig. 13).  
968 For example, saturation pressures calculated for 1000 ppm CO<sub>2</sub> vs. 0 ppm CO<sub>2</sub> differ by factors of  
969 5.7–8.8 $\times$  for 2 wt% H<sub>2</sub>O, and 1.6–2 $\times$  for 6 wt% H<sub>2</sub>O. Even saturation pressures calculated for 300  
970 ppm CO<sub>2</sub> (0.03 wt%) vs 0 ppm CO<sub>2</sub> are a factor of  $\sim$ 2–3 $\times$  higher for 2 wt% H<sub>2</sub>O, and 1.2–1.3 $\times$   
971 higher for 6 wt% H<sub>2</sub>O. The strong effect of CO<sub>2</sub> on saturation pressure is important to recognise when  
972 calculating saturation pressures using only melt H<sub>2</sub>O contents, such as studies using mineral-melt  
973 hygrometers (Waters & Lange, 2013), or volatiles-by-difference methods to estimate H<sub>2</sub>O contents  
974 of melt inclusions. It is also interesting to note that, to our knowledge, there are no published Ra-  
975 man measurements of CO<sub>2</sub> in vapour bubbles which grew after melt inclusion entrapment in dacitic-  
976 rhyolitic melt compositions. While the extremely low CO<sub>2</sub> contents of many rhyolitic melt inclusions  
977 are commonly interpreted to result from shallow crustal storage, it is becoming increasingly recog-  
978 nised that mafic melt inclusions with CO<sub>2</sub> below detection limit contain large quantities of CO<sub>2</sub> in  
979 the vapour bubble (Wieser et al., 2021). Thus, examination of vapour bubbles in melt inclusions from  
980 more silicic systems (e.g., Fig. 1 of Lowenstern, 2001) is likely warranted, to rule out the possibility  
981 that these melts crystallized at greater depths than calculated using measurements of CO<sub>2</sub> hosted in  
982 just the glass phase.

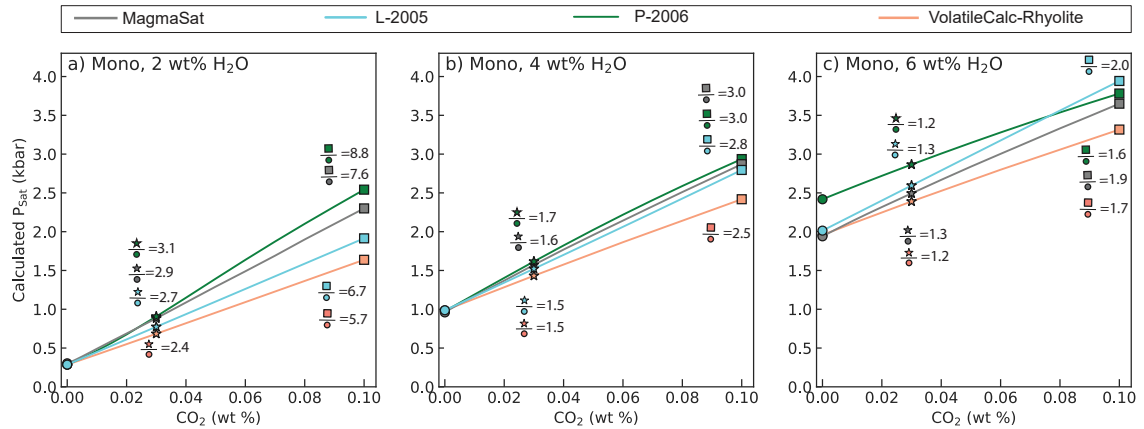


**Figure 13.** Sensitivity of saturation pressures to melt  $\text{CO}_2$  contents at three different  $\text{H}_2\text{O}$  contents (2, 4 and 6 wt%) for the Mono Craters rhyolite. Ratios of saturation pressures at 0.03 wt%  $\text{CO}_2$  (300 ppm; star symbol) vs. 0 wt% (circle), and 0.1 wt% (1000 ppm; square symbol) vs. 0 wt%  $\text{CO}_2$  are shown on the figure.

### 5.3 Sensitivity to Temperature

The temperature of the melt at the time of entrapment is another source of uncertainty when calculating saturation pressures, as melt or mineral-melt thermometers are relatively imprecise. For example, the liquid  $\text{MgO}$  thermometer presented in eq. 13 of Putirka (2008) has a standard error of  $\pm 71^\circ\text{C}$ , while the clinopyroxene–liquid thermometer presented in their equation 28b has a standard error of  $\pm 48^\circ\text{C}$ . Changes in the major element compositions of the melt inclusion during PEC and diffusive  $\text{H}_2\text{O}$ -loss can also introduce errors when estimating entrapment temperatures (as most thermometers are highly sensitive to the  $\text{MgO}$  and  $\text{H}_2\text{O}$  content of the melt). Additionally, almost all solubility experiments are performed at supra-liquidus conditions, while melt inclusion formation must take place at sub-liquidus conditions, so extrapolation to lower temperatures is an unfortunate necessity.

To investigate the sensitivity of different models to temperature, we calculate the 0.5 and 2 kbar isobars for the MORB1 composition at  $1000^\circ\text{C}$  and  $1400^\circ\text{C}$ . Only S-2014 shows no temperature dependency, because there is neither a temperature or fugacity term in their equations. Interestingly, there is considerable disagreement between the other models as to whether a hotter magma dissolves more or less volatiles. MagmaSat and P-2006 predict an increase in pure  $\text{CO}_2$  solubility with increasing temperature, while VolatileCalc-Basalt and IM-2012-A and -H predict a much smaller decrease (Fig. 14a-c). In all models but IM-2012-A, isobars calculated for lower temperatures intercept the x axis ( $\text{CO}_2=0$  wt%) at higher  $\text{H}_2\text{O}$  contents, so the temperature dependency of  $\text{H}_2\text{O}$  solubility is

1002 opposite to that for CO<sub>2</sub> solubility. To visualize the effect of these trends on calculated saturation  
 1003 pressures for the MORB1 composition, the calculated saturation pressures for melts with volatile con-  
 1004 tents represented by the yellow and cyan stars on Figure 14b are plotted against temperature (between  
 1005 1000–1400°C; Fig. 14c-d). MagmaSat and P–2006 show the strongest temperature sensitivity, with a  
 1006 slope opposite to that of the more subtle changes predicted by VolatileCalc-Basalt and IM–2012.

1007 The lack of consensus as to whether increasing temperature increases or decreases the solubility  
 1008 of H<sub>2</sub>O and CO<sub>2</sub> indicates that this effect is relatively subtle, and overwhelmed by analytical errors  
 1009 associated with measuring experimental products (and other sources of experimental scatter; e.g., Fig.  
 1010 16a-b). This makes it very difficult for empirical models to fully constrain the temperature sensitiv-  
 1011 ity, particularly given that the experiments conducted by any given study are usually performed at a  
 1012 single temperature. For example, all the experiments used to calibrate the VolatileCalc-Basalt model  
 1013 were conducted at 1200°C, so the temperature dependency of this model results from the fugacity  
 1014 function, and 1/T terms from Dixon et al. (1995), rather than experimental observations.

1015 IM–2012 is calibrated on experiments mostly performed at 1200–1300°C (with a few spanning  
 1016 1100–1400°C). Their empirical expressions contain  $C_{H_2O} \times \frac{P}{T}$  and  $C_{CO_2} \times \frac{P}{T}$  terms in their expressions  
 1017 for H<sub>2</sub>O and CO<sub>2</sub> solubility respectively (equation 11 and 15), where C<sub>H<sub>2</sub>O</sub> and C<sub>CO<sub>2</sub></sub> are empirically-  
 1018 derived constants, and P and T are pressure and temperature. In the hydrous model, C<sub>H<sub>2</sub>O</sub> is negative  
 1019 ( $-0.02 \pm 0.02$ ), so H<sub>2</sub>O solubility increases with increasing temperature, while in the anhydrous model  
 1020 C<sub>H<sub>2</sub>O</sub> is positive ( $0.02 \pm 0.02$ ), so H<sub>2</sub>O solubility decreases with increasing temperature (Fig. 14). As  
 1021 the magnitude of these coefficients is small, the temperature effect on H<sub>2</sub>O solubility is small, and  
 1022 only visible at higher pressures (because of the P part of these terms; Fig. 14a vs. c). It is also worth  
 1023 noting that these coefficients in both models are within error of zero, showing that the experimental  
 1024 dataset used to calibrate this model showed very little evidence for a change in H<sub>2</sub>O solubility with  
 1025 temperature. In both the hydrous and anhydrous models, C<sub>CO<sub>2</sub></sub> is positive ( $0.12 \pm 0.02$  and  $0.14 \pm 0.02$   
 1026 respectively) and larger in magnitude than C<sub>H<sub>2</sub>O</sub>, so CO<sub>2</sub> solubility decreases with increasing tempera-  
 1027 ture (see Fig. 14c).

1028 The approach taken by S–2014 and A–2019 is an interesting alternative when constructing sol-  
 1029 ubility models. While S–2014 is calibrated on experiments conducted between 1200–1300°C for CO<sub>2</sub>,  
 1030 and 1200–1250°C for H<sub>2</sub>O, their solubility equations contain no temperature or fugacity term. Instead,  
 1031 these authors suggest that the H<sub>2</sub>O model should ideally be used between 1150–1250°C. They perform  
 1032 additional tests on experiments between 1050–1400°C not used in the calibration, and show that their  
 1033 model predicts H<sub>2</sub>O solubility within  $\pm 10\%$  for 78% of experiments for this wider temperature range.  
 1034 The S–2014 testing dataset for CO<sub>2</sub> only has a slightly different temperature range than the calibra-

1035 tion dataset (1170–1250°C vs. 1200–1250°C), so they do not suggest an expanded temperature range  
1036 for CO<sub>2</sub>. Similarly, the spreadsheet for A–2019 (and the implementation of this model in VESIcal)  
1037 performs all calculations at 1200°C, regardless of the user-input temperature. Allison et al. (2019)  
1038 suggest that this approach is likely valid between 1000–1400°C.

1039 Unlike empirical models, the temperature sensitivity of P–2006 and MagmaSat arises from the  
1040 entropy differences between melt and fluid components. Given the limited experimental evidence for  
1041 changes in solubility with temperature, the directionality inferred by thermodynamical models is more  
1042 likely to be correct, as the relative entropy differences between components are easier to constrain than  
1043 deconvoluting subtle differences between the solubility of CO<sub>2</sub> and H<sub>2</sub>O in experiments run at different  
1044 temperatures, and because all empirical models are being extrapolated to lower temperatures than the  
1045 supra-liquidus experiments used to calibrate them. However, the fact that P–2006 doesn't account for  
1046 volatile speciation for either H<sub>2</sub>O or CO<sub>2</sub>, and MagmaSat doesn't account for the two H<sub>2</sub>O species in  
1047 the melt means that these thermodynamic temperature sensitivities may also need further interrogation.

1048 Overall, although the differences between models is interesting, and important to recognise when  
1049 extrapolating beyond the range of the calibration dataset, the uncertainty that temperature variations  
1050 introduce to saturation pressure calculations are relatively small for mafic melts. For example, an un-  
1051 certainty in the initial entrapment temperature of ±100°C introduces an uncertainty similar to that  
1052 associated with in-situ measurements of melt inclusion volatile contents (±5–10%; Fig. 14).

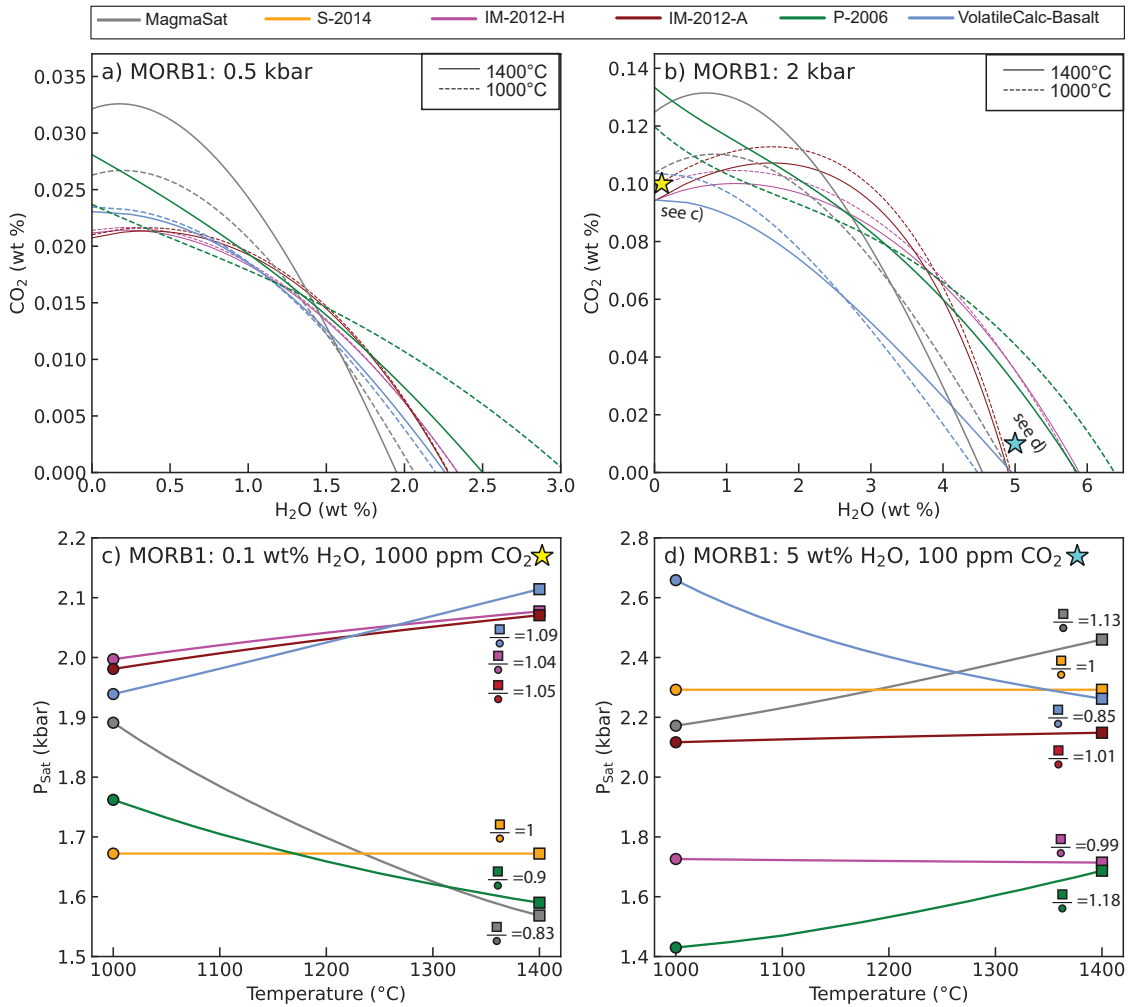


**Figure 14.** Evaluating model sensitivity to temperature (using the MORB1 composition). a-b) Isobars evaluated at 1000 and 1400°C and 0.5 and 2 kbar. c) Relationship between saturation pressure and temperature for a melt with 1000 ppm CO<sub>2</sub>, 0.1 wt% H<sub>2</sub>O (yellow star on a), d) 100 ppm CO<sub>2</sub>, 5 wt% H<sub>2</sub>O (cyan star on b). Ratios of saturation pressures at 1400°C (square symbol) to 1000°C (circle symbol) are shown on the figure.

Similarly, temperature sensitivity in rhyolitic melts was evaluated by calculating isobars at 0.5 and 2 kbar for 700 and 900°C using the Mono Craters rhyolite composition. As for the basaltic example, the directionality and magnitude of effect of temperature on saturation pressures for melts with volatile contents indicated by the colored stars is shown in Fig. 15c-d for temperatures between 700 and 1000°C. VolatileCalc-Rhyolite shows the strongest temperature sensitivity, predicting that the solubility of CO<sub>2</sub> decreases with increasing temperature. L-2005 also predicts decreasing CO<sub>2</sub> solubility with increasing temperature, although this effect is smaller than in VolatileCalc-Rhyolite. Decreasing solubility of molecular CO<sub>2</sub> with increasing temperature was demonstrated experimentally by Fogel

and Rutherford (1990). In contrast, the two thermodynamic models, P-2006 and MagmaSat, predict that pure CO<sub>2</sub> solubility increases with increasing temperature. VolatileCalc-Rhyolite also predicts that H<sub>2</sub>O solubility decreases with increasing temperature, but the effect is smaller than for CO<sub>2</sub>.

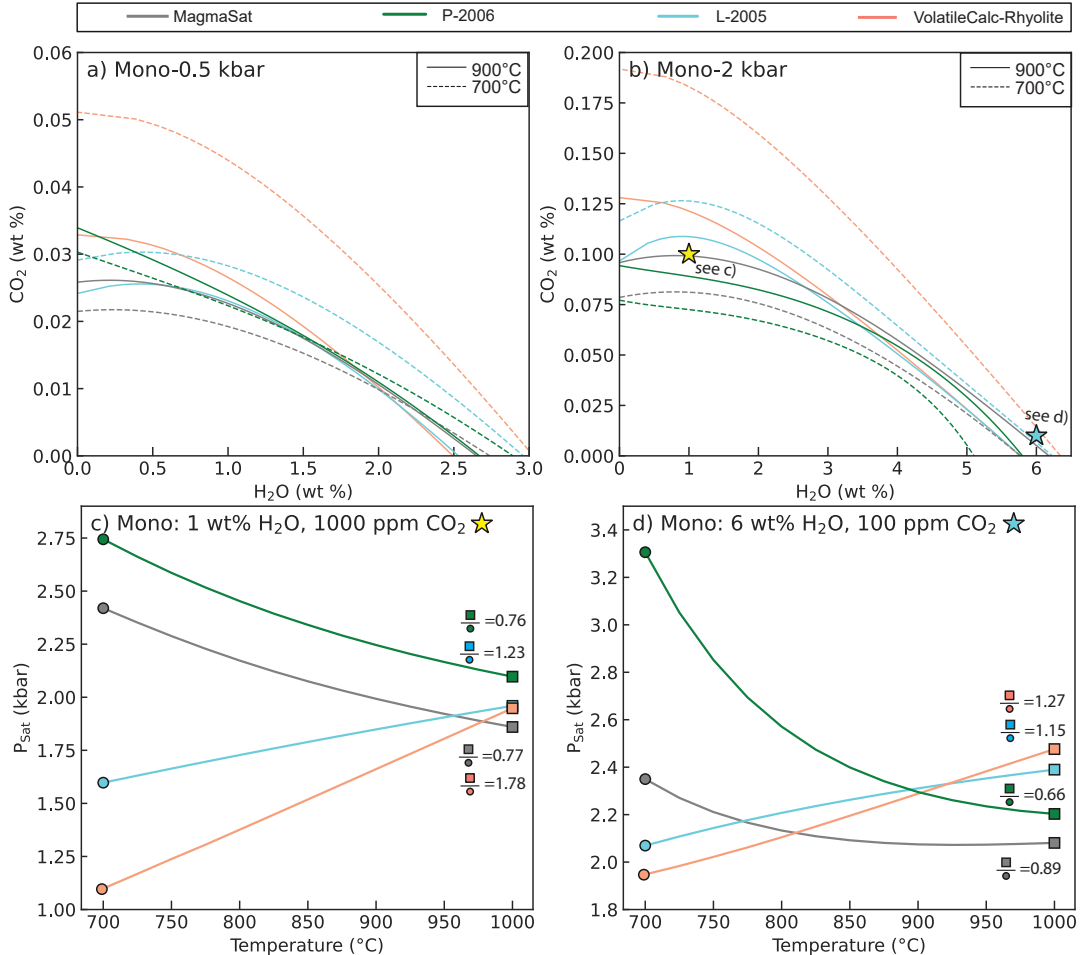


**Figure 15.** Sensitivity of saturation pressures for the Mono Craters rhyolite to temperature. a-b) Isobars calculated for different solubility models at 700 and 900°C and 0.5 and 2 kbar. c) Relationship between saturation pressure and temperature for a melt with 1000 ppm CO<sub>2</sub>, 1 wt% H<sub>2</sub>O (yellow star in b), d) 100 ppm CO<sub>2</sub>, 6 wt% H<sub>2</sub>O (cyan star in b). Ratios of saturation pressures at 900°C (square symbol) to 700°C (circle symbol) are shown on the figure.

It is noteworthy that the temperature sensitivity of CO<sub>2</sub> solubility predicted by L-2005 and VolatileCalc-Rhyolite is much greater than that shown by any of the basaltic models (Fig. 14d-e vs. Fig 15d-e), and significant considering other sources of error associated with saturation pressure calculations. MagmaSat and P-2006 also show a far greater sensitivity to H<sub>2</sub>O solubility between

1068 700–850°C in rhyolites than any of the basaltic models between 1000–1400°C (Fig. 14f vs. Fig 15f),  
 1069 although the sensitivity decreases between 800–900°C.

1070 Given the contrasting behaviour of empirical and thermodynamic models, and the relatively  
 1071 strong effect of temperature in rhyolitic melts, we suggest that users proceed with caution when ex-  
 1072 trapolating empirical models to temperatures significantly lower or higher than the calibration tem-  
 1073 perature of each model. It may be best to use empirical models at the calibration temperature (e.g.,  
 1074 1200°C for VolatileCalc-Basalt, 850°C for VolatileCalc-Rhyolite), which is the approach used by in the  
 1075 models of S–2014 and A–2019, rather than introduce a temperature sensitivity with the wrong sign.  
 1076 This is discussed in further detail for VolatileCalc-Rhyolite in section 6.

## 1077 6 Intermediate Compositions

1078 In this section, we compare the predictions of different solubility models for intermediate melt  
 1079 compositions (andesites to dacites). Lavas with these compositions are dominant within subduction  
 1080 zones, and volcanoes erupting these compositions are extremely hazardous. Yet, there is a notable  
 1081 paucity of solubility experiments for andesitic and dacitic compositions relative to basalts and rhyolites  
 1082 (Fig. 2; King & Holloway, 2002; Botcharnikov et al., 2006). This section builds on the sensitivity tests  
 1083 performed in section 5 to evaluate possible discrepancies between model outputs and experimental  
 1084 constraints.

1085 The calibration dataset of MagmaSat has the broadest coverage of andesitic-dacitic composi-  
 1086 tions of all the models described here (although it is far from extensive). While there are a number  
 1087 of pure H<sub>2</sub>O experiments, MagmaSat only includes one pure CO<sub>2</sub> experiment on an andesitic melt  
 1088 (conducted at 1 GPa; King & Holloway, 2002), and no pure CO<sub>2</sub> experiments on dacitic melts. Sim-  
 1089 ilarly for mixed H<sub>2</sub>O-CO<sub>2</sub>, the calibration dataset for andesitic melts includes only four experiments  
 1090 from King and Holloway (2002), 21 from Botcharnikov et al. (2006) and three from Botcharnikov et  
 1091 al. (2007). Dacitic liquids are represented by the 12 experiments on mixed H<sub>2</sub>O-CO<sub>2</sub> solubility by  
 1092 Behrens et al. (2004). As the P–2006 model had a decade fewer experimental constraints available for  
 1093 calibration, it only includes the one pure CO<sub>2</sub> and four mixed H<sub>2</sub>O-CO<sub>2</sub> andesitic experiments of King  
 1094 and Holloway (2002). The IM–2012 model includes two pure H<sub>2</sub>O experiments that lie within the an-  
 1095 desite field on a TAS diagram, but no H<sub>2</sub>O-CO<sub>2</sub> experiments, and no experiments in the dacitic field.  
 1096 None of the other models contain any andesitic or dacitic melts in their calibration datasets.

### 1097 6.1 Comparing solubility models to experimental products

1098 The suitability of different solubility models for andesitic-dacitic compositions can be evaluated  
 1099 by calculating isobars using the melt compositions, pressures and temperatures of different experimen-

1100 tal studies, and comparing these isobars to measurements of dissolved volatile contents in experimental  
1101 products (similar to the method used in the supplementary material of Ghiorso & Gualda, 2015). The  
1102 2 and 5 kbar andesitic experiments of Botcharnikov et al. (2006) are shown in Fig. 16a-b, the 1, 2,  
1103 and 5 kbar dacitic experiments of Behrens et al. (2004) are shown in Fig. 16c-e, and the 10 kbar an-  
1104 desite experiments of King and Holloway (2002) are shown in Fig. 16f. Additional isobar diagrams  
1105 for the 3–12 kbar basaltic-andesite experiments of Mangan et al. (2021) are shown in the supporting  
1106 information.

1107 Isobar diagrams show that S–2014 significantly underpredicts CO<sub>2</sub> for all experiments except the  
1108 most H<sub>2</sub>O-poor composition of King and Holloway (2002). L–2005, VolatileCalc-Basalt and -Rhyolite  
1109 also mostly plot to lower CO<sub>2</sub> contents than experimental products. IM–2012–H and –A do a reason-  
1110 able job of recreating the most H<sub>2</sub>O-poor experiments at <5 kbar, but curve rapidly down to intercept  
1111 the x axis at lower H<sub>2</sub>O contents than experimental products and other models. MagmaSat is a good  
1112 match to experimental data in Fig. 16d, e and f, but plots to lower CO<sub>2</sub> contents than experiments in  
1113 Fig. 16 a, b and c. Using Fe<sup>3+</sup> proportions best representing the experimental conditions, P–2006 only  
1114 passes through experimental data on Figs. 16a-b, and e, and plots to significantly lower CO<sub>2</sub> contents  
1115 than experiments (lower than MagmaSat) on Fig. 16c and d. P–2006 is a better match to most exper-  
1116 iments if Fe<sup>3+</sup>/Fe<sub>T</sub>=0, but overpredicts CO<sub>2</sub> solubility at 10 kbar for all redox states. Interestingly,  
1117 none of the available models recreate the near-flat trajectory of dissolved CO<sub>2</sub> contents with increasing  
1118 H<sub>2</sub>O from Botcharnikov et al. (2006).

1119 The underprediction of CO<sub>2</sub> solubility by S–2014 is a good example of the dangers of extrap-  
1120 olating models accounting for the effect of melt composition using empirical expressions beyond the  
1121 compositional range of the calibration dataset. The S–2014 model expresses CO<sub>2</sub> solubility as a func-  
1122 tion of the composition parameter, Π\*, with CO<sub>2</sub> solubility increasing as an exponential function of  
1123 Π\* at a given pressure (equation 16). The melt compositions for the three sets of experimental studies  
1124 shown in Fig. 16 all plot to much lower Π\* values than any of the melts in the calibration dataset (or-  
1125 ange diamonds; Fig. 17a). These low Π\* values mean that the S–2014 model predicts that these melts  
1126 have very low CO<sub>2</sub> solubilities. However, CO<sub>2</sub> solubility for melts with Π\* values outside the range of  
1127 the calibration dataset may not follow the same exponential function of this parameter as melt compo-  
1128 sitions within the calibration range. Additionally, the exponential dependency of CO<sub>2</sub> solubility on Π\*  
1129 incorporated by S–2014 likely breaks down in more evolved melts, because Π\* represents the ability of  
1130 the melt to form carbonate-bearing species, while more evolved melts contain increasing proportions  
1131 of molecular CO<sub>2</sub> (Shishkina et al., 2014). For example, the proportion of molecular CO<sub>2</sub> to carbonate

1132 species varies between 0–4 wt% in the experiments of Botcharnikov et al. (2006), and 3–30 wt% in the  
1133 dacitic experiments of Behrens et al. (2004).

1134       VolatileCalc-Basalt and VolatileCalc-Rhyolite underpredict CO<sub>2</sub> solubility for all intermediate  
1135 experiments, with VolatileCalc-Rhyolite predicting lower pure CO<sub>2</sub> solubility than VolatileCalc-Basalt.  
1136 This is noteworthy, because many publications have calculated saturation pressures for andesitic and  
1137 dacitic melts using VolatileCalc-Rhyolite (e.g., Blundy et al., 2006; Atlas et al., 2006; Cassidy et al.,  
1138 2015; Koleszar et al., 2012). In the original publication, Newman and Lowenstern (2002) state: “be-  
1139 cause many andesites contain rhyolitic interstitial melt, VolatileCalc may also be applicable to these  
1140 intermediate compositions.” However, this should not be taken to suggest that VolatileCalc-Rhyolite  
1141 is safely extrapolated to andesitic-dacitic melts. Instead, this statement is referring to the fact that  
1142 many lavas with andesitic bulk compositions have rhyolitic groundmass/melt inclusion compositions  
1143 (e.g., Tamura & Tatsumi, 2002; Reubi & Blundy, 2009), where VolatileCalc-Rhyolite may be applica-  
1144 ble. Interestingly, VolatileCalc-Rhyolite isobars calculated for the reference temperature of this model  
1145 (850°C) rather than the experimental temperature are a good match to experimental data at < 5 kbar  
1146 (see Supplementary Fig. S3). Thus, the main failure of this model in intermediate compositions ap-  
1147 pears to result from the fact that this model is extremely sensitive to temperature, and these melts  
1148 have much higher temperatures than the experiments used to calibrate this model. This supports our  
1149 suggestion in section 4.2.1 that it may be better run models at their reference temperature, rather  
1150 than extrapolate beyond the calibration range.

1151       It is also worth noting that all these experimental products have negative values of the Dixon Π  
1152 parameter (equation 2). As highlighted by G. Moore (2008), the full Π expression of Dixon (1997) can-  
1153 not be used to calculate CO<sub>2</sub> solubility in calc-alkaline lavas, because Π is negative (yielding a negative  
1154 solubility of CO<sub>2</sub>; Fig. 17).

1155       Differences between experimental data and isobars from IM–2012–H and -A are more compli-  
1156 cated, because the discrepancies between models and experiments are very dependent on the pressure.  
1157 For example, at 1 kbar, IM–2012–H and -A underpredict H<sub>2</sub>O and CO<sub>2</sub> solubility relative to the ex-  
1158 periments of Behrens et al. (2004), while at 5 kbar, they overpredict CO<sub>2</sub> solubility, but underpredict  
1159 H<sub>2</sub>O solubility (Fig. 16c vs.e). These discrepancies likely reflect this model being extrapolated towards  
1160 the limits of its calibration dataset in terms of both pressure (most experiments were conducted at <5  
1161 kbar) and melt composition (Fig. 17, see the next section for more discussion).

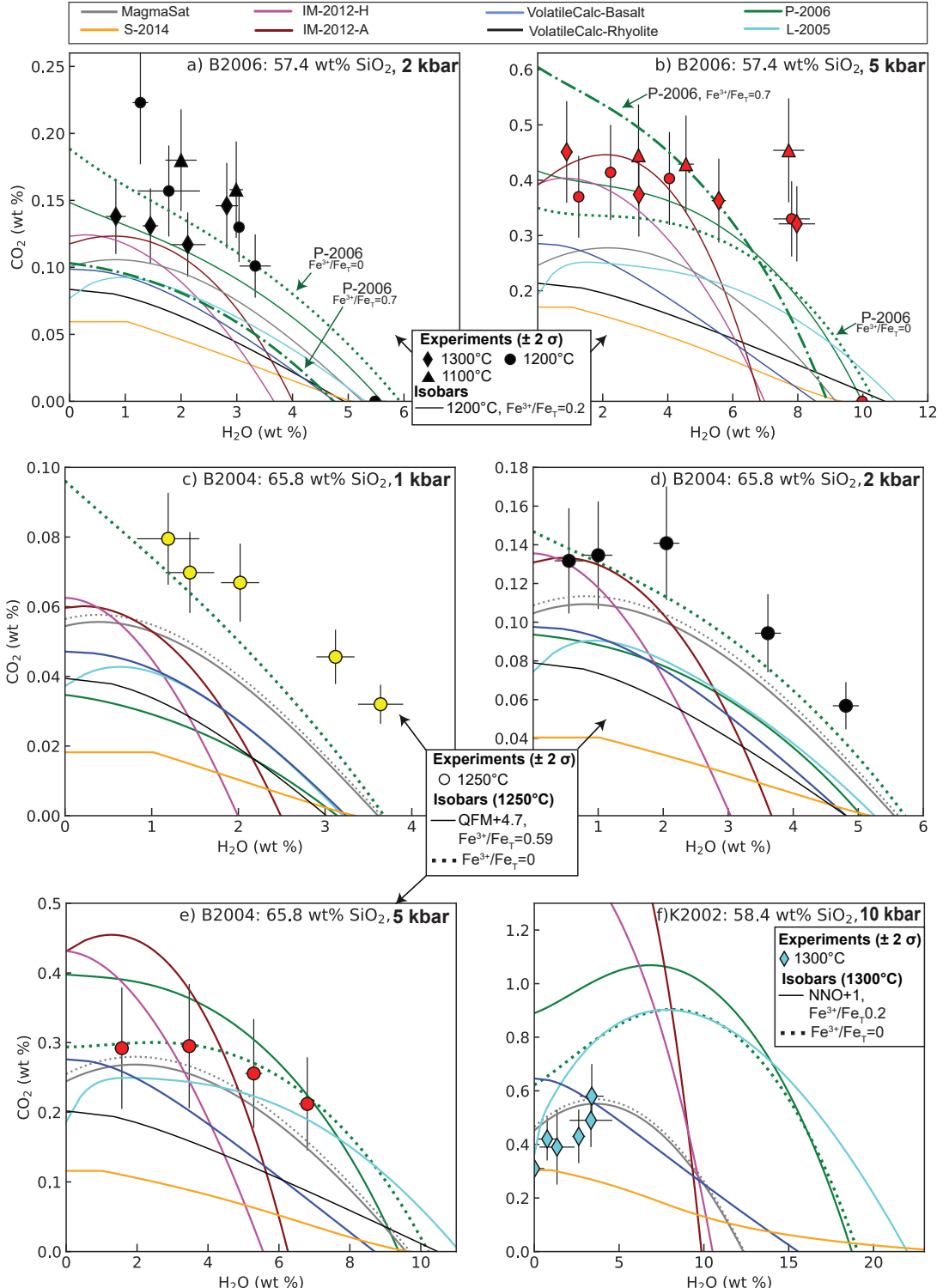


**Figure 16.** Assessing model fits to experimental data for andesitic and dacitic compositions a-b) Experiments from Botcharnikov et al. (2006). Isobars were calculated for 1200°C and  $\text{Fe}^{3+}/\text{Fe}_T = 0.2$  ( $\sim \text{QFM} + 1.5$ ). P-2006 isobars are also shown for  $\text{Fe}^{3+}/\text{Fe}_T = 0.7$  (the upper estimate of  $\text{Fe}^{3+}/\text{Fe}_T$  in experimental products; dash-dotted line), and  $\text{Fe}^{3+}/\text{Fe}_T = 0$  (dotted line) c-e) Experiments from Behrens et al. (2004). Isobars are shown for  $\text{Fe}^{3+}/\text{Fe}_T = 0.59$  ( $f\text{O}_2$  of QFM+4.7). For P-2006 and MagmaSat, isobars are also shown for  $\text{Fe}^{3+}/\text{Fe}_T = 0$ . f) Experiments from King and Holloway (2002). Isobars are shown for  $\text{Fe}^{3+}/\text{Fe}_T = 0.54$ . For P-2006 and MagmaSat, isobars are also shown for  $\text{Fe}^{3+}/\text{Fe}_T = 0$ . VolatileCalc-Rhyolite isobars are not shown, as the spreadsheet doesn't calculate isobars above 5 kbar. Error bars on all plots shows the  $2\sigma$  uncertainties from measurements of volatile contents in experimental products.  $\text{Fe}^{3+}/\text{Fe}_T$  ratios were calculated from author-stated buffers using MELTS for Excel (Gualda & Ghiorso, 2015).

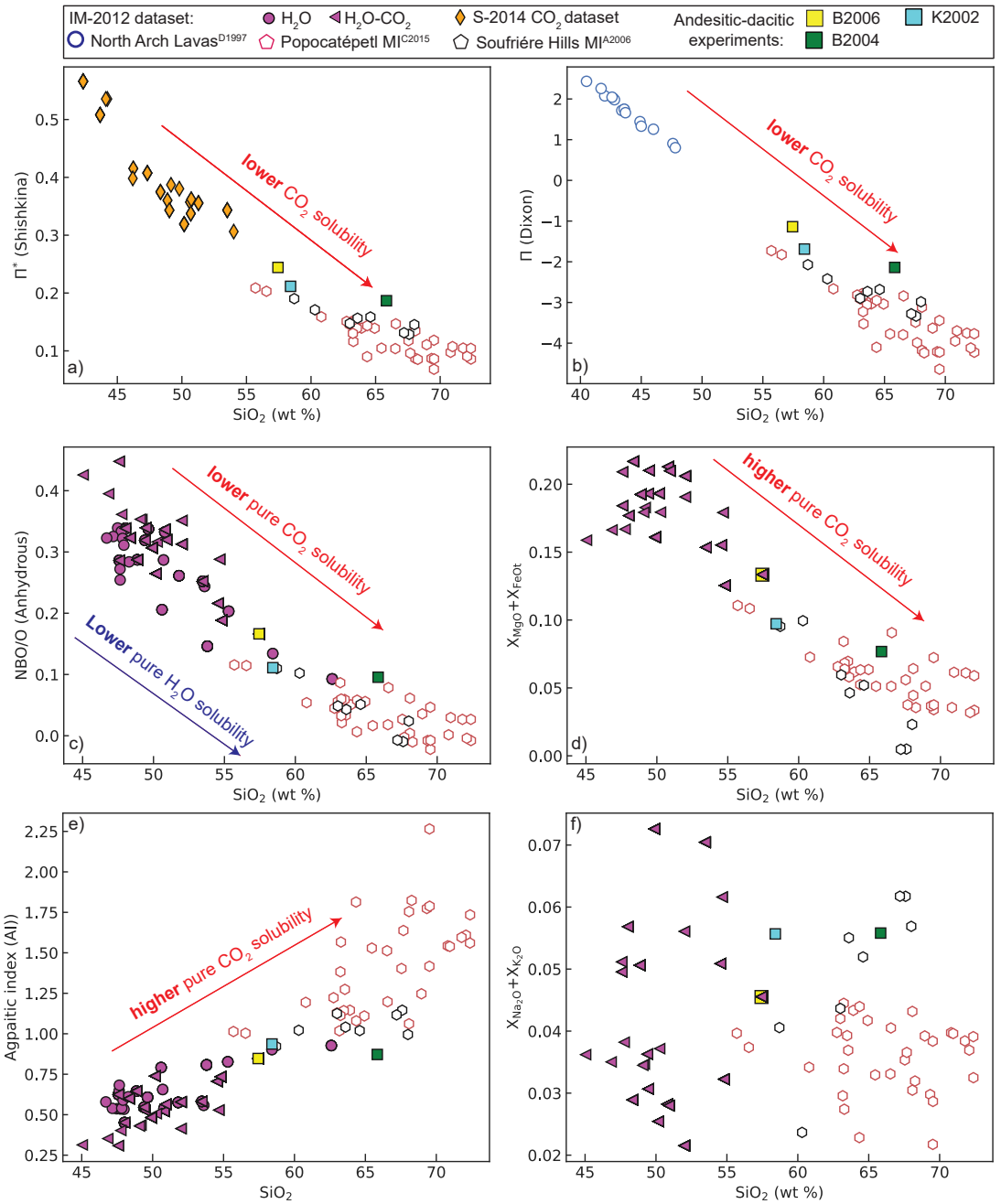


**Figure 17.** Comparing the calibration datasets of S–2014 and IM–2012 to the andesitic experiments of Botcharnikov et al. (2006), (B2006), Behrens et al. (2004), (B2004) and King and Holloway (2002), (K2002) shown in Fig. 16, and the melt inclusions from Popocatépetl (Atlas et al., 2006) and Soufrière Hills (Cassidy et al., 2015) shown in Fig. 18. Anhydrous molar fractions are used to calculate compositional parameters in parts c-f, because when accounting for discrepancies between isobars (e.g., on Fig. 18, the H<sub>2</sub>O content and therefore hydrous cation fraction varies as a function of the pressure).

The fact that no model passes through all available experiments demonstrates that further investigation of solubility in andesitic to dacitic melts is warranted. Using representative experimental  $\text{Fe}^{3+}/\text{Fe}_T$  ratios, MagmaSat is the most accurate model, predicting dissolved volatile contents within  $\sim 20\%$  of experimental products (considering reported error bars on dissolved volatile contents).

The extreme sensitivity to the  $\text{Fe}^{3+}/\text{Fe}_T$  ratio makes it very difficult to assess the accuracy of the P–2006 model (particularly given the relatively large uncertainties in the oxygen fugacity of experimental run products; King & Holloway, 2002; Botcharnikov et al., 2006). In all of the examples shown, P–2006 isobars calculated for  $\text{Fe}^{3+}/\text{Fe}_T=0$  are a better fit to the experimental data than isobars calculated using estimates of the  $\text{Fe}^{3+}/\text{Fe}_T$  ratio of experiments. This suggests that, in relatively oxidising intermediate melts, P–2006 is overestimating the effect of  $\text{Fe}^{3+}$  species on volatile solubility. It is noteworthy that P–2006 is a particularly poor match to the high pressure andesitic experiments of King and Holloway (2002), despite the fact that these are the only intermediate experiments in the calibration dataset of this model.

As all the experiments shown were used to calibrate MagmaSat, similar analysis applied to new experimental data on andesitic compositions when it becomes available will provide further constraints on the accuracy of this model. Isobars for recent solubility experiments on a basaltic-andesite at 4–12 kbar by Mangan et al. (2021) are shown in the Supplementary Fig. S4 and S5. MagmaSat is a much better fit to this new data than P–2006, with experiments performed 400–815 MPa plotting within error of calculated MagmaSat isobars. In contrast, P–2006 overpredicts  $\text{CO}_2$  solubility (regardless of  $\text{Fe}^{3+}/\text{Fe}_T$ ) at  $<600$  MPa.

## 6.2 Case Study: Intermediate melt inclusions

To assess the impact of these model differences on the depths of magma storage reservoirs inferred from melt inclusions in volcanic arcs, we calculate saturation pressures using a variety of models for two suites of melt inclusions with andesitic-dacitic liquid compositions: 1) 34 melt inclusions from Volcán Popocatépetl, Mexico with 55.7–73.4 wt%  $\text{SiO}_2$  (Figs. 2, 18a; Atlas et al., 2006), and 2) 8 melt inclusions from Soufrière Hills Volcano, Montserrat with 58.7–68.0 wt%  $\text{SiO}_2$  (Figs. 2, 18b; Cassidy et al., 2015). Both studies calculated saturation pressures (and therefore magma storage depths) using VolatileCalc-Rhyolite.

Cumulative frequency distributions for the Popocatépetl melt inclusions (Fig. 18a) shows that P–2006 predicts the lowest saturation pressures, and S–2014 the highest, with MagmaSat, IM–2012–A, VolatileCalc-Basalt, VolatileCalc-Rhyolite, and IM–2012–H lying in-between these model extremes. Based on our analysis in the previous section suggesting that MagmaSat is the best calibrated model for intermediate melt compositions, we ratio saturation pressures from each model to those determined

1195 using MagmaSat (allowing model differences to be quantified). Additionally, because MagmaSat is a  
1196 thermodynamic model that has been shown to work well for basaltic and rhyolitic compositions, it is  
1197 effectively being interpolated to andesitic-dacitic compositions which are not represented in its calibra-  
1198 tion dataset (i.e., these melt inclusion compositions), rather than extrapolated (as for empirical models  
1199 such as S-2014, VolatileCalc-Basalt, and IM-2012 which are primarily calibrated on more mafic melt  
1200 compositions; Fig. 2).

1201 The median saturation pressure for Popocatépetl melt inclusions calculated for VolatileCalc-  
1202 Rhyolite is  $1.26\times$  higher than for MagmaSat. The median for MagmaSat is  $\sim 1.2\times$  higher than for  
1203 P-2006. The deviation relative to MagmaSat increases with  $\text{SiO}_2$  content for VolatileCalc-Rhyolite  
1204 ( $\sim 1.1$  to  $1.5\times$ ), VolatileCalc-Basalt ( $\sim 1$  to  $1.35\times$ ), and L-2005 ( $\sim 1$  to  $1.4\times$ ). The deviation between  
1205 S-2014 and MagmaSat is very large, increasing from a factor of 2 at  $\sim 55$  wt%  $\text{SiO}_2$  to  $\sim 5.5\times$  at 72.5  
1206 wt%  $\text{SiO}_2$ . The deviation between IM-2012-H and -A and P-2006 vs. MagmaSat shows no clear cor-  
1207 relation with  $\text{SiO}_2$  content (Supporting Fig. S6). The presence of discrepancies which correlate with  
1208 melt composition is particularly concerning, because it means that choice of an inappropriate solubility  
1209 model may introduce systematic error into a dataset as a function of melt inclusion composition.

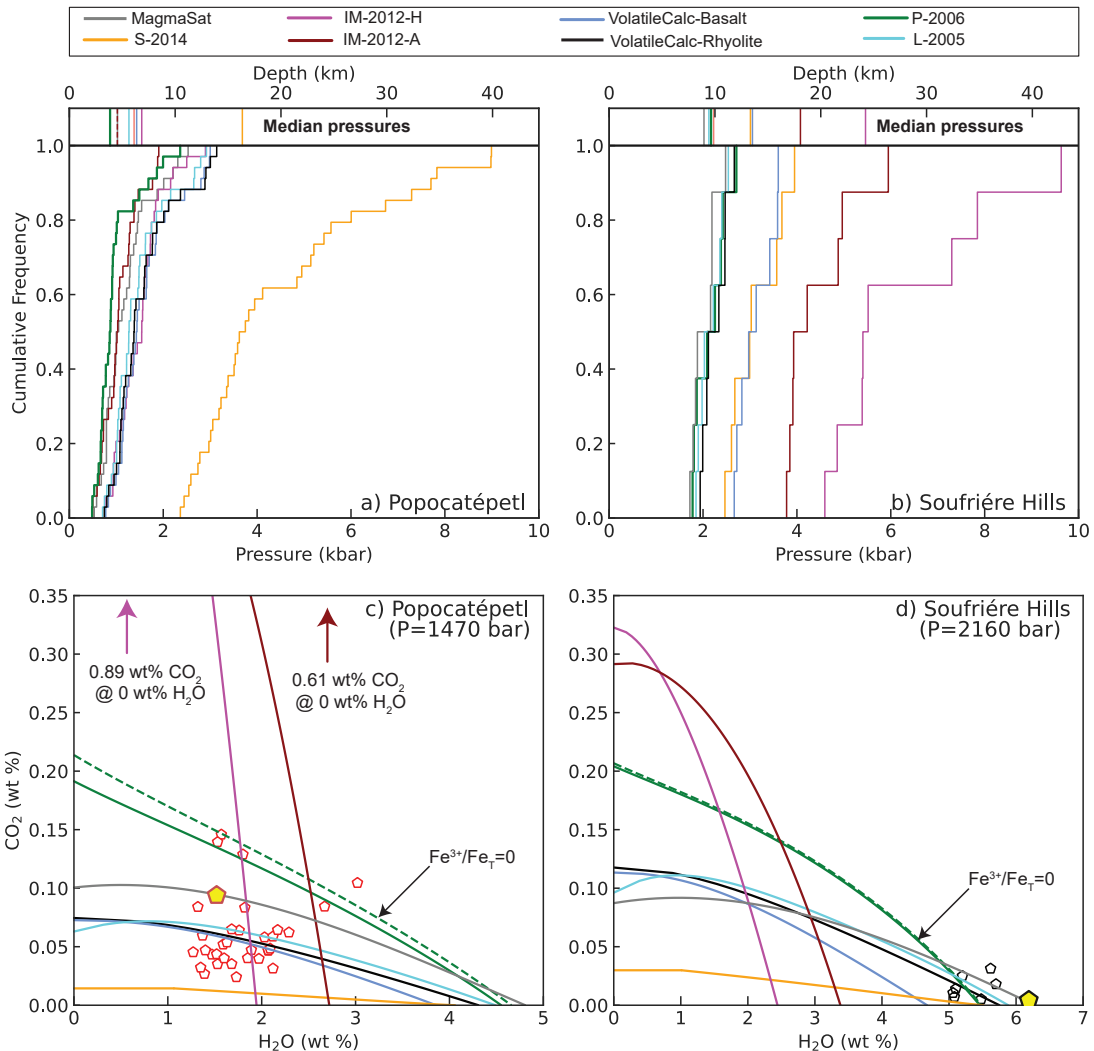


**Figure 18.** a-b) Cumulative distribution functions of saturation pressures from different models for melt inclusions from a) Popocatépetl (Atlas et al., 2006) and b) Soufrière Hills (Cassidy et al., 2015). Fe<sup>3+</sup>/Fe<sub>T</sub> was set to 0.15. c) Isobars from different models calculated at the saturation pressure from MagmaSat (1470 bar) for the Popocatépetl melt inclusion shown with a yellow pentagon (at 1050°C following Atlas et al., 2006). The scale is trimmed to emphasize the differences between models at lower CO<sub>2</sub> contents, with the interception of the IM-2012 isobars with the y axis labelled on the plot. d) Isobars from different models calculated at the saturation pressure from MagmaSat (2160 bar) for the Soufrière Hills melt inclusion shown with a yellow pentagon (at 1000°C following Cassidy et al., 2015). Isobars are also shown for P-2006 with Fe<sup>3+</sup>/Fe<sub>T</sub>=0 (dotted line)

MagmaSat predicts the lowest saturation pressures for the Soufrière Hills melt inclusions, with

L-2005, P-2006, and VolatileCalc-Rhyolite predicting reasonably similar pressures. VolatileCalc-

1212 Basalt, S–2014 and IM–2012–A and –H are offset to higher pressures. Similar to the results for  
 1213 Popocatépetl, the ratio of saturation pressures for Soufrière Hills melt inclusions relative to MagmaSat  
 1214 for L–2005 ( $\sim 1$  to  $1.1 \times$ ), VolatileCalc–Basalt ( $\sim 1.25$  to  $1.35 \times$ ) and VolatileCalc–Rhyolite ( $\sim 1.05$  to  
 1215  $1.17 \times$ ) increase with increasing  $\text{SiO}_2$  (Supporting Fig. S7). Unlike Popocatépetl melt inclusions, the  
 1216 discrepancy between IM–2012 and MagmaSat increases dramatically with increasing  $\text{SiO}_2$  (from  $\sim 1.5$   
 1217 to  $2.5 \times$  for anhydrous, and 2 to  $4.5 \times$  for hydrous), while that for S–2014 shows a weak negative corre-  
 1218 lation with  $\text{SiO}_2$  (from  $\sim 1.7$ – $1.35 \times$ ).

1219 The large discrepancies shown by IM–2012 (for Soufrière Hills) and S–2014 (for Popocatépetl)  
 1220 are best understood by examining an isobar calculated for the inclusion showing the largest deviation  
 1221 relative to MagmaSat in each dataset ( $\text{SiO}_2 = 72.4$  wt% for Popocatépetl, and 67.6 wt% for Soufrière  
 1222 Hills; yellow pentagon on Fig. 18c-d) at the saturation pressure obtained from MagmaSat. For both  
 1223 sets of inclusions, S–2014 isobars intercept the x axis at similar  $\text{H}_2\text{O}$  contents to other models, but in-  
 1224 tercept the y axis at drastically lower  $\text{CO}_2$  contents. This underestimation of  $\text{CO}_2$  solubility likely re-  
 1225 sults from the fact that the  $\Pi^*$  values of these inclusions lie well below that of the calibration dataset  
 1226 (as discussed for andesitic experiments; Fig. 17b).

1227 In contrast, IM–2012 predicts very high pure  $\text{CO}_2$  solubility, and low pure  $\text{H}_2\text{O}$  solubility relative  
 1228 to the other models. Both IM–2012 models express the compositional dependence of  $\text{H}_2\text{O}$  solubility in  
 1229 terms of the parameter NBO/O, with melts with higher NBO/O values having higher  $\text{H}_2\text{O}$  solubility  
 1230 (equation 15). Both sets of melt inclusions possess much lower NBO/O values than the calibration  
 1231 dataset of IM–2012 (Fig. 17c-d). This is problematic, because the empirical relationship between  
 1232 NBO/O and pure  $\text{H}_2\text{O}$  solubility incorporated by IM–2012 has not been validated for these melt com-  
 1233 positions. For example, Shishkina et al. (2014) show that IM–2012 drastically overestimates  $\text{H}_2\text{O}$   
 1234 solubility in their basanite and nephelinite melt compositions. They point out that while IM–2012  
 1235 conclude that there is only a small effect of melt composition on  $\text{H}_2\text{O}$  composition, the IM–2012 model  
 1236 ends up showing a strong sensitivity to melt composition when extrapolated to the high NBO/O ratio  
 1237 in their basanite and nephelinite melts (and we invoke a similar explanation for the lower NBO/O  
 1238 ratios in melt inclusions discussed here).

1239 The IM–2012 expression for  $\text{CO}_2$  solubility is more complicated, containing terms for the Ag-  
 1240 paitic index (AI), NBO/O,  $X_{\text{Na}_2\text{O}+\text{K}_2\text{O}}$ ,  $X_{\text{FeO}+\text{MgO}}$  and  $X_{\text{H}_2\text{O}}$  (equation 11). These two sets of melt  
 1241 inclusions have higher AI, lower NBO/O ratios, similar values of  $X_{\text{Na}_2\text{O}+\text{K}_2\text{O}}$ , and lower  $X_{\text{FeO}+\text{MgO}}$   
 1242 values than the calibration dataset (Fig. 17d-f). While the effect of NBO/O is more convoluted be-  
 1243 cause it also affects the solubility of  $\text{H}_2\text{O}$  (which feeds back into the expression for  $\text{CO}_2$ ), it is readily  
 1244 apparent that the positive coefficient attached to the AI term combined with the negative coefficient

1245 attached to the MgO+FeO term causes this model to predict higher CO<sub>2</sub> solubilities than the calibra-  
 1246 tion dataset for the andesitic-dacitic melt inclusions considered here.

1247 The discrepancy between isobars for S–2014 and IM–2012 relative to MagmaSat are relatively  
 1248 similar for the Popocatépetl and Soufrière Hills melt compositions, while discrepancies for saturation  
 1249 pressures differ markedly (Fig. 18a-b vs. c-d). This is because the volatile contents of Popocatépetl  
 1250 melt inclusions are significantly more CO<sub>2</sub>-rich (~0.02–0.15 wt% and higher), and H<sub>2</sub>O-poor (~1–3  
 1251 wt%) than Soufrière Hills melt inclusions (<0.04 wt% CO<sub>2</sub> and 5–6 wt% H<sub>2</sub>O). For this reason, cal-  
 1252 culated saturation pressures for Popocatépetl melt inclusions are sensitive to the treatment of both  
 1253 CO<sub>2</sub> and H<sub>2</sub>O in solubility models (Fig. 18b), while those for Soufrière Hills melt inclusions are mostly  
 1254 sensitive to pure H<sub>2</sub>O solubility. Thus, S–2014 overestimates saturation pressures for Popocatépetl  
 1255 melt inclusions because this model drastically underestimates the solubility of pure CO<sub>2</sub>. In contrast,  
 1256 S–2014 only slightly underestimates H<sub>2</sub>O solubility relative to MagmaSat, so only slightly overpredicts  
 1257 saturation pressures for H<sub>2</sub>O-rich Soufrière Hills melt inclusions. The discrepancy between IM–2012  
 1258 and MagmaSat is much smaller for Popocatépetl relative to Soufrière Hills because, fortuitously, the  
 1259 IM–2012–H isobar intercepts the MagmaSat isobar at H<sub>2</sub>O contents similar to these Popocatépetl melt  
 1260 inclusions. IM–2012–H and -A drastically underestimates the solubility of pure H<sub>2</sub>O, so overestimates  
 1261 saturation pressures for the H<sub>2</sub>O-rich Soufrière Hills melt inclusions relative to other models.

1262 It is worth noting that Iacono-Marziano never intended their model to be applied to andesites,  
 1263 and when discussing the limitations of their model, they explicitly warn that their empirical expres-  
 1264 sions poorly incorporates the effect of MgO and FeO on CO<sub>2</sub> solubility because of the restricted range  
 1265 of these oxides in the calibration dataset. We have included this discussion as an extreme example of  
 1266 the danger of extrapolating empirical models beyond their calibration range. However, the sensitiv-  
 1267 ity of this model to the FeO and MgO content of the melt also presents issues when applied to high  
 1268 MgO basaltic liquids. For example, Wieser et al. (2021) show that IM–2012 predicts higher saturation  
 1269 pressures for highly primitive (high MgO) melt inclusions from Kīlauea Volcano relative to S–2014 and  
 1270 MagmaSat. This likely reflects the higher values of X<sub>FeO+MgO</sub> in these melt inclusions relative to the  
 1271 calibration dataset, which causes IM–2012 to predict lower CO<sub>2</sub> solubility (the opposite directionality  
 1272 to that seen for the intermediate melt inclusions discussed here).

1273 The H<sub>2</sub>O-rich nature of Soufrière Hills melt inclusions means that VolatileCalc-Rhyolite pre-  
 1274 dicted much more similar saturation pressures to MagmaSat (1.07–1.15×; Supporting Figure S6) than  
 1275 for Popocatépetl (1.1–1.5× higher; Supporting Figure S5), because the main failure of VolatileCalc-  
 1276 Rhyolite for intermediate compositions at moderate to high temperatures (>850 C) is its prediction  
 1277 of pure CO<sub>2</sub> solubility (Figs. 16, 18c-d). The discrepancy for both VolatileCalc models and L–2005

relative to MagmaSat is significantly smaller than for S–2014 and IM–2012. This is because the solubility differences during evolution for basaltic to rhyolitic compositions are relatively small (30–40%) compared to the error associated with the extrapolating an empirical model far beyond its compositional range. Overall, this case study shows the importance of checking that the calibration dataset of a model contains melts similar to those in the sample set of interest, particularly if the effect of melt composition is parameterized empirically.

## 7 Best practices for data visualization and curation

### 7.1 Isobar Diagrams: limitations and alternatives

As demonstrated by the preceding section, isobar diagrams are a useful tool to visualize variations in volatile solubility for a specific melt composition. However, many suites of melt inclusions have considerable major element variability, which translates into differing solubilities of H<sub>2</sub>O-CO<sub>2</sub> at a given pressure, and different isobar shapes at a given pressure (Wieser et al., 2021; Roggensack, 2001; Iacovino et al., 2021). We use two suites of melt inclusions to demonstrate this point.

First, we consider a suite of basaltic melt inclusions from Butajira volcanoes in the Main Ethiopian Rift from Iddon and Edmonds (2020). We calculate isobars for a representative inclusion composition (BJ08\_7; Fig. 19a), and then we compare these to the isobars calculated for each individual melt inclusion composition at 1 and 3 kbar (Fig. 19a-b). 3 kbar isobars calculated from the composition of each individual melt inclusion from Butajira (Fig. 19b) cover the entire region of H<sub>2</sub>O-CO<sub>2</sub> space that is bracketed by the 2 and 4 kbar isobars calculated in MagmaSat for the representative melt inclusion composition (Fig. 19b vs. a). In fact, saturation pressures calculated using any given melt inclusion composition vs. the major element composition of the melt inclusion in question can affect the saturation pressure by almost a factor of 2. By extension, visual inspection of melt inclusion volatile concentrations plotted on isobar diagrams may be associated with an error of this magnitude).

Second, we calculate isobars at 300 and 700 bars for a representative subset of melt inclusions from the 2018 eruption of Kīlauea with PEC-corrected MgO contents between 6.4 to 13.5 wt% (Wieser et al., 2021). Although less extreme than the Butajira example, the spread of isobars calculated for a single sample at 700 bars for multiple melt inclusions is wider than the distance between isobars calculated 100 bar apart for a specific melt inclusion. Similar isobar spreads are seen for both Kīlauea and Butajira using IM–2012 (Supporting Fig. S8 and S9).

VESIcal solves the problem of potentially misleading isobar diagrams by facilitating rapid calculations of saturation pressures for large suites of melt inclusions. For example, calculating saturation pressures for the 33 melt inclusions in the dataset of Iddon and Edmonds (2020) using VolatileCalc-Basalt, S–2014, and IM–2012 takes only 4.2 seconds if VESIcal is run on the ENKI server. MagmaSat

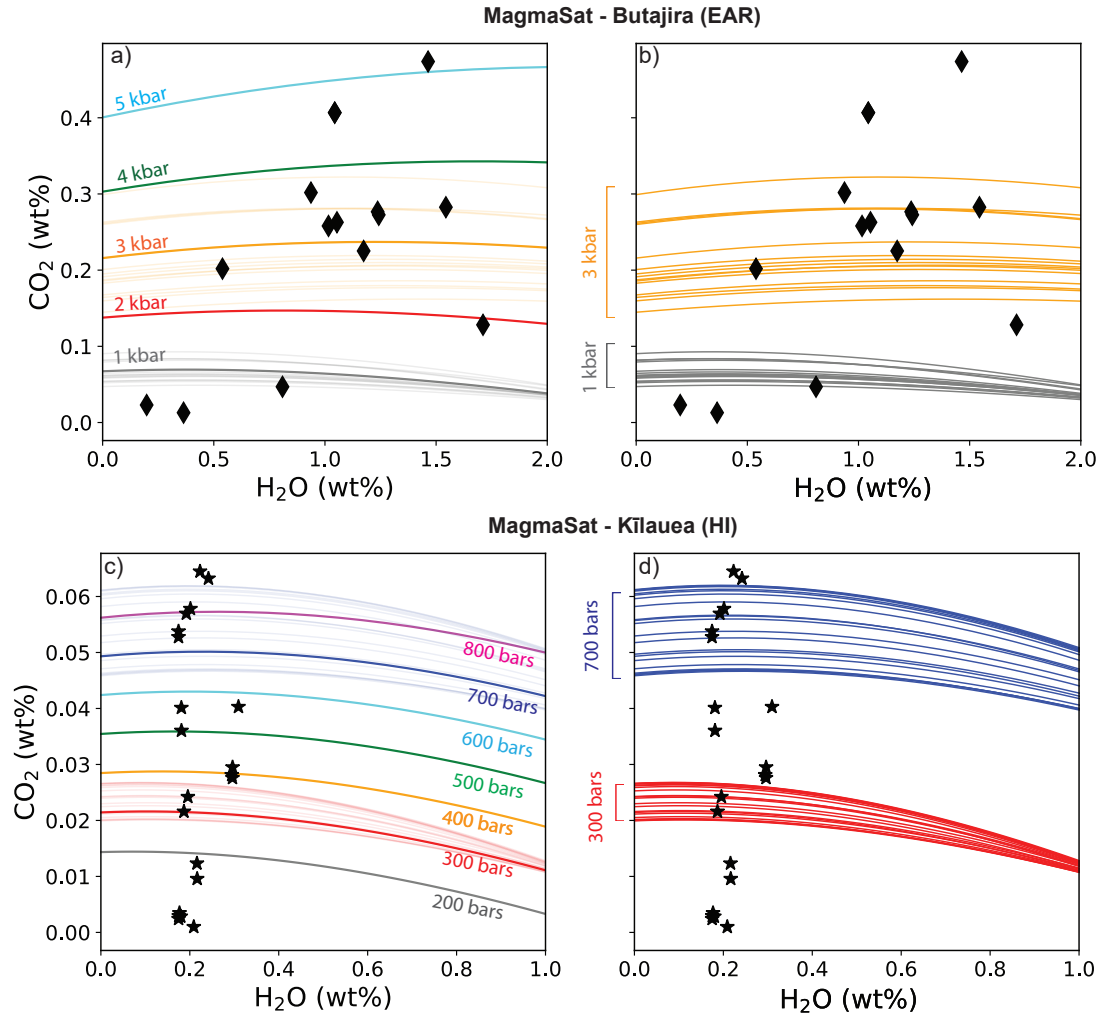


**Figure 19.** a-b) Isobars for olivine-hosted melt inclusions from Iddon and Edmonds (2020) calculated at 1170°C. a) MagmaSat isobars for melt inclusion BJ08\_7 from Butajira with melt inclusion volatile data overlain. b) 1 and 3 kbar isobars calculated for the major element composition of each individual melt inclusion from Butajira (underlain as light lines in a). c-d) As for a-b, but using a representative subset of melt inclusions from Kilauea (Wieser et al., 2021). To save computation time as this study analyses >100 melt inclusions, PEC-corrected compositions were sorted by MgO content, and every 5th inclusion composition was used to calculate an isobar. Isobars are calculated for a temperature calculated from the melt inclusion MgO content using the thermometer of Helz and Thornber (1987).

1311 is slightly slower, taking 31.5 seconds (still <1 s per sample). MagmaSat calculations may run faster  
 1312 if ThermoEngine is installed locally (calculations take 26.3 s using a Dell Inspiron laptop with 16 GB

1313 RAM and an Intel-i7 processor, see <https://gitlab.com/ENKI-portal/ThermoEngine> for installation  
1314 help).

1315 Once users have calculated saturation pressures for each inclusion, a number of different x-y plots  
1316 will provide more information than isobar diagrams. For example, G. Moore (2008) suggests that users  
1317 could plot two graphs, one showing melt inclusion CO<sub>2</sub> content against saturation pressure and one  
1318 showing melt inclusion H<sub>2</sub>O contents against saturation pressure. This allows clustering of saturation  
1319 pressures to be observed, and determination of the importance of each volatile species when calculat-  
1320 ing saturation pressure. Alternatively, saturation pressures could be plotted as histograms, cumulative  
1321 density functions, or box/violin plots to assess clustering, and to compare distributions from different  
1322 crystal populations, eruptions, or different volcanic centres. It may also be advantageous to compare  
1323 saturation pressures to host-crystal chemistry. For example, Wieser et al. (2021) show that melt in-  
1324 clusions hosted in low forsterite olivine crystals from Kilauea Volcano crystallized at ~1–2 km depth,  
1325 while melt inclusions hosted within higher forsterite olivines crystallized at ~3–5 km depth.

## 1326 7.2 Assessing Errors

1327 The ability to calculate saturation pressures using a number of different models in VESIcal is  
1328 advantageous, because it can provide assessment of the systematic errors associated with model choice.  
1329 If different solubility models produce saturation pressures which are statistically distinguishable using  
1330 tests such as ANOVA or the Kolmogorov-Smirnov test, or differences between models exceed 10–20%  
1331 (the approximate quoted error on most models), users need to evaluate their melt compositions, pres-  
1332 sures and temperatures in the context of the calibration dataset of each solubility model. Several  
1333 Juptyer notebooks aiding these comparisons are provided alongside VESIcal part I (Iacovino et al.,  
1334 2021). Additionally, comparisons between any available experimental data for relevant melt com-  
1335 positions and different solubility models using a workflow similar to that used here for andesites (e.g.,  
1336 isobar diagrams as in Fig. 16, plots of melt composition vs. calibration datasets) will help users select  
1337 a suitable model. As well as examining melt compositions, users should also evaluate whether they  
1338 are extrapolating temperature-sensitive models beyond the calibration range (as discussed here for  
1339 VolatileCalc-Rhyolite).

1340 In general, if a natural silicate melt composition is poorly represented by experimental data,  
1341 MagmaSat is probably the best model to use, as its thermodynamic nature is more suitable to extrap-  
1342 olation to melt compositions not represented in the calibration dataset than empirical models such  
1343 as IM–2012, S–2014, or VolatileCalc-Basalt. However, the comprehensive nature of MagmaSat means  
1344 that the fit to experimental data from any specific region of major element space is compromised by  
1345 the fact the model is optimizing the overall fit to many different major element compositions. Thus,

1346 where present, models developed for specific volcanic centres, or highly weighted towards specific melt  
 1347 compositions (e.g., A–2019 for the 6 centers they investigate, or IM–2012 for alkaline compositions)  
 1348 may return a better fit. While these composition-specific models may be well calibrated in terms of  
 1349 melt composition, users must also check that they are applying the model within the recommended  
 1350 pressure and temperature range.

1351 VESIcal can also be used to explore the effects of uncertainty in input parameters (as in the sen-  
 1352 sitivity tests presented here). Error bars for calculated saturation pressures are asymmetrical, even for  
 1353 input parameters with symmetric error distributions. Thus, to calculate an error bar on each inclusion,  
 1354 three saturation pressure calculations must be performed. Using the older generation of tools, this  
 1355 would be exceptionally time consuming. Using VESIcal, calculations can be performed automatically,  
 1356 and users could simply input three spreadsheets, or a spreadsheet with three columns for the uncer-  
 1357 tain parameter (containing the preferred, maximum and minimum value) to calculate error bars (e.g.,  
 1358 uncertainties in total CO<sub>2</sub> contents resulting from 2D measurements of bubble volumes and analytical  
 1359 uncertainties in diad splittings; Wieser et al., 2021).

1360 VESIcal also opens up the capability to handle errors arising from volatile solubility modelling  
 1361 using the advanced functionality of Python3 packages such as Numpy, SciPy and PyMC to perform  
 1362 Bayesian statistical techniques (e.g., Markov Chain Monte Carlo methods). This would allow the un-  
 1363 certainty in all input parameters (e.g., temperature, analytical uncertainties in volatile and major  
 1364 element contents, uncertainty arising from post-entrapment crystallization corrections) into a resulting  
 1365 error distribution for each melt inclusion. These techniques are increasingly being utilized by igneous  
 1366 petrologists, with recent applications including calculating error distributions for diffusion timescales  
 1367 (Mutch et al., 2019), the contribution of melts from distinct mantle sources (Gleeson et al., 2020), and  
 1368 propagating uncertainties in vapour bubble growth models (Rasmussen et al., 2020).

### 1369 7.3 Data Curation

1370 Now that VESIcal makes it possible to calculate saturation pressures for large melt inclusion  
 1371 datasets in short amounts of time, it is vital that data is published in a way that allows such calcu-  
 1372 lations to be performed retrospectively (e.g., using the same solubility model to calculate saturation  
 1373 pressures for a literature compilation). The concentration of major elements and volatile elements  
 1374 should be provided within a single spreadsheet or database, ideally alongside the composition of the  
 1375 mineral host. Additionally, if melt inclusions are corrected for post-entrapment crystallization (PEC),  
 1376 both raw and corrected major and volatile element concentrations should be published. Particularly  
 1377 for more chemically-complex host minerals like pyroxene and plagioclase, it is highly likely that com-  
 1378 munity standards on the best PEC procedure will change with time. Even for olivine-hosted melt

1379 inclusions, there a variety of correction techniques used in the literature, which can predict very vari-  
 1380 able amounts of PEC (Wieser et al., 2021, show that the PEC routine in Petrolog3 predicts 30% more  
 1381 PEC than corrections based on Mg# disequilibrium between the host and melt inclusion). Finally,  
 1382 given that numerous recent studies have shown that bubble CO<sub>2</sub> contents can change calculated satu-  
 1383 ration pressures by up to an order of magnitude (section 5), authors should also make note of whether  
 1384 each melt inclusion contained a vapour bubble (and ideally an estimate of the volume proportion of  
 1385 the vapour bubble). This information may allow the CO<sub>2</sub> contents in vapour bubbles to be recon-  
 1386 structed theoretically by future studies, given the recent proliferation of vapour bubble growth models  
 1387 (e.g. Aster et al., 2016; Rasmussen et al., 2020; Maclennan, 2017).

1388 Proper data curation is particularly vital in the world of volatile solubility modelling because it  
 1389 is very likely that many more experiments will be published over the next decade, allowing the cre-  
 1390 ation of new solubility models that are calibrated over an even wider region of P-T and compositional  
 1391 space. Many publications could not be used for comparisons in this study, because there was simply no  
 1392 way to combine volatile element concentrations and major element concentrations (which were often  
 1393 reported in different tables with non-unique or non-matching sample names), or not reported at all. It  
 1394 would be a great shame if published melt inclusion datasets could not be input into these new models  
 1395 to recalculate saturation pressures, and gain a greater understanding of magma storage in the Earth's  
 1396 crust.

## 1397 8 Future work

1398 The comparisons drawn in this review highlight several research areas where further experimental  
 1399 work is required to be able to distinguish which model behaviors are accurate. First, significantly more  
 1400 experiments are needed on andesitic-dacitic melt compositions. Figure 16 shows that it is currently  
 1401 impossible to differentiate a potential failure in any given solubility model from anomalies in any given  
 1402 set of experiments (e.g., the differential effect of addition of H<sub>2</sub>O on CO<sub>2</sub> solubility in different experi-  
 1403 ments; Fig. 16b. vs f).

1404 One of the challenges when assessing CO<sub>2</sub> solubility in andesitic-dacitic melts is the fact that  
 1405 CO<sub>2</sub> is present as both carbonate and molecular CO<sub>2</sub>. Carbon species do appear separately in FTIR  
 1406 spectra, but the accuracy of FTIR-derived volatile concentrations can be affected by peak over-  
 1407 lap (e.g., Brooker et al., 2001b), as well as uncertainty in peak baseline and absorption coefficients  
 1408 (Botcharnikov et al., 2006; Mangan et al., 2021). SIMS cannot distinguish different carbon species  
 1409 (only yields total carbon), but may help to resolve issues with FTIR as a result of increased under-  
 1410 standing of the optimal analysis conditions for volatiles in silicate glasses of the last few decades.  
 1411 However, in addition to its substantial cost relative to FTIR, accurate SIMS measurements are reliant

1412 on having a suite of standards with similar major element compositions and a range of volatile con-  
1413 tents (and these standards are often characterized by FTIR, so are subject to the caveats mentioned  
1414 above).

1415 Second, the effect of redox on volatile solubility across the range encountered in terrestrial mag-  
1416 mas is still poorly constrained (section 5). This discrepancy largely reflects the fact that the redox  
1417 conditions at which many experiments in the literature were conducted are uncertain and/or highly  
1418 variable (e.g., Botcharnikov et al., 2006). Because of this uncertainty, many calibration datasets are  
1419 built without being able to constrain the quantities of  $\text{Fe}_2\text{O}_3$  and  $\text{FeO}$  for each experimental run.  
1420 While our investigation of intermediate melts indicates that the strong sensitivity of  $\text{CO}_2$  solubility  
1421 to melt redox shown by P-2006 is likely anomalous because of the presence of experiments with ex-  
1422 tremely high calculated  $\text{Fe}^{3+}/\text{Fe}_T$  ratios in the calibration dataset, further experiments where  $\text{Fe}_2\text{O}_3$   
1423 and  $\text{FeO}$  proportions are accurately measured are needed to be certain that this behaviour is not real.  
1424 It is also noteworthy that almost all the andesitic experiments were performed at higher oxygen fugac-  
1425 ities than lavas erupted at volcanic arcs. When the calibration dataset for a given set of compositions  
1426 is so small, this makes it difficult to deconvolve changes in volatile solubility with melt composition  
1427 compared to redox. Recent advances in measurements of  $\text{Fe}^{3+}/\text{Fe}_T$  using Fe K-edge micro-X-ray ab-  
1428 sorption near-edge structure (XANES) spectroscopy in hydrous glasses (Cottrell et al., 2018) could  
1429 provide an avenue to better constrain this parameter in future (and past) experimental products.

1430 It is also worth noting that all the models discussed here only consider the effect of redox  
1431 through terms for  $\text{Fe}^{2+}$  and  $\text{Fe}^{3+}$  in the melt, constraining their applicability to melts more oxidising  
1432 than the IW buffer. In more reducing conditions, the co-existing  $\text{CO}_2$ -rich phase may be graphite or  
1433 diamond rather than a  $\text{CO}_2$ -rich vapour phase (Eguchi & Dasgupta, 2018), and the dissolved volatile  
1434 species may be  $\text{CO}$ ,  $\text{CH}_4$  and  $\text{H}_2$  (Mysen et al., 2009). This means that extreme caution is required  
1435 when applying these solubility models to highly reducing conditions such as those found on other  
1436 planetary bodies (e.g., the Moon, Mars and Mercury; Li et al., 2017).

1437 Third, there is still significant uncertainty regarding the exact nature of  $\text{H}_2\text{O}$  and  $\text{CO}_2$  mixing  
1438 at higher pressure. This reflects the difficulty in measuring mixed  $\text{H}_2\text{O}-\text{CO}_2$  fluids that were in equi-  
1439 librium with the melt during the experiment. If measured at all, methods in the literature span from  
1440 puncture and weight loss of frozen capsules (i.e., when frozen the  $\text{CO}_2$  is released, but not the  $\text{H}_2\text{O}$ ;  
1441 Shishkina et al., 2010) to more sophisticated and accurate vacuum line manometry (G. Moore et al.,  
1442 2008; Iacobino et al., 2013; Allison et al., 2019). New infinite path laser spectrometry technology may  
1443 offer potential improvement of this critical measurement, but challenges associated with small sample

1444 sizes remain. More work determining the pure CO<sub>2</sub> solubility as a function of pressure and tempera-  
 1445 ture would also be of great benefit in constraining the behavior of H<sub>2</sub>O-poor fluids.

1446 Fourth, we show that the sensitivity of dissolved volatile contents to temperature is highly  
 1447 model-specific. Given the difficulties with constraining temperature sensitivity experimentally (Iacono-  
 1448 Marziano et al., 2012), we suggest that it may be best to parametrize future empirical model at a  
 1449 single temperature (e.g., A–2019, S–2014), or incorporate the temperature sensitivity predicted by  
 1450 thermodynamical models, rather than introduce a spurious temperature dependency which is not  
 1451 founded in experimental data, nor consistent with the relative entropy of melt and fluid terms.

1452 Finally, it is worth noting that all of the solubility models discussed only consider H<sub>2</sub>O-CO<sub>2</sub> in  
 1453 the vapour phase, while in reality, natural fluids in volcanic systems may contain relatively large pro-  
 1454 portions of F, Cl, and S, as well as a separate brine phase (Botcharnikov et al., 2007). Additionally,  
 1455 at higher pressures and temperatures, significant quantities of major element species will dissolve into  
 1456 a H<sub>2</sub>O-rich fluid (e.g., Si, Na, K), with silicate melt and hydrous fluids becoming completely miscible  
 1457 above a critical temperature (Bureau & Keppler, 1999). This causes a pure H<sub>2</sub>O model to underesti-  
 1458 mate the true solubility of H<sub>2</sub>O at these conditions. Combined with the fact that it is near-impossible  
 1459 to quench silicate melts with  $>9\pm1$  wt% H<sub>2</sub>O to a glass phase which can be analysed by SIMS or  
 1460 FTIR (Gavrilenko et al., 2019; Mitchell et al., 2017), quantifying the solubility of H<sub>2</sub>O at condition  
 1461 relavant to lower crustal magma storage will require experimental innovations (e.g. Makhluf et al.,  
 1462 2020; Mitchell et al., 2017), in addition to developing models capable of calculating equilibria between  
 1463 a silicic melt phase and a complex aqueous fluid (Ghiorso & Sverjensky, 2016; Sverjensky et al., 2014;  
 1464 Huang & Sverjensky, 2019).

## 1465 9 Conclusion

1466 This review uses the new open-source Python3 tool VESIcal (Iacovino et al., 2021), in addition  
 1467 to VolatileCalc (Newman & Lowenstern, 2002) and Solwcad (Papale et al., 2006) to draw extensive  
 1468 comparisons between the behaviour of 9 different solubility models for a range of melt compositions.  
 1469 We show that these models predict surprisingly different volatile solubilities, particularly for pure  
 1470 CO<sub>2</sub> or mixed CO<sub>2</sub>-H<sub>2</sub>O fluids. Even for melt compositions that are well represented in the calibra-  
 1471 tion datasets of multiple models (e.g., MORBs), calculated solubilities for pure CO<sub>2</sub> can deviate from  
 1472 one another by factors of  $\sim 2$ . Differential treatment of H<sub>2</sub>O-CO<sub>2</sub> mixing enhances these differences  
 1473 when calculating volatile solubility for melts containing both volatile species. The solubility of CO<sub>2</sub>  
 1474 predicted by different rhyolitic models also differs substantially, overwhelming other sources of uncer-  
 1475 tainty such as analytical errors on measurements of volatile contents or uncertainties in crustal density

1476 profiles. Differences are most pronounced for peralkaline rhyolites where there are fewer experimental  
1477 constraints.

1478 Overall, these comparisons demonstrate that it is vital to pick a model which is calibrated for  
1479 the pressure, temperature, and melt composition of interest. Choice of a poorly calibrated model could  
1480 introduce a systematic error of a factor of 2 or more in estimates of saturation pressures. This has  
1481 widespread implications for published estimates of magma storage depths within volcanic systems, and  
1482 indicates that re-evaluation of published magma storage depths calculated using older models may be  
1483 warranted.

1484 We also investigate the sensitivity of different models to variation in parameters such as H<sub>2</sub>O  
1485 content (with relevance to diffusive re-equilibration), CO<sub>2</sub> content (with relevance to melt inclusion  
1486 vapour bubble growth), temperature and oxygen fugacity. We suggest that by performing similar sen-  
1487 sitivity tests in the future, the uncertainties affecting calculations of volatile solubility in magmatic  
1488 systems (and therefore the limitations of each study) can be quantified. We also demonstrate that iso-  
1489 bar diagrams are a poor visualization method for determining magma storage depths in systems where  
1490 melt inclusions possess diverse melt inclusion chemistry, so encourage users to take advantage of the  
1491 ease and speed of calculations in VESIcal to determine the saturation pressure for each melt inclusion  
1492 of interest. Saturation pressures can then be visualized as various cumulative frequency distributions,  
1493 histograms, or violin plots, and plotted against melt inclusion H<sub>2</sub>O and CO<sub>2</sub> contents, or parameters  
1494 relating to host crystal chemistry, to gain greater insight into the factors controlling magma storage  
1495 depths within volcanic systems.

1496 Finally, we identify that further experimental constraints are required to accurately estimate  
1497 volatile solubility in andesitic-dacitic melts, and that further work is needed to understand the effect of  
1498 temperature, redox, and non-ideal mixing between H<sub>2</sub>O-CO<sub>2</sub> on volatile solubility.

1499

## 1500 Acknowledgments

1501 PW acknowledges funding from a NERC DTP studentship (NE/L002507/1) and a National Science  
1502 Foundation grant (1948862). KI and GMM were supported by the NASA Jacobs JETS Contract  
1503 (NNJ13HA01C). We thank Jackie Dixon, Giada Iacono-Marziano, Paolo Papale, and Mark Ghiorso  
1504 for help tracking down and using existing calculation tools, and for help constructing model calibra-  
1505 tion datasets. We also thank Mark Ghiorso and Paolo Papale for helpful reviews which improved the  
1506 clarity and robustness of this manuscript, and the late Peter Fox for his editorial handling of the first  
1507 draft of this manuscript.

1508       **Data Availability** The Jupyter notebooks and associated Excel spreadsheets used to cre-  
 1509       ate the figures in this manuscript are currently hosted at <https://github.com/PennyWieser/>  
 1510       VESIcal\_II, and will be added to the main VESIcal github upon acceptance of this article. Videos  
 1511       showing how to use VESIcal are hosted on YouTube [https://www.youtube.com/channel/](https://www.youtube.com/channel/UCpvCCs5KMXz0xXWm0seF8Qw)  
 1512       UCpvCCs5KMXz0xXWm0seF8Qw.

1513       **References**

- 1514       Allan, J. F., BATIZA, R., PERFIT, M. R., FORNARI, D. J., & SACK, R. O. (1989). Petrology of  
 1515       lavas from the lamont seamount chain and adjacent east pacific rise, 10 n. *Journal of Petrology*,  
 1516       30(5), 1245–1298.
- 1517       Allison, C. M., Roggensack, K., & Clark, A. (2021). Highly explosive basaltic eruptions driven by co2  
 1518       exsolution. *Nature Communications*.
- 1519       Allison, C. M., Roggensack, K., & Clarke, A. B. (2019). H 2 o-co 2 solubility in alkali-rich mafic  
 1520       magmas: new experiments at mid-crustal pressures. *Contributions to Mineralogy and Petrology*,  
 1521       174(7), 58.
- 1522       Aster, E. M., Wallace, P. J., Moore, L. R., Watkins, J., Gazel, E., & Bodnar, R. J. (2016). Recon-  
 1523       structing co2 concentrations in basaltic melt inclusions using raman analysis of vapor bubbles.  
 1524       *Journal of Volcanology and Geothermal Research*, 323, 148–162.
- 1525       Atlas, Z. D., Dixon, J. E., Sen, G., Finny, M., & Martin-Del Pozzo, A. L. (2006). Melt inclusions from  
 1526       volcán popocatépetl and volcán de colima, mexico: melt evolution due to vapor-saturated crys-  
 1527       tallization during ascent. *Journal of Volcanology and Geothermal Research*, 153(3-4), 221–240.
- 1528       Behrens, H., Ohlhorst, S., Holtz, F., & Champenois, M. (2004). Co2 solubility in dacitic melts  
 1529       equilibrated with h2o-co2 fluids: Implications for modeling the solubility of co2 in silicic melts.  
 1530       *Geochimica et Cosmochimica Acta*, 68(22), 4687–4703.
- 1531       Blank, J., Stolper, E., & Carroll, M. (1993). Solubilities of carbon dioxide and water in rhyolitic melt  
 1532       at 850 c and 750 bars. *Earth and Planetary Science Letters*, 119(1-2), 27–36.
- 1533       Blundy, J., & Cashman, K. (2005). Rapid decompression-driven crystallization recorded by melt inclu-  
 1534       sions from mount st. helens volcano. *Geology*, 33(10), 793–796.
- 1535       Blundy, J., Cashman, K., & Humphreys, M. (2006). Magma heating by decompression-driven crystal-  
 1536       lization beneath andesite volcanoes. *Nature*, 443(7107), 76–80.
- 1537       Botcharnikov, R. E., Behrens, H., & Holtz, F. (2006). Solubility and speciation of c-o-h fluids in an-  
 1538       desitic melt at t= 1100–1300 c and p= 200 and 500 mpa. *Chemical Geology*, 229(1-3), 125–143.
- 1539       Botcharnikov, R. E., Holtz, F., & Behrens, H. (2007). The effect of co2 on the solubility of h2o-cl flu-  
 1540       ids in andesitic melt. *European Journal of Mineralogy*, 19(5), 671–680.

- 1541 Bowen, N. (1928). The evolution of the igneous rocks, princeton, univ. *Press, Princeton, New Jersey.*
- 1542 Brooker, R., Kohn, S., Holloway, J., & McMillan, P. (2001a). Structural controls on the solubility of  
1543 co<sub>2</sub> in silicate melts: part i: bulk solubility data. *Chemical Geology*, 174(1-3), 225–239.
- 1544 Brooker, R., Kohn, S., Holloway, J., & McMillan, P. (2001b). Structural controls on the solubility  
1545 of co<sub>2</sub> in silicate melts: part ii: Ir characteristics of carbonate groups in silicate glasses. *Chemical*  
1546 *Geology*, 174(1-3), 241–254.
- 1547 Bucholz, C. E., Gaetani, G. A., Behn, M. D., & Shimizu, N. (2013). Post-entrapment modification of  
1548 volatiles and oxygen fugacity in olivine-hosted melt inclusions. *Earth and Planetary Science Let-*  
1549 *ters*, 374, 145–155.
- 1550 Bureau, H., & Kepller, H. (1999). Complete miscibility between silicate melts and hydrous fluids in  
1551 the upper mantle: experimental evidence and geochemical implications. *Earth and Planetary Sci-*  
1552 *ence Letters*, 165(2), 187–196.
- 1553 Burgisser, A., Alletti, M., & Scaillet, B. (2015). Simulating the behavior of volatiles belonging to the  
1554 c–o–h–s system in silicate melts under magmatic conditions with the software d-compress. *Com-*  
1555 *puters & Geosciences*, 79, 1–14.
- 1556 Burnham, C. W. (1979). The importance of volatile constituents. *The evolution of the igneous rocks*,  
1557 439–482.
- 1558 Burnham, C. W., & Davis, N. (1971). The role of h<sub>2</sub>o in silicate melts; i, pvt relations in the sys-  
1559 tem naalsi 3 o 8-h 2 o to 10 kilobars and 1000 degrees c. *American Journal of Science*, 270(1),  
1560 54–79.
- 1561 Burnham, C. W., & Davis, N. (1974). The role of h<sub>2</sub>o in silicate melts; ii, thermodynamic and phase  
1562 relations in the system naalsi 3 o 8-h 2 o to 10 kilobars, 700 degrees to 1100 degrees c. *American*  
1563 *Journal of Science*, 274(8), 902–940.
- 1564 Cassidy, M., Edmonds, M., Watt, S. F., Palmer, M. R., & Gernon, T. M. (2015). Origin of basalts by  
1565 hybridization in andesite-dominated arcs. *Journal of Petrology*, 56(2), 325–346.
- 1566 Cocheo, P., & Holloway, J. (1993). The solubility of h<sub>2</sub>o in basanitic melts at low pressure. *EOS*  
1567 *Transactions of the American Geophysical Union* 74.
- 1568 Cottrell, E., Lanzirotti, A., Mysen, B., Birner, S., Kelley, K. A., Botcharnikov, R., ... Newville, M.  
1569 (2018). A mössbauer-based xanes calibration for hydrous basalt glasses reveals radiation-induced  
1570 oxidation of fe. *American Mineralogist: Journal of Earth and Planetary Materials*, 103(4),  
1571 489–501.
- 1572 Dingwell, D. B. (1986). Volatile solubilities in silicate melts.
- 1573 Dixon, J. E. (1997). Degassing of alkalic basalts. *American Mineralogist*, 82(3-4), 368–378.

- 1574 Dixon, J. E., Stolper, E. M., & Holloway, J. R. (1995). An experimental study of water and carbon  
1575 dioxide solubilities in mid-ocean ridge basaltic liquids. part i: calibration and solubility models.  
1576 *Journal of Petrology*, 36(6), 1607–1631.
- 1577 Duan, X. (2014). A general model for predicting the solubility behavior of h<sub>2</sub>o–co<sub>2</sub> fluids in silicate  
1578 melts over a wide range of pressure, temperature and compositions. *Geochimica et Cosmochimica  
1579 Acta*, 125, 582–609.
- 1580 Duan, Z., & Zhang, Z. (2006). Equation of state of the h<sub>2</sub>o, co<sub>2</sub>, and h<sub>2</sub>o–co<sub>2</sub> systems up to 10 gpa  
1581 and 2573.15 k: Molecular dynamics simulations with ab initio potential surface. *Geochimica et  
1582 cosmochimica acta*, 70(9), 2311–2324.
- 1583 Eggler, D. (1973). Role of co<sub>2</sub> in melting processes in the mantle. *Carnegie Inst. Wash. Yearb*, 72,  
1584 457–467.
- 1585 Eguchi, J., & Dasgupta, R. (2018). A co<sub>2</sub> solubility model for silicate melts from fluid saturation to  
1586 graphite or diamond saturation. *Chemical Geology*, 487, 23–38.
- 1587 Fine, G., & Stolper, E. (1986). Dissolved carbon dioxide in basaltic glasses: concentrations and specia-  
1588 tion. *Earth and Planetary Science Letters*, 76(3-4), 263–278.
- 1589 Flowers, G. C. (1979). Correction of holloway's (1977) adaptation of the modified redlich-kwong equa-  
1590 tion of state for calculation of the fugacities of molecular species in supercritical fluids of geologic  
1591 interest. *Contributions to Mineralogy and Petrology*, 69(3), 315–318.
- 1592 Fogel, R. A., & Rutherford, M. J. (1990). The solubility of carbon dioxide in rhyolitic melts; a quanti-  
1593 tative ftir study. *American Mineralogist*, 75(11-12), 1311–1326.
- 1594 Freise, M. (2004). *Differenzierung von basalten einer “large igneous province” am Beispiel des Kergue-  
1595 len Plateaus. Eine experimentelle Studie* (Unpublished doctoral dissertation). PhD thesis, Univer-  
1596 sity of Hannover.
- 1597 Gaborieau, M., Laubier, M., Bolfan-Casanova, N., Mccammon, C., Vantelon, D., Chumakov, A.,  
1598 ... Venugopal, S. (2020). Determination of fe<sup>3+</sup>/σfe of olivine-hosted melt inclusions using  
1599 mössbauer and xanes spectroscopy. *Chemical Geology*, 119646.
- 1600 Gaetani, G. A., O'Leary, J. A., Shimizu, N., Bucholz, C. E., & Newville, M. (2012). Rapid reequilibra-  
1601 tion of h<sub>2</sub>o and oxygen fugacity in olivine-hosted melt inclusions. *Geology*, 40(10), 915–918.
- 1602 Gavrilenko, M., Krawczynski, M., Ruprecht, P., Li, W., & Catalano, J. G. (2019). The quench control  
1603 of water estimates in convergent margin magmas. *American Mineralogist: Journal of Earth and  
1604 Planetary Materials*, 104(7), 936–948.
- 1605 Gerlach, T. M. (1986). Exsolution of h<sub>2</sub>o, co<sub>2</sub>, and s during eruptive episodes at kilauea volcano,  
1606 hawaii. *Journal of Geophysical Research: Solid Earth*, 91(B12), 12177–12185.

- 1607 Ghiorso, M. S., Carmichael, I. S., Rivers, M. L., & Sack, R. O. (1983). The gibbs free energy of mix-  
1608 ing of natural silicate liquids; an expanded regular solution approximation for the calculation of  
1609 magmatic intensive variables. *Contributions to Mineralogy and Petrology*, 84(2), 107–145.
- 1610 Ghiorso, M. S., & Gualda, G. A. (2015). An h<sub>2</sub>o–co<sub>2</sub> mixed fluid saturation model compatible with  
1611 rhyolite-melts. *Contributions to Mineralogy and Petrology*, 169(6), 1–30.
- 1612 Ghiorso, M. S., & Sack, R. O. (1995). Chemical mass transfer in magmatic processes iv. a revised  
1613 and internally consistent thermodynamic model for the interpolation and extrapolation of liquid-  
1614 solid equilibria in magmatic systems at elevated temperatures and pressures. *Contributions to  
1615 Mineralogy and Petrology*, 119(2-3), 197–212.
- 1616 Ghiorso, M. S., & Sverjensky, D. A. (2016). The melts-dew connection: Integration of thermodynamic  
1617 models for magmatic systems and aqueous fluids at elevated temperatures and pressures. In *Agu  
1618 fall meeting abstracts* (Vol. 2016, pp. V33H–04).
- 1619 Gleeson, M. L., Gibson, S. A., & Williams, H. M. (2020). Novel insights from fe-isotopes into the  
1620 lithological heterogeneity of ocean island basalts and plume-influenced morbs. *Earth and Planetary  
1621 Science Letters*, 535, 116114.
- 1622 Gleeson, M. L., Stock, M. J., Pyle, D. M., Mather, T. A., Hutchison, W., Yirgu, G., & Wade, J.  
1623 (2017). Constraining magma storage conditions at a restless volcano in the main ethiopian  
1624 rift using phase equilibria models. *Journal of Volcanology and Geothermal Research*, 337, 44–61.
- 1625 Goltz, A. E., Krawczynski, M. J., Gavrilenko, M., Gorbach, N. V., & Ruprecht, P. (2020). Evidence  
1626 for superhydrinous primitive arc magmas from mafic enclaves at shiveluch volcano, kamchatka.  
1627 *Contributions to Mineralogy and Petrology*, 175(12), 1–26.
- 1628 Goranson, R. W. (1931). Solubility of water in granite magmas. *Eos, Transactions American Geophys-  
1629 ical Union*, 12(1), 183–183.
- 1630 Gualda, G. A., & Ghiorso, M. S. (2015). Melts \_ e xcel: Am icrosoft e xcel-based melts interface for re-  
1631 search and teaching of magma properties and evolution. *Geochemistry, Geophysics, Geosystems*,  
1632 16(1), 315–324.
- 1633 Gualda, G. A., Ghiorso, M. S., Lemons, R. V., & Carley, T. L. (2012). Rhyolite-melts: a modified cal-  
1634 ibration of melts optimized for silica-rich, fluid-bearing magmatic systems. *Journal of Petrology*,  
1635 53(5), 875–890.
- 1636 Hamilton, D., Burnham, C. W., & Osborn, E. (1964). The solubility of water and effects of oxygen fu-  
1637 gacity and water content on crystallization in mafic magmas. *Journal of Petrology*, 5(1), 21–39.
- 1638 Hartley, M. E., Maclennan, J., Edmonds, M., & Thordarson, T. (2014). Reconstructing the deep co<sub>2</sub>  
1639 degassing behaviour of large basaltic fissure eruptions. *Earth and Planetary Science Letters*, 393,

- 1640 120–131.
- 1641 Hartley, M. E., Neave, D. A., Maclennan, J., Edmonds, M., & Thordarson, T. (2015). Diffusive over-  
1642 hydration of olivine-hosted melt inclusions. *Earth and Planetary Science Letters*, 425, 168–178.
- 1643 Hauri, E. (2002). Sims analysis of volatiles in silicate glasses, 2: isotopes and abundances in hawaiian  
1644 melt inclusions. *Chemical Geology*, 183(1-4), 115–141.
- 1645 Hauri, E., Kent, A. J., & Arndt, N. (2002). Melt inclusions at the millennium: toward a deeper under-  
1646 standing of magmatic processes. *ChGeo*, 183(1-4), 1–3.
- 1647 Helz, R., & Thornber, C. R. (1987). Geothermometry of kilauea iki lava lake, hawaii. *Bulletin of Vol-*  
1648 *canology*, 49(5), 651–668.
- 1649 Hervig, R., Dunbar, N., Westrich, H. R., & Kyle, P. R. (1989). Pre-eruptive water content of rhyolitic  
1650 magmas as determined by ion microprobe analyses of melt inclusions in phenocrysts. *Journal of*  
1651 *Volcanology and Geothermal Research*, 36(4), 293–302.
- 1652 Hervig, R., & Williams, P. (1988). Sims microanalysis of minerals and glasses for h and d. *SIMS VI*  
1653 *Proceedings*, 961–964.
- 1654 Hess, K., & Dingwell, D. (1996). Viscosities of hydrous leucogranitic melts: A non-arrhenian model.  
1655 *American Mineralogist*, 81(9-10), 1297–1300.
- 1656 Holloway, J. R. (1977). Fugacity and activity of molecular species in supercritical fluids. In *Thermody-*  
1657 *namics in geology* (pp. 161–181). Springer.
- 1658 Holloway, J. R., & Blank, J. G. (1994). Application of experimental results to coh species in natural  
1659 melts. *Reviews in mineralogy*, 30, 187–187.
- 1660 Huang, F., & Sverjensky, D. A. (2019). Extended deep earth water model for predicting major element  
1661 mantle metasomatism. *Geochimica et Cosmochimica Acta*, 254, 192–230.
- 1662 Huber, C., Townsend, M., Degruyter, W., & Bachmann, O. (2019). Optimal depth of subvolcanic  
1663 magma chamber growth controlled by volatiles and crust rheology. *Nature Geoscience*, 12(9),  
1664 762–768.
- 1665 Huppert, H. E., & Woods, A. W. (2002). The role of volatiles in magma chamber dynamics. *Nature*,  
1666 420(6915), 493–495.
- 1667 Husen, A., Almeev, R. R., & Holtz, F. (2016). The effect of h<sub>2</sub>o and pressure on multiple saturation  
1668 and liquid lines of descent in basalt from the shatsky rise. *Journal of Petrology*, 57(2), 309–344.
- 1669 Iacono-Marziano, G., Morizet, Y., Le Trong, E., & Gaillard, F. (2012). New experimental data and  
1670 semi-empirical parameterization of h<sub>2</sub>o–co<sub>2</sub> solubility in mafic melts. *Geochimica et Cosmochim-*  
1671 *ica Acta*, 97, 1–23.
- 1672 Iacovino, K., Matthews, S., Wieser, P. E., Moore, G., & Begue, F. (2021). Vesical part i: An open

- 1673 source thermodynamic model engine for mixed volatile solubility in silicate melts. *EarthArxiv -*  
1674 <https://doi.org/10.31223/X5D606>.
- 1675 Iacovino, K., Moore, G., Roggensack, K., Oppenheimer, C., & Kyle, P. (2013). H<sub>2</sub>O–CO<sub>2</sub> solubility in  
1676 mafic alkaline magma: applications to volatile sources and degassing behavior at Erebus volcano,  
1677 Antarctica. *Contributions to Mineralogy and Petrology*, 166(3), 845–860.
- 1678 Iddon, F., & Edmonds, M. (2020). Volatile-rich magmas distributed through the upper crust in the  
1679 main Ethiopian rift. *Geochemistry, Geophysics, Geosystems*, 21(6), e2019GC008904.
- 1680 Jakobsson, S. (1997). Solubility of water and carbon dioxide in an icelandite at 1400 °C and 10 kilobars.  
1681 *Contributions to Mineralogy and Petrology*, 127(1–2), 129–135.
- 1682 Kerrick, D., & Jacobs, G. (1981). A modified Redlich-Kwong equation for H<sub>2</sub>O, CO<sub>2</sub>, and H<sub>2</sub>O-CO<sub>2</sub>  
1683 mixtures at elevated pressures and temperatures. *American Journal of Science*, 281(6), 735–  
1684 767.
- 1685 King, P., & Holloway, J. (2002). CO<sub>2</sub> solubility and speciation in intermediate (andesitic) melts: the  
1686 role of H<sub>2</sub>O and composition. *Geochimica et Cosmochimica Acta*, 66(9), 1627–1640.
- 1687 Koleszar, A., Kent, A. J., Wallace, P. J., & Scott, W. E. (2012). Controls on long-term low explosivity at  
1688 andesitic arc volcanoes: Insights from Mount Hood, Oregon. *Journal of Volcanology and  
1689 Geothermal Research*, 219, 1–14.
- 1690 Koleszar, A., Saal, A., Hauri, E., Nagle, A., Liang, Y., & Kurz, M. (2009). The volatile contents of  
1691 the Galapagos plume; evidence for H<sub>2</sub>O and F open system behavior in melt inclusions. *Earth and  
1692 Planetary Science Letters*, 287(3–4), 442–452.
- 1693 Lesne, P., Scaillet, B., Pichavant, M., & Beny, J.-M. (2011). The carbon dioxide solubility in alkali  
1694 basalts: an experimental study. *Contributions to Mineralogy and Petrology*, 162(1), 153–168.
- 1695 Lesne, P., Scaillet, B., Pichavant, M., Iacono-Marziano, G., & Beny, J.-M. (2011). The H<sub>2</sub>O solu-  
1696 bility of alkali basaltic melts: an experimental study. *Contributions to Mineralogy and Petrology*,  
1697 162(1), 133–151.
- 1698 Le Voyer, M., Hauri, E., Cottrell, E., Kelley, K. A., Salters, V. J., Langmuir, C. H., ... Füri, E.  
1699 (2019). Carbon fluxes and primary magma CO<sub>2</sub> contents along the global mid-ocean ridge system.  
1700 *Geochemistry, Geophysics, Geosystems*, 20(3), 1387–1424.
- 1701 Li, Y., Dasgupta, R., & Tsuno, K. (2017). Carbon contents in reduced basalts at graphite saturation:  
1702 Implications for the degassing of Mars, Mercury, and the Moon. *Journal of Geophysical Research:  
1703 Planets*, 122(6), 1300–1320.
- 1704 Liu, Y., Zhang, Y., & Behrens, H. (2005). Solubility of H<sub>2</sub>O in rhyolitic melts at low pressures and a  
1705 new empirical model for mixed H<sub>2</sub>O–CO<sub>2</sub> solubility in rhyolitic melts. *Journal of Volcanology and*

- 1706                   *Geothermal Research*, 143(1-3), 219–235.
- 1707   Lloyd, A. S., Plank, T., Ruprecht, P., Hauri, E., & Rose, W. (2013). Volatile loss from melt inclusions  
1708                   in pyroclasts of differing sizes. *Contributions to Mineralogy and Petrology*, 165(1), 129–153.
- 1709   Lowenstern, J. B. (1995). Applications of silicate-melt inclusions to the study of magmatic volatiles.  
1710                   *Magmas, fluids and ore deposits*, 23, 71–99.
- 1711   Lowenstern, J. B. (2001). Carbon dioxide in magmas and implications for hydrothermal systems. *Min-  
1712                   eralium Deposita*, 36(6), 490–502.
- 1713   Lowenstern, J. B. (2003). Melt inclusions come of age: volatiles, volcanoes, and sorby's legacy. In *De-  
1714                   velopments in volcanology* (Vol. 5, pp. 1–21). Elsevier.
- 1715   Lucic, G., Berg, A.-S., & Stix, J. (2016). Water-rich and volatile-undersaturated magmas at hekla vol-  
1716                   cano, iceland. *Geochemistry, Geophysics, Geosystems*, 17(8), 3111–3130.
- 1717   Maclellan, J. (2017). Bubble formation and decrepitation control the co<sub>2</sub> content of olivine-hosted  
1718                   melt inclusions. *Geochemistry, Geophysics, Geosystems*, 18(2), 597–616.
- 1719   Makhluf, A. R., Newton, R., & Manning, C. (2020). Experimental investigation of phase relations  
1720                   in the system naalsi 3 o 8-h 2 o at high temperatures and pressures: liquidus relations, liquid–  
1721                   vapor mixing, and critical phenomena at deep crust–upper mantle conditions. *Contributions to  
1722                   Mineralogy and Petrology*, 175(8), 1–20.
- 1723   Mangan, M. T., Sisson, T. W., Hankins, W. B., Shimizu, N., & Vennemann, T. (2021). Constraints  
1724                   on deep, co<sub>2</sub>-rich degassing at arc volcanoes from solubility experiments on hydrous basaltic an-  
1725                   desite of pavlof volcano, alaska peninsula, at 300 to 1200 mpa. *American Mineralogist: Journal  
1726                   of Earth and Planetary Materials*, 106(5), 762–773.
- 1727   Métrich, N., & Wallace, P. J. (2008). Volatile abundances in basaltic magmas and their degassing  
1728                   paths tracked by melt inclusions. *Reviews in mineralogy and geochemistry*, 69(1), 363–402.
- 1729   Mironov, N., Tobelko, D., Smirnov, S., Portnyagin, M. V., & Krasheninnikov, S. (2020). Estimation  
1730                   of co<sub>2</sub> content in the gas phase of melt inclusions using raman spectroscopy: Case study of in-  
1731                   clusions in olivine from the karymsky volcano (kamchatka). *Russian Geology and Geophysics*,  
1732                   61(5-6), 600–610.
- 1733   Mitchell, A. L., Gaetani, G. A., O'leary, J. A., & Hauri, E. H. (2017). H 2 o solubility in basalt at up-  
1734                   per mantle conditions. *Contributions to Mineralogy and Petrology*, 172(10), 1–16.
- 1735   Moore, G. (2008). Interpreting h<sub>2</sub>o and co<sub>2</sub> contents in melt inclusions: constraints from solubility ex-  
1736                   periments and modeling. *Reviews in Mineralogy and Geochemistry*, 69(1), 333–362.
- 1737   Moore, G., & Carmichael, I. (1998). The hydrous phase equilibria (to 3 kbar) of an andesite and  
1738                   basaltic andesite from western mexico: constraints on water content and conditions of phenocryst

- 1739 growth. *Contributions to Mineralogy and Petrology*, 130(3-4), 304–319.
- 1740 Moore, G., Roggensack, K., & Klonowski, S. (2008). A low-pressure–high-temperature technique for  
1741 the piston-cylinder. *American Mineralogist*, 93(1), 48–52.
- 1742 Moore, G., Vennemann, T., & Carmichael, I. (1998). An empirical model for the solubility of h<sub>2</sub>o in  
1743 magmas to 3 kilobars. *American Mineralogist*, 83(1), 36–42.
- 1744 Moore, L. R., Gazel, E., Tuohy, R., Lloyd, A. S., Esposito, R., Steele-MacInnis, M., ... Bodnar, R. J.  
1745 (2015). Bubbles matter: An assessment of the contribution of vapor bubbles to melt inclusion  
1746 volatile budgets. *American Mineralogist*, 100(4), 806–823.
- 1747 Mutch, E. J., MacLennan, J., Shorttle, O., Edmonds, M., & Rudge, J. F. (2019). Rapid transcrustal  
1748 magma movement under iceland. *Nature Geoscience*, 12(7), 569–574.
- 1749 Mysen, B. O. (1976). The role of volatiles in silicate melts; solubility of carbon dioxide and water in  
1750 feldspar, pyroxene, and feldspathoid melts to 30 kb and 1625 degrees c. *American Journal of Sci-  
1751 ence*, 276(8), 969–996.
- 1752 Mysen, B. O., Eggler, D. H., Seitz, M., & Holloway, J. R. (1976). Carbon dioxide in silicate melts and  
1753 crystals; part i, solubility measurements. *American Journal of Science*, 276(4), 455–479.
- 1754 Mysen, B. O., Fogel, M. L., Morrill, P. L., & Cody, G. D. (2009). Solution behavior of reduced coh  
1755 volatiles in silicate melts at high pressure and temperature. *Geochimica et Cosmochimica Acta*,  
1756 73(6), 1696–1710.
- 1757 Newman, S., & Lowenstern, J. B. (2002). Volatilecalc: a silicate melt–h<sub>2</sub>o–co<sub>2</sub> solution model written  
1758 in visual basic for excel. *Computers & Geosciences*, 28(5), 597–604.
- 1759 Ochs, F. A., & Lange, R. A. (1999). The density of hydrous magmatic liquids. *Science*, 283(5406),  
1760 1314–1317.
- 1761 Paonita, A., Gigli, G., Gozzi, D., Nuccio, P., & Trigila, R. (2000). Investigation of the he solubility  
1762 in h<sub>2</sub>o–co<sub>2</sub> bearing silicate liquids at moderate pressure: a new experimental method. *Earth and  
1763 Planetary Science Letters*, 181(4), 595–604.
- 1764 Papale, P. (1997). Modeling of the solubility of a one-component h<sub>2</sub> o or co<sub>2</sub> fluid in silicate liquids.  
1765 *Contributions to Mineralogy and Petrology*, 126(3), 237–251.
- 1766 Papale, P. (1999). Modeling of the solubility of a two-component h<sub>2</sub>o+ co<sub>2</sub> fluid in silicate liquids.  
1767 *American Mineralogist*, 84(4), 477–492.
- 1768 Papale, P., Moretti, R., & Barbato, D. (2006). The compositional dependence of the saturation surface  
1769 of h<sub>2</sub>o+ co<sub>2</sub> fluids in silicate melts. *Chemical Geology*, 229(1-3), 78–95.
- 1770 Papale, P., Neri, A., & Macedonio, G. (1999). The role of water content and magma composition  
1771 on explosive eruption dynamics. *Physics and Chemistry of the Earth, Part A: Solid Earth and*

- 1772                   *Geodesy*, 24(11-12), 969–975.
- 1773     Plank, T., Kelley, K. A., Zimmer, M. M., Hauri, E., & Wallace, P. J. (2013). Why do mafic arc mag-
- 1774       mas contain 4 wt% water on average? *Earth and Planetary Science Letters*, 364, 168–179.
- 1775     Portnyagin, M., Almeev, R., Matveev, S., & Holtz, F. (2008). Experimental evidence for rapid water
- 1776       exchange between melt inclusions in olivine and host magma. *Earth and Planetary Science Let-*
- 1777       *ters*, 272(3-4), 541–552.
- 1778     Putirka, K. D. (2008). Thermometers and barometers for volcanic systems. *Reviews in Mineralogy and*
- 1779       *Geochemistry*, 69(1), 61–120.
- 1780     Rasmussen, D. J., Plank, T. A., Wallace, P. J., Newcombe, M. E., & Lowenstern, J. B. (2020). Vapor-
- 1781       bubble growth in olivine-hosted melt inclusions. *American Mineralogist: Journal of Earth and*
- 1782       *Planetary Materials*, 105(12), 1898–1919.
- 1783     Reubi, O., & Blundy, J. (2009). A dearth of intermediate melts at subduction zone volcanoes and the
- 1784       petrogenesis of arc andesites. *Nature*, 461(7268), 1269–1273.
- 1785     Roggensack, K. (2001). Unraveling the 1974 eruption of fuego volcano (guatemala) with small crystals
- 1786       and their young melt inclusions. *Geology*, 29(10), 911–914.
- 1787     Rohatgi, A. (2017). *Webplotdigitizer*. Austin, Texas, USA.
- 1788     Saal, A. E., Hauri, E., Langmuir, C. H., & Perfit, M. R. (2002). Vapour undersaturation in primitive
- 1789       mid-ocean-ridge basalt and the volatile content of earth's upper mantle. *Nature*, 419(6906), 451–
- 1790       455.
- 1791     Shishkina, T., Botcharnikov, R. E., Holtz, F., Almeev, R., & Portnyagin, M. V. (2010). Solubility
- 1792       of h<sub>2</sub>o-and co<sub>2</sub>-bearing fluids in tholeiitic basalts at pressures up to 500 mpa. *Chemical geology*,
- 1793       277(1-2), 115–125.
- 1794     Shishkina, T., Botcharnikov, R. E., Holtz, F., Almeev, R. R., Jazwa, A. M., & Jakubiak, A. A. (2014).
- 1795       Compositional and pressure effects on the solubility of h<sub>2</sub>o and co<sub>2</sub> in mafic melts. *Chemical Ge-*
- 1796       *ology*, 388, 112–129.
- 1797     Sides, I., Edmonds, M., MacLennan, J., Swanson, D., & Houghton, B. (2014a). Eruption style at
- 1798       kīlauea volcano in hawai ‘i linked to primary melt composition. *Nature Geoscience*, 7(6), 464.
- 1799     Sides, I., Edmonds, M., MacLennan, J., Swanson, D., & Houghton, B. (2014b). Magma mixing and
- 1800       high fountaining during the 1959 kīlauea iki eruption, hawai ‘i. *Earth and Planetary Science Let-*
- 1801       *ters*, 400, 102–112.
- 1802     Silver, L. A. (1988). *Water in silicate glasses* (Unpublished doctoral dissertation). California Institute
- 1803       of Technology.
- 1804     Silver, L. A., Ihinger, P. D., & Stolper, E. (1990). The influence of bulk composition on the speciation

- 1805 of water in silicate glasses. *Contributions to Mineralogy and Petrology*, 104(2), 142–162.
- 1806 Silver, L. A., & Stolper, E. (1989). Water in albitic glasses. *Journal of petrology*, 30(3), 667–709.
- 1807 Steele-Macinnis, M., Esposito, R., & Bodnar, R. J. (2011). Thermodynamic model for the effect  
1808 of post-entrapment crystallization on the h<sub>2</sub>O–CO<sub>2</sub> systematics of vapor-saturated, silicate melt  
1809 inclusions. *Journal of Petrology*, 52(12), 2461–2482.
- 1810 Stevenson, J. (2015). *Tasplot*. <https://bitbucket.org/jsteven5/tasplot/src/master/>. bitbucket.
- 1811 Stolper, E. (1982). Water in silicate glasses: an infrared spectroscopic study. *Contributions to Mineral-  
1812 ogy and Petrology*, 81(1), 1–17.
- 1813 Stolper, E., Fine, G., Johnson, T., & Newman, S. (1987). Solubility of carbon dioxide in albitic melt.  
1814 *American Mineralogist*, 72(11–12), 1071–1085.
- 1815 Sverjensky, D. A., Harrison, B., & Azzolini, D. (2014). Water in the deep earth: the dielectric constant  
1816 and the solubilities of quartz and corundum to 60 kb and 1200 °C. *Geochimica et Cosmochimica  
1817 Acta*, 129, 125–145.
- 1818 Tamura, Y., & Tatsumi, Y. (2002). Remelting of an andesitic crust as a possible origin for rhyolitic  
1819 magma in oceanic arcs: an example from the Izu–Bonin arc. *Journal of Petrology*, 43(6), 1029–  
1820 1047.
- 1821 Tucker, J. M., Hauri, E., Pietruszka, A. J., Garcia, M. O., Marske, J. P., & Trusdell, F. A. (2019). A  
1822 high carbon content of the Hawaiian mantle from olivine-hosted melt inclusions. *Geochimica et  
1823 Cosmochimica Acta*, 254, 156–172.
- 1824 Tuttle, O. F., & Bowen, N. L. (1958). *Origin of granite in the light of experimental studies in the sys-  
1825 tem naalsi308-kalsi308-si02-h20* (Vol. 74). Geological Society of America.
- 1826 Venugopal, S., Schiavi, F., Moune, S., Bolfan-Casanova, N., Druitt, T., & Williams-Jones, G. (2020).  
1827 Melt inclusion vapour bubbles: the hidden reservoir for major and volatile elements. *Scientific  
1828 Reports*, 10(1), 1–14.
- 1829 Wallace, P. J., Anderson, A. T., & Davis, A. M. (1995). Quantification of pre-eruptive exsolved gas  
1830 contents in silicic magmas. *Nature*, 377(6550), 612–616.
- 1831 Waters, L. E., & Lange, R. A. (2013). Crystal-poor, multiply saturated rhyolites (obsidians) from the  
1832 cascade and Mexican arcs: evidence of degassing-induced crystallization of phenocrysts. *Contri-  
1833 butions to Mineralogy and Petrology*, 166(3), 731–754.
- 1834 Waters, L. E., & Lange, R. A. (2015). An updated calibration of the plagioclase-liquid hygrometer-  
1835 thermometer applicable to basalts through rhyolites. *American Mineralogist*, 100(10), 2172–  
1836 2184.
- 1837 Wieser, P. E., Lamadrid, H., MacLennan, J., Edmonds, M., Matthews, S., Iacovino, K., ... others

(2021). Reconstructing magma storage depths for the 2018 kilauean eruption from melt inclusion  
co<sub>2</sub> contents: the importance of vapor bubbles. *Geochemistry, Geophysics, Geosystems*, 22(2),  
e2020GC009364.

# **Supporting Information for "VESIcal Part II: A critical approach to volatile solubility modelling using an open-source Python3 engine"**

P. E. Wieser<sup>1,2</sup>, K. Iacovino<sup>3</sup>, S. Matthews<sup>4</sup>, G. Moore <sup>3</sup>, C. M. Allison <sup>5,6</sup>

<sup>1</sup>Department of Earth Sciences, University of Cambridge, UK.

<sup>2</sup>Now at College of Earth, Ocean and Atmospheric sciences, Oregon State University

<sup>3</sup>Jacobs, NASA Johnson Space Center, Houston, TX 77058, USA.

<sup>4</sup>Johns Hopkins University, Department of Earth and Planetary Sciences, Baltimore, MD 21218, USA.

<sup>5</sup>Cornell University, Department of Earth and Atmospheric Sciences, Ithaca, NY 14853

<sup>6</sup>City College of New York, City University of New York, New York, NY 10031

## **Contents of this file**

1. Figures S1 to S12

2. Text S1

3. Table S1

## **Introduction**

This supplement presents a number of additional figures, and further explanation with respect to how the coefficients in the IM–2012 models account for some of the behaviours shown by this model.

---

Corresponding author: P. E. Wieser, Now at the College of Earth, Ocean and Atmospheric Sciences, Oregon State University. (penny.wieser@gmail.com)

### 0.1. IM–2012 - Difference in isobar curvature

As noted in the main text, the anhydrous version of this model shows a more prominent peak in isobar space compared to the hydrous model. This reflects differences in the coefficient  $d_{H_2O}$  attached to the term for the molar fraction of  $H_2O$  in the melt. In the anhydrous version,  $d_{H_2O}$  is positive ( $2.3 \pm 0.5$ ), so the addition of small amounts of  $H_2O$  to the melt causes  $X_{H_2O}$ , and therefore  $CO_2$  solubility to increase. In the hydrous expression, this coefficient is negative ( $-16.4 \pm 1.2$ ). Alone, this would cause the solubility of  $CO_2$  to decrease with the addition of small amounts of water to the melt. However, NBO/O calculated on a hydrous basis increases with the addition of  $H_2O$  (because  $X_{H_2O}$  appears twice in the numerator, but only once in the denominator of the NBO/O term), and the NBO/O term is attached to a positive coefficient ( $17.3 \pm 0.9$ ). This increase in NBO/O overwhelms the product of the negative coefficient multiplied by  $X_{H_2O}$ .

### References

- Dixon, J. E. (1997). Degassing of alkalic basalts. *American Mineralogist*, 82(3-4), 368–378.
- Mangan, M. T., Sisson, T. W., Hankins, W. B., Shimizu, N., & Vennemann, T. (2021). Constraints on deep, co<sub>2</sub>-rich degassing at arc volcanoes from solubility experiments on hydrous basaltic andesite of pavlof volcano, alaska peninsula, at 300 to 1200 mpa. *American Mineralogist: Journal of Earth and Planetary Materials*, 106(5), 762–773.

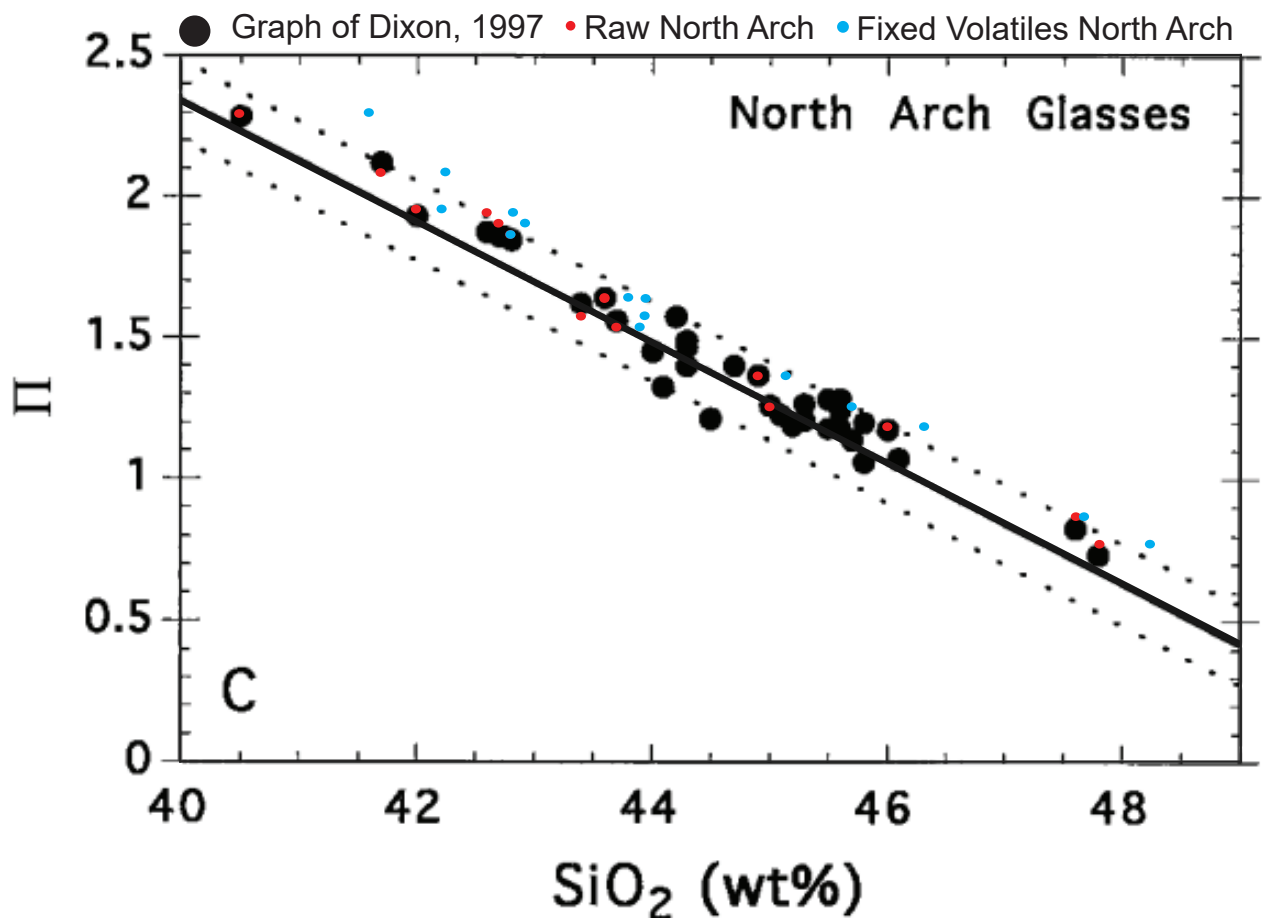


**Figure S1.** II vs. SiO<sub>2</sub> graph shown in Fig. 2C of Dixon (1997). Red dots show the raw data presented in Table 1 of Dixon (1997), with analytical totals ranging between 97.38 to 99.995 wt%, while cyan dots show this data following the VESIcal Fixed Volatiles normalization routine. It is apparent that raw data is a significantly better fit; all normalization routines shift SiO<sub>2</sub> contents to higher values.

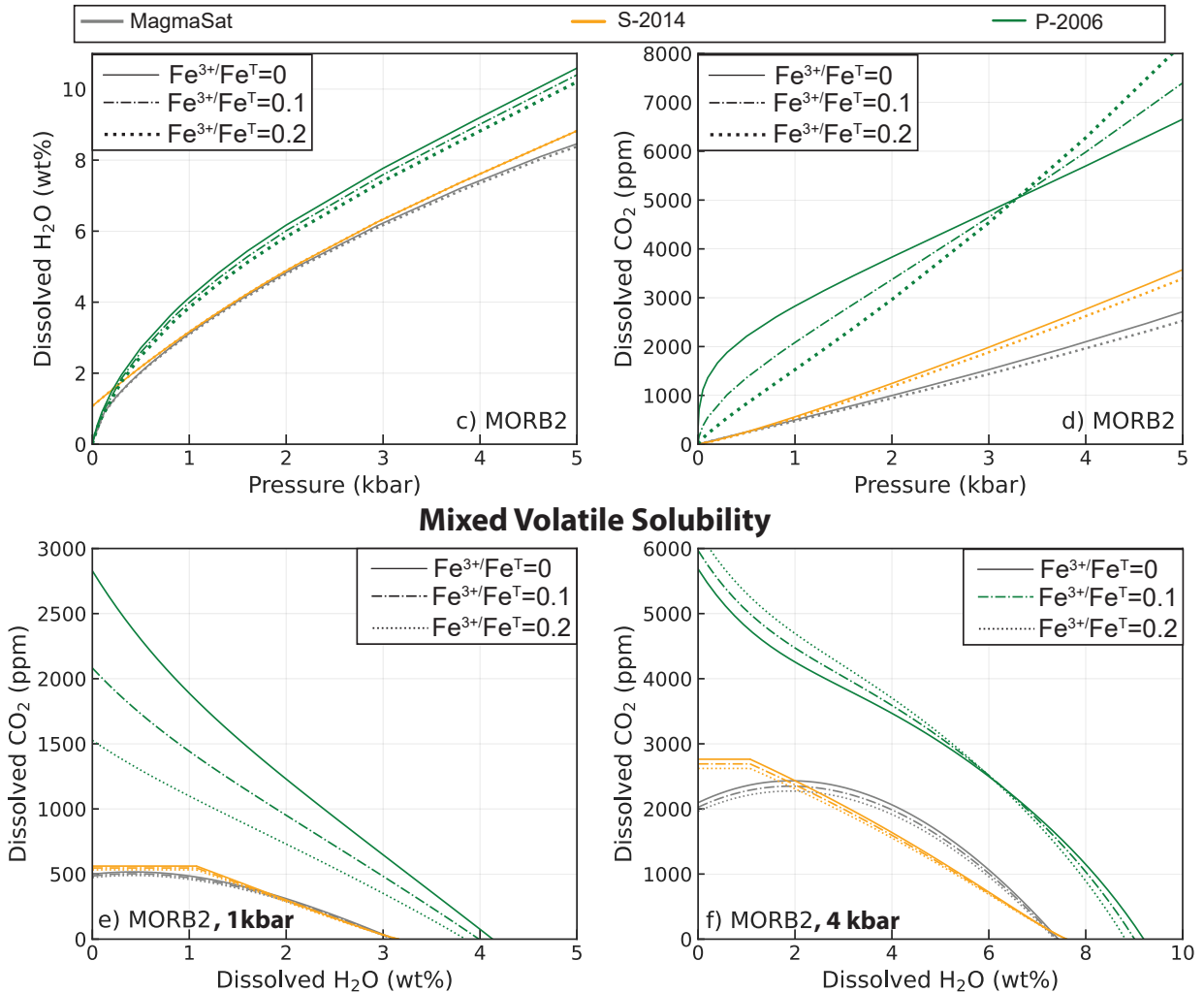


**Figure S2.** Parts c-d as in Fig. 4 of the main text, with the addition of isobars calculated for the MORB2 composition for different proportions of Fe<sup>3+</sup> at 1 and 4 kbar.

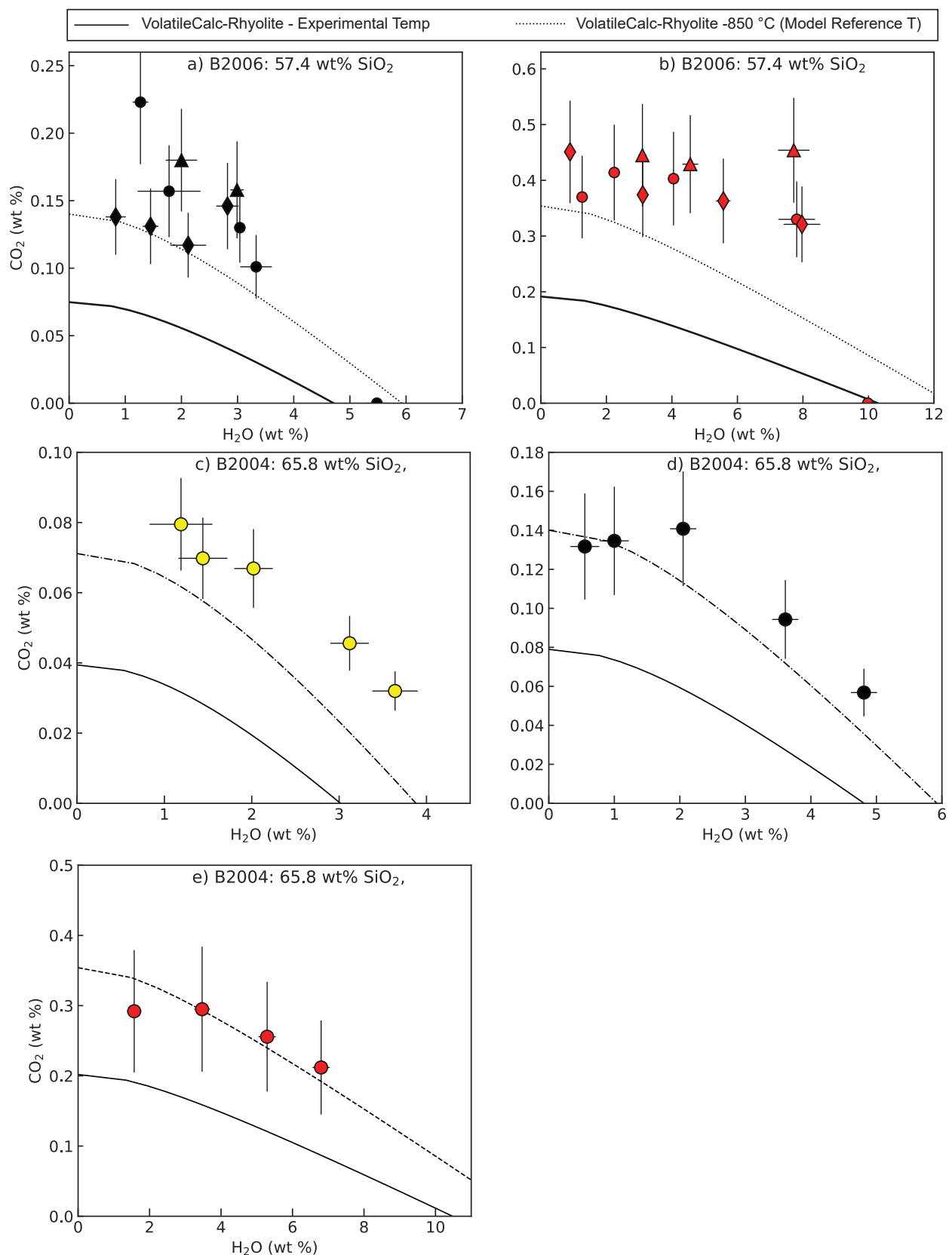


**Figure S3.** Recreation of the figure in the main text for andesitic isobars, but also showing VolatileCalc-Rhyolite isobars calculated at the reference temperature of this model (850°C). These are a significantly better fit to experimental products.

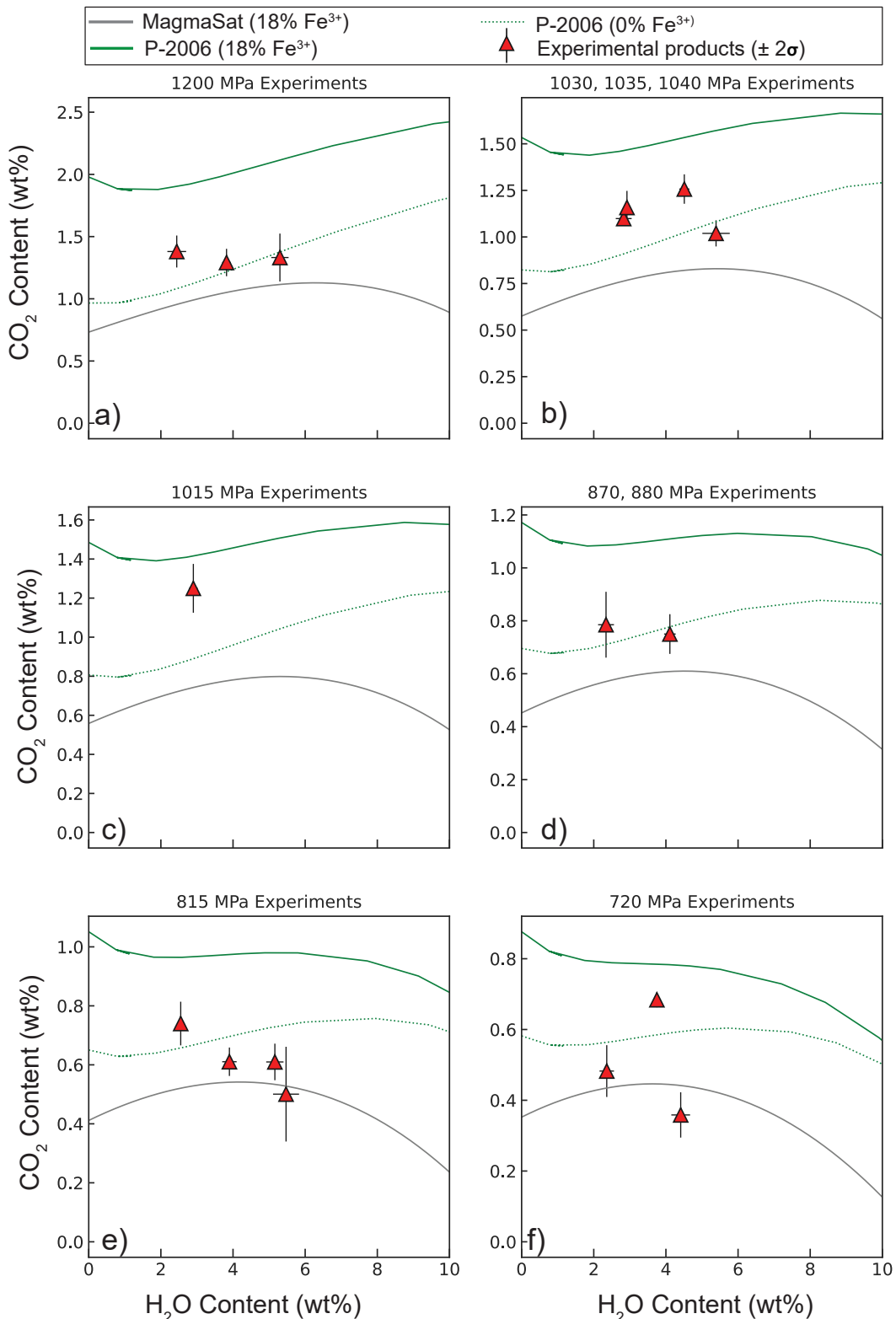


**Figure S4.** Isobars calculated for the major element composition of run number 1890 from Mangan et al. (2021) at 1125°C. As in the main text, calculations for P-2006 are performed for no  $\text{Fe}^{3+}$ , and a best estimate of the proportion of  $\text{Fe}^{3+}$  in the experiments (from MELTS for Excel based on reported oxygen fugacity). Isobars in b) calculated for 1035 MPa, isobars in d) calculated for 875 MPa.

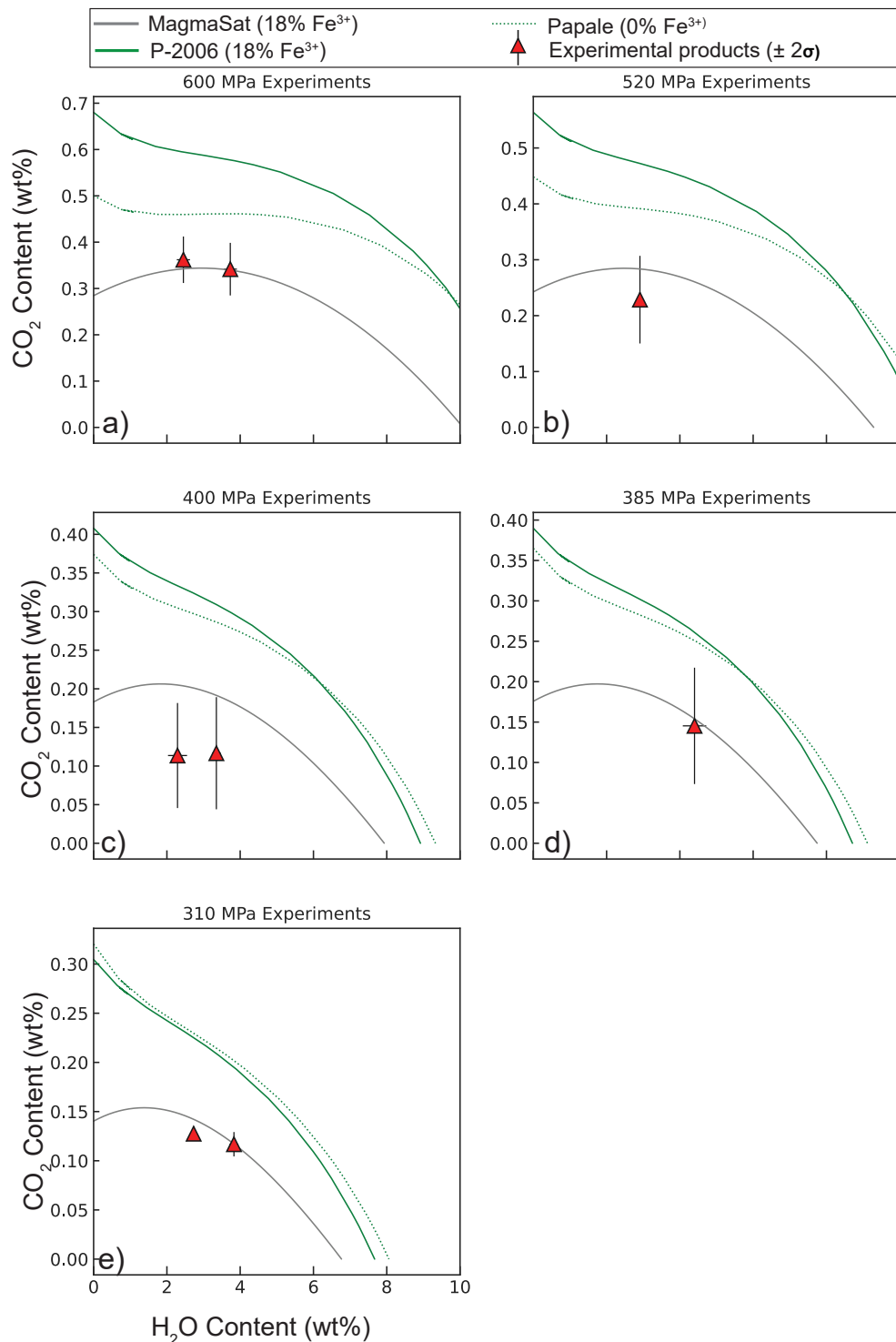


**Figure S5.** Isobars calculated for the major element composition of run number 1890 from Mangan et al. (2021) at 1125°C. As in the main text, calculations for P-2006 are performed for no Fe<sup>3+</sup>, and a best estimate of the proportion of Fe<sup>3+</sup> in the experiments (from MELTS for Excel based on reported oxygen fugacity). Considering the error bars on measured volatile contents and on models (not shown, but likely 10-20%), MagmaSat recreates all experimental solubilities within error.

## Popocatépetl - Atlas et al. (2006)

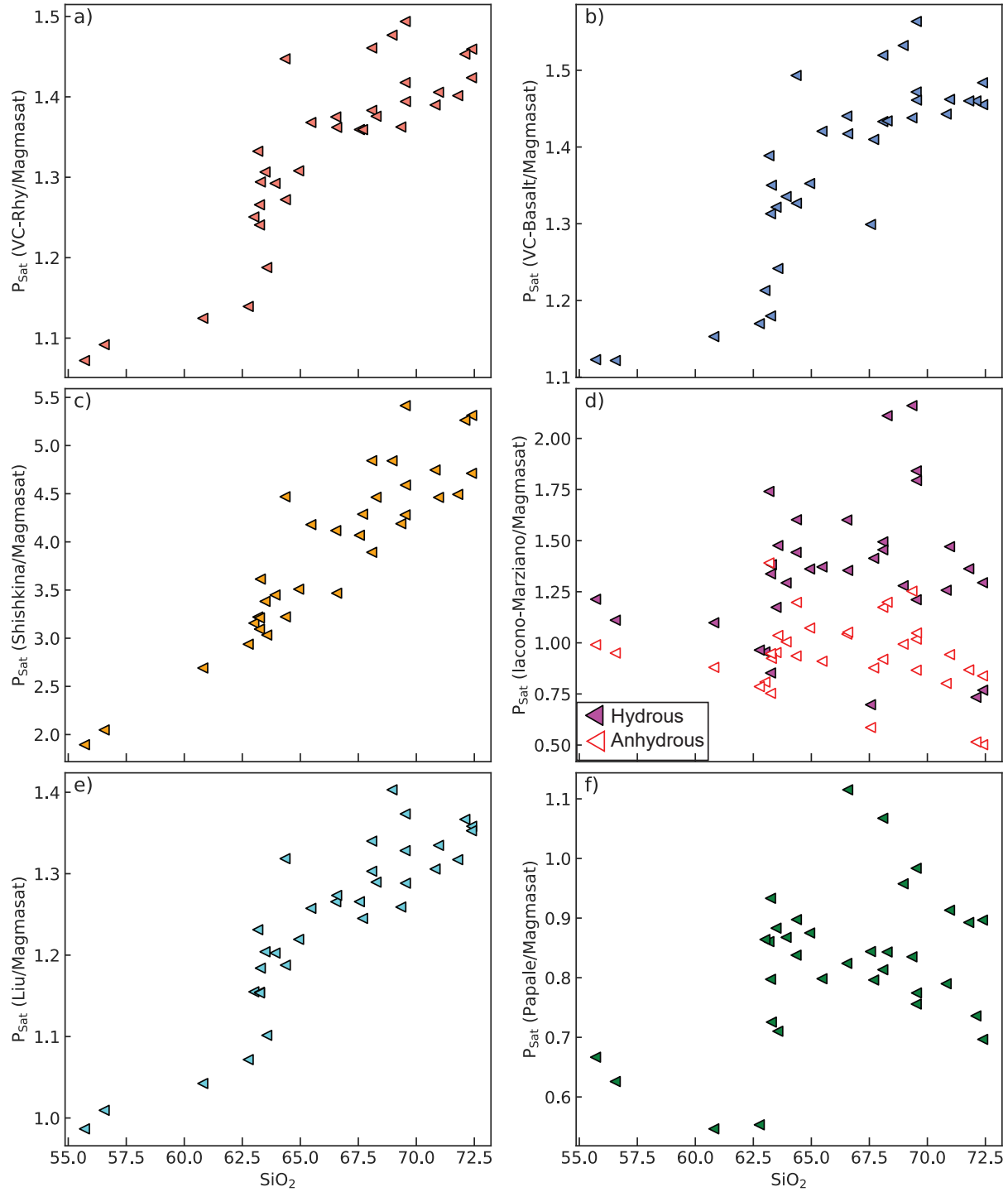


**Figure S6.** Discrepancies between various models and MagmaSat for the suite of Popocatépetl melt inclusions from Atlas et al. (2006). The strong correlation between  $\text{SiO}_2$  and  $\Pi^*$  for these inclusions (Fig. 15a, main text) may account for the increased discrepancy between Shishkina and MagmaSat with increasing  $\text{SiO}_2$ .

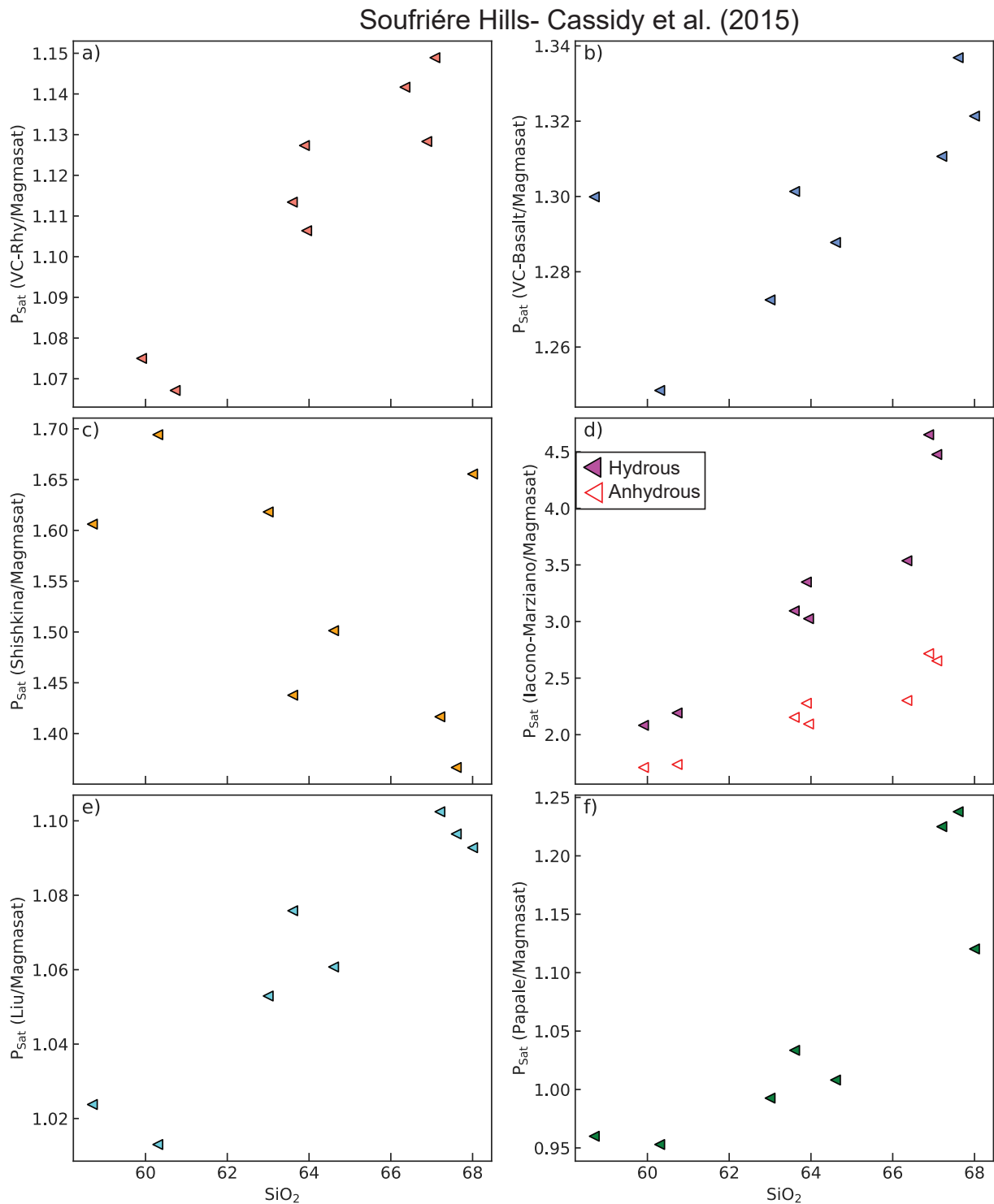


**Figure S7.** Discrepancies between various models and MagmaSat for the suite of Soufrière Hills melt inclusions from Cassidy et al. (2015). NBO/O decreases with increasing  $\text{SiO}_2$  in the Soufrière Hills inclusions (Fig. 15c, main text), which may explain why the discrepancy between Iacono-Marziano and MagmaSat increases with increasing  $\text{SiO}_2$ .

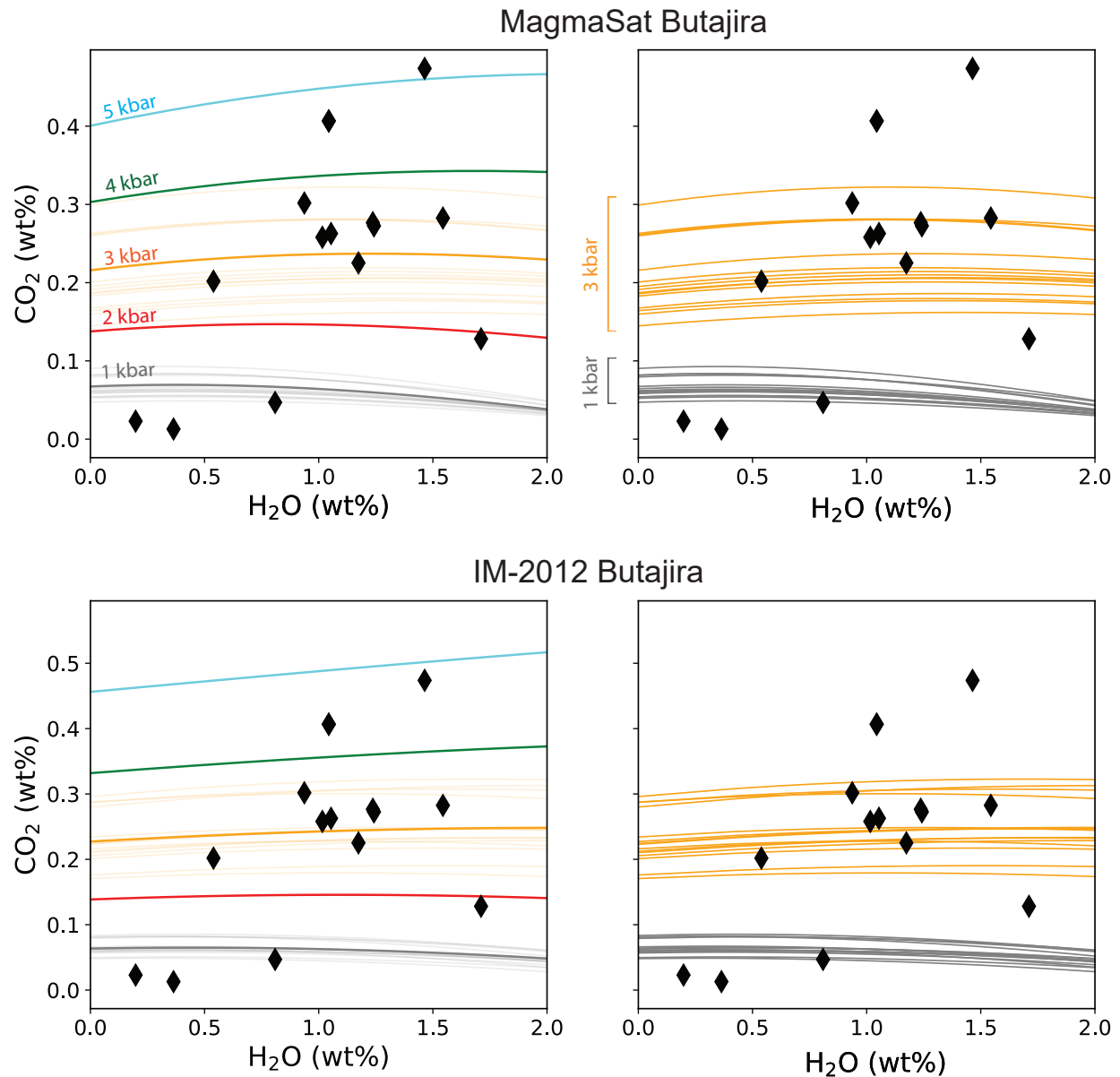


**Figure S8.** Comparison of isobars calculated for Butajira using MagmaSat (as shown in the main text) vs. IM-2012-H. This demonstrates that both models predict a spread of isobar positions.

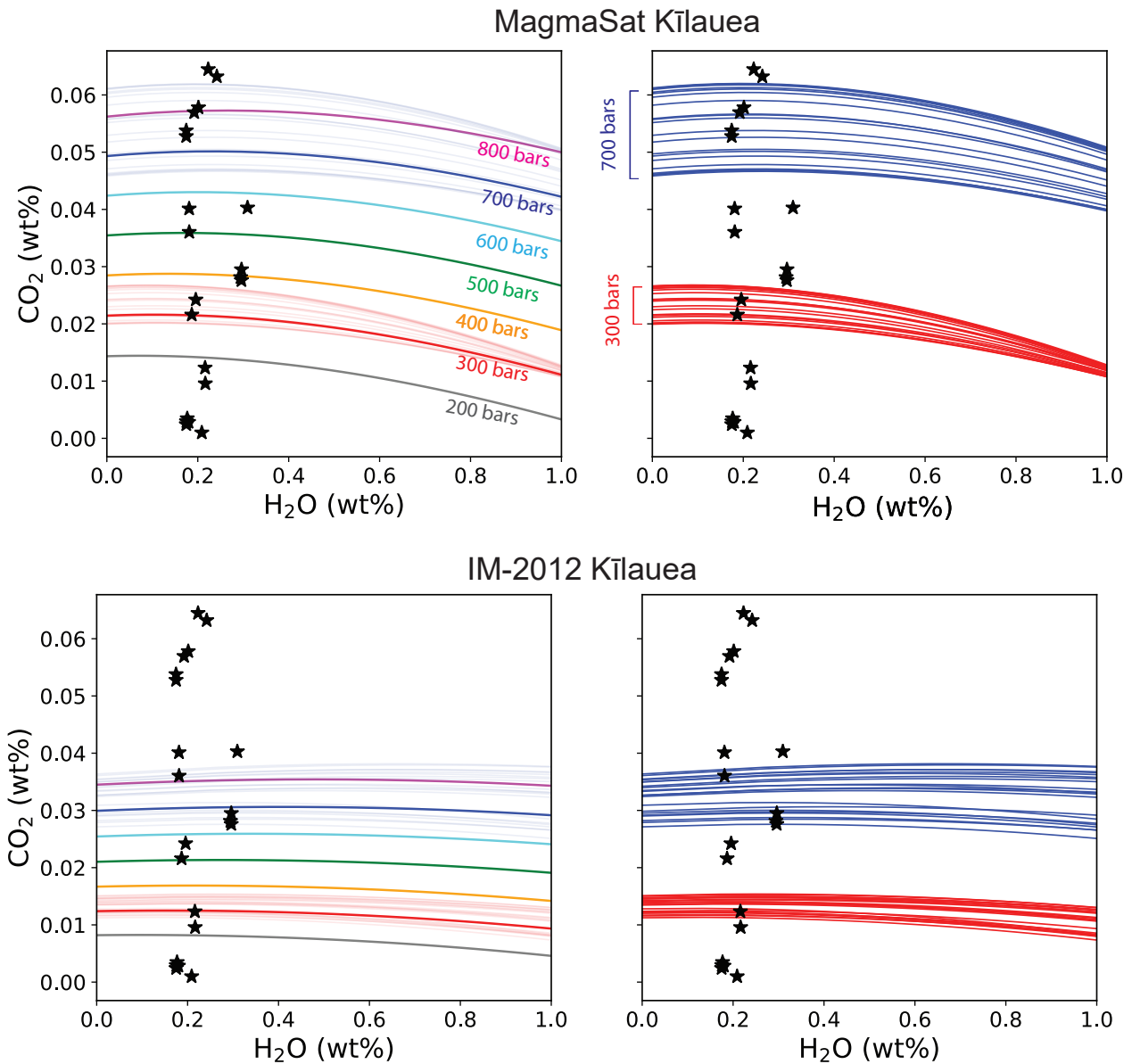


**Figure S9.** Comparison of isobars calculated for Kīlauea using MagmaSat (as shown in the main text) vs. IM-2012-H. This demonstrates that both models predict a spread of isobar positions.